Zinc Dyshomeostasis in *Salmonella*-Infected Immune Competent Primary Macrophage Impacts Infection Outcome

by

Michael T. Minson

B.S. University of Utah, 2012

A thesis submitted to the

Faculty of the Graduate School of the University of Colorado

in partial fulfillment of the requirements for the degree of

Doctor of Philosophy

College of Arts & Sciences

Department of Biochemistry

2019

This thesis entitled:
"Zinc Dyshomeostasis in *Salmonella*-Infected Immune Competent Primary Macrophage Impacts Infection Outcome"
written by Michael T. Minson
has been approved for the Department of Biochemistry

_____
Amy E. Palmer

_____
Jeffery Cameron

Date _____

The final copy of this thesis has been examined by the signatories, and we find that both the content and the form meet acceptable presentation standards of scholarly work in the above mentioned discipline.

Minson, Michael T. (Ph.D., Biochemistry)

"Zinc Dyshomeostasis in *Salmonella*-Infected Immune Competent Primary Macrophage Impacts Infection Outcome"

Thesis directed by Prof. Amy E. Palmer

Zinc is an essential micronutrient for mammalian cells and their bacterial pathogens. Intracellular pathogens such as *Salmonella sp.* colonize macrophages to form systemic infections and must acquire enough Zn^{2+} to survive and replicate within their host cell. The interface of this infection is defined largely by a tug of war for Zn^{2+}. Macrophages that have been activated by phagocytosis of a pathogen shift their intracellular zinc pool through upregulation of a zinc importer that sequesters zinc from the extracellular milieu. Using tools developed in the Palmer lab, we quantified the cytosolic labile zinc concentration in primary immune competent macrophages infected with the intracellular pathogen *Salmonella* Typhimurium and show that it increases over the course of the infection. We measured an increase in the expression of the zinc importer Zip14, and show that the ability of these macrophages to control bacterial replication and clear the intracellular pathogen is altered due to changes in the availability of zinc in the media. Zinc reduction in the media correlates with the expression of the spliced Xbp1 isoform, a marker for ER stress, indicating that the zinc adequacy is important for resistance to ER stress during infection.

Dedication

To my family, without your love, support and inspiration, none of this would have been possible

Acknowledgements

I am so grateful to my parents who raised me to be to be a problem solver and a hard worker. Thank you for teaching me to dream and believe that anything is possible. Thank you for all of your sacrifices to get me here.

I would never have been able to do this without the support of my wonderful girlfriend Saaraa. Thank you so much for helping me keep it together and keeping me afloat when I needed it most. Thank you for pushing me to be better and believing in me, and Thank you for all of the many wonderful adventures we've shared. May there be many more!

Thanks to all of my friends that I have made here in Colorado throughout my time here. We've had a great deal of adventure and shenanigans and that has made all of the difference to me. I'd especially like to thank Michal Matyjasik and Nicholas Parsonet, who have been fellow grad students and fellow climbers, you've kept me motivated, and you've kept me safe. To anyone who has shared a rope with me, thank you for your trust and your adventurous spirit, on belay!

I must thank everyone in the Palmer Lab for making the lab a great place to work every day. Thank you Esther Braselmann for being a great help on many of my projects and for all of your encouragement. Thank you Maria Lo, birthday buddies! And thanks to former members of the lab, Kyle Carter, Sarah McQuate, and Ali Young, for being my rotation mentor and getting me hooked on studying *Salmonella*.

I owe a big debt of thanks to Dr. Shelley Minteer at the University of Utah who welcomed me into her lab and gave me a fantastic project to work on the last year of my undergraduate career and thank you Matt Meredith for being such a great mentor. I would not have gone to graduate school without your encouragement and support.

Thanks to my thesis committee, Corrie Detweiler, Jeff Cameron, Joel Kralj and Xuedong Liu. For their expertise and guidance and support during my graduate school career. Thank you, Corrie for all of the support since the very beginning, for a great rotation, and for the continued collaboration and support and advice that we've had with your lab over the years.

Finally, I would like to say thank you to Amy Palmer, who has been a wonderful mentor and has really pushed me to grow and mature in my thinking and inspired me to be keep growing as a thinker and scientist, but also as a person. Thank you for everything!

Contents

Chapter

Figures

Tables

Chapter 1

Introduction

1.1 Publication Status and Author Contributions

Young, A.M., Minson, M, McQuate, S.E., Palmer, A.E., "Optimized Fluorescence Complementation Platform for Visualizing *Salmonella* Effector Proteins Reveals Distinctly Different Intracellular Niches in Different Cell Types" *ACS Infectious Diseases*, 2017

A.M.Y. designed the experiments, A.M.Y., M.M., S.E.M. carried out the research, A.M.Y., A.E.P., S.E.M., and M.M. wrote the manuscript.

Batan, D., Braselmann, E., Minson, M., Nguyen Thanh, D.M., Cossart, P., Palmer, A.E., "A Multicolor Split-Fluorescent Protein Approach to Visualize Listeria Protein Secretion in Infection" *Biophysical Journal,* 2018

D.B., E.B., A.E.P. designed research; D.B., E.B., M.M., D.M.T.N. performed research; D.B., E.B., M.M., D.M.T.N. analyzed data; P.C. contributed reagents and experimental advice; D.B., E.B., A.E.P. wrote the manuscript.

Portions of this chapter were reproduced from these publications.

1.2 Salmonella Pathogenesis and Effector Proteins

Salmonella enterica is a facultative intracellular Gram-negative bacterium that is a major cause of enteric disease in humans and animals[1]. *S. enterica* is subdivided into over 2500 serovars. Certain serovars of *S. enterica* cause disease in humans, ranging from gastroenteritis that resolves without antibiotics to a systemic infection such as typhoid fever or paratyphoid fever which requires immediate treatment with antibiotics. *S. enterica* serovars display host specificity, therefore the severity of the disease depends on the serovar and the host. *S. enterica* serovar Typhi are responsible for the persistent systemic infection that causes typhoid fever[2] in humans while serovar Typhimurium causes food poisoning in humans but causes a systemic infection in mice similar to typhoid fever[3]. *Salmonella* may persist in the host for long periods of time after symptoms have resided allowing them to spread to other animals and humans primarily through oral-fecal contact[4]. Agricultural populations infected with *Salmonella* begin to shed high levels of bacteria upon treatment with antibiotics[5] making it difficult to manage disease spread.

Salmonella is among a class of intracellular pathogens that survive and replicate by acquiring access to and manipulating the interior of a variety of eukaryotic host cells[6]. These bacteria are equipped with a set of needle-like secretion systems known as Type III secretion systems 1 and 2 (T3SS)[7] that span both the inner and outer bacterial membrane and then penetrate the membrane of a host cell. The T3SS delivers a payload of virulence proteins into the host, termed "effectors," that bind and modulate functional targets within the host cell[8]. *Salmonella* infection proceeds through the route of ingestion and exposure to the gut epithelium. Once ingested, bile exposure signals the genes expressed on *Salmonella* pathogenicity island 1 (SPI-1) to produce the secretion machinery[9]. When *Salmonella* comes into contact with the apical membrane of the gut epithelium, effectors are translocated into the cell, inducing remodeling of the actin cytoskeleton and causing phagocytosis of the bacteria. Inside the host cell, the bacterium resides within a vacuole, called the *Salmonella* containing vacuole (SCV). There, it actively remodels the SCV membrane to block lysosome fusion. The SCV is trafficked along the endosomal pathway until the vacuole begins to acidify which signals the bacteria to express the *Salmonella* pathogenicity Island 2 (SPI-2) genes which encode for the

second T3SS and another array of effectors that get translocated into the host. SPI-2 effectors are responsible for maintaining the vacuolar niche by actively modulating the SCV, acquiring nutrition by coopting host vesicle traffic, and modulating the immune response of the host cell[10–12].

Salmonella infection can progress to a systemic infection as bacteria cross the intestinal mucosa into the blood. In the blood, *Salmonella* can migrate throughout the body infecting different cell types and replicating intracellularly. Professional phagocytes such as macrophages, dendritic cells and neutrophils try to mitigate the infection by phagocytosis of the bacteria. However, *Salmonella* is capable of evading the microbiocidal activity of the macrophages and hide out within, waiting to be disseminated to other parts of the body including the spleen and the liver[13–15]. The sophistication of the diverse array of effectors secreted by *Salmonella* provides a versatile strategy to enter and replicate within a variety of host cell types and develop a resilient replicative niche.

The coordinated action of the bacterial effector proteins and their spatial and temporal localization are critical for bacterial survival, replication and dissemination within the host. There are over 65 putative *Salmonella* effector proteins[16]. The functional roles of many of the effectors and their functional targets within the host are still unknown. The order of secretion of effectors and their localization in the host are spatially distinct with each effector acting at a specific time for a specific duration throughout infection[16–19]. There has been a considerable amount of work aimed at elucidating and characterizing the functional role of many of the effectors. A well characterized *Salmonella* effector protein, SifA, plays a critical role in maintaining the integrity of the SCV by tethering the vacuole to the pleckstrin homology domain of the host protein SifA-kinesin interacting protein (SKIP)[20,21]. It also possesses a WxxxE motif in its C-terminal domain that mimics the active form of host Rho-GTPases. The two functional domains within this effector protein serve to acquire more membrane by tethering the vacuole to kinesin which promotes the formation of tubular membranous structures called *Salmonella* induced filaments (SIFs). This increases real estate of the SCV and fosters the growth of the bacteria inside the host cell. Interestingly, it was through the study of this *Salmonella* effector protein that the host protein SKIP was discovered. This is good example of how the study of host-pathogen interactions can lead to discoveries within eukaryotic cell biology[22].

Recently, it was discovered that SifA also has a DxxD caspase-3 cleavable domain that when cleaved provides a unique localization for both domains, and is required for proper function and localization of the effector[23]. Investigations into the role of SifA demonstrate that effector function can be modular, complex, and dynamic with a diverse set of spatial and temporal localizations. Considering that new effector functions and localizations are continuously being discovered, even for well characterized proteins, and that there is heterogeneity of infection phenotypes, it is clear that investigative techniques that can capture single cell infection dynamics and map the spatial and temporal changes in effector localizations, such as live-cell fluorescence microscopy, will be an essential tool for unraveling the complexity of effector roles.

1.3 Listeria Pathogenesis and Effector Proteins

Listeria monocytogenes is another intracellular pathogen that, like *Salmonella*, uses bacterial secretion systems to secrete virulence proteins into host cells to replicate and spread within an organism. This Gram-positive bacterium can cross the placental, intestinal and blood-brain barrier, making *Listeria* infections particularly dangerous for immunocompromised patients and pregnant women, for whom it can lead to miscarriage[24]. *Listeria* can enter different types of mammalian cells, including epithelial cells and macrophages, escape the internalization vacuole, replicate within the cytosol while escaping the immune response, and spread from cell to cell[24,25].

To enable and support the intracellular lifecycle, *Listeria* produces and secretes a series of proteins called virulence proteins during the infection process[26,27]. Over 700 proteins were predicted to have a signal peptide for secretion via Sec[28], the major secretion pathway in *Listeria*[29]. Six other secretion pathways exist in *Listeria*[27,30], and protein clients of these pathways continue to be cataloged by proteomic analyses[31,32]. There has been a considerable amount of work elucidating and characterizing the functional role of many of the effectors. For example, ActA is a well characterized effector protein that is secreted to *Listeria*'s surface and promotes actin nucleation that enables Listeria's spread from cell to cell[33–36]. Recently, it was found that ActA also plays an important role in biofilm formation[37,38]. Similarly, new roles of perhaps the most heavily studied *Listeria* virulence protein, Listeriolysin O (LLO), [39–41] continue to be discovered [42], including roles in organelle and histone manipulation [43,44].

Together, a picture of complex dynamics with ever increasing diversity of localization patterns and functionalities for secreted virulence proteins emerges, necessitating approaches to track these proteins on a single cell level during infection for mechanistic insights.

1.4 Tools for Imaging Effector Proteins

Live cell imaging is ideal for capturing the dynamics of infection but the complexity of bacterial secretion systems make fluorescent tagging of effector proteins technically challenging[7]. Cell fixation can alter infection phenotypes, such as the integrity of SIFs, and snap shots often fail to capture dynamic processes such as the coalescence or dispersion of the SCV[45]. Bacterial secretion systems require the secreted protein and their fusion partners to become partially unfolded[8]. In the case of the T3SS, proteins are translocated through a flagellar like needle complex that has a maximum diameter of about 28 angstroms. Fluorescent proteins are composed of highly stable ß-barrels that are difficult to unfold and are bigger than the size of the secretion machinery, making fluorescent proteins secretion incompetent.

One method that has been used for tagging effectors fuses a 3x repeat of the 12 amino acid tetracysteine (TC) motif which binds a fluorescein based bi-arsenical dye, FlAsH[18,46]. The FlAsH/TC system is great for measuring fast translocation events by fluorescence depletion when the tagged effectors are concentrated within the bacteria and released upon contact with the mammalian cell. But, it lacks the brightness needed to track the effector after it is secreted into the host cell and diffuses away from the site of translocation[18].

There are two systems currently in use capable of monitoring the localization of tagged effectors in live cells, the photostable improved Light Oxygen Voltage sensing domain (phiLOV) system[47] and the split-GFP system[17]. The phiLOV fluorescence reporter is an engineered variant derived from the blue light receptor phototropin that binds cellular flavin mononucleotide to produce fluorescence. This system boasts two advantages over GFP, its fluorescent signal is oxygen independent, making it ideal for anaerobic conditions, and it is small and flexible enough to be secretion competent in bacterial secretion systems. It has been used to measure translocation of effectors and track their localization after secretion. One major drawback to the phiLOV system is limited brightness. The quantum yield

for phiLov = 0.2-0.4 compared to QY = 0.6 for split-GFP[48]. This makes it difficult to track effectors that have lower concentrations within the host cell.

The Split-GFP was developed in the Waldo lab in 2005[49]. The system works by splitting the GFP protein into two separate fragments that spontaneously self-associate once in proximity with one another to reform the full-length protein. This can be used to tag effector proteins while circumventing the problem of bacterial secretion by genetically tagging the effector protein of interest with the small fragment of the GFP ß-barrel (GFP11, 16 amino acids) and expressing the remaining fragment, strands 1-10 (GFP1-10), in the host cell. Both fragments are non-fluorescent on their own but upon translocation of the GFP11 tagged effector into the host cell the two halves of the protein bind each other and the GFP chromophore begins to mature. One technical challenge faced in the application of the split-GFP system is that the fluorescence signal intensity is limited by the rate of chromophore maturation. The time it takes for split-GFP to mature is ~2 hours after complementation[49]. Additionally, cells that are difficult to transfect or ones that don't produce much protein from a transfection, such as primary cells, will have lower fluorescence signal due to having a lower concentration of GFP1-10.

Split-GFP was used to visualize the *Salmonella* SPI-2 effectors, SteA, PipB2, and SteC for the first time in 2010[17]. In this thesis work (Chapter 2), we sought to broaden the application of the split-GFP system by employing a generalized effector labeling platform that allowed us to tune the bacterial expression of the effector proteins and multimerize the tag in order to enhance fluorescence signal intensity for visualizing new effector proteins[50]. Additionally, we improved our ability to detect GFP fluorescence complementation by creating an orthogonal nuclear localized transfection marker that is co-expressed with GFP1-10 in the host cell. As part of this thesis, we show *Salmonella*[50] (Chapter 2) and *Listeria*[51] (Chapter 3) effector protein localization in live primary bone marrow derived macrophages for the first time and find that the localization of some effector proteins between macrophages and epithelial cells are distinct. Two new optimized split fluorescent proteins have recently been reported[52,53] and we have adapted their use for fluorescent tagging of both *Salmonella* and *Listeria* effector proteins[54]. Visualization of *Salmonella* effector proteins in live cell infection using

split GFP is discussed in Chapter 2. Tagging and visualization of *Listeria* proteins during live cell infection with split GFP, split mNeonGreen and split super folder Cherry is discussed in Chapter 3.

1.5 Nutritional Immunity

The mammalian host immune system has developed an arsenal of antimicrobial strategies to deal with insults from microbial pathogens such as *Salmonella* or *Listeria* in order to clear bacteria and limit bacterial replication[55]. One of the first lines of host defense is withholding of nutrients that are required for growth of the bacteria including zinc, iron, manganese and copper to prevent pathogen outgrowth, referred to as nutritional immunity[56–58]. Professional phagocytes, macrophages, neutrophils, and dendritic cells, phagocytose invading pathogens and subject them to reactive oxygen and nitrogen species[59,60], antimicrobial proteins and peptides[55], and nutrient starvation[61,62] or in some cases poisoning[63,64]. Many bacterial pathogens have evolved virulence mechanisms that allow them to evade killing, colonize and thrive within macrophages, forming a stable infection that becomes systemic[3,15,65–67].

Upon infection, mammalian hosts produce a number of antimicrobial proteins and peptides[68]. The function of many of these proteins is important in normal physiological processes within the host outside of the context of infection but their antimicrobial activity centers around their ability to sequester nutrient metals. An example of one such protein is the serum protein transferrin which binds free iron with an association constant of approximately 10^{36}, ensuring that availability of iron to invading pathogens is much less than what is needed to replicate and cause disease[56,69]. Another antimicrobial protein is calprotectin[68]. During an insult from invading pathogens, neutrophils will secrete an extracellular trap, NETs, that capture bacteria and inhibit bacterial growth. NETs are made up of DNA, chromatin, and granule proteins including calprotectin, a heterodimer of S100A8 and S100A9 proteins which tightly bind iron, manganese and zinc[70]. Calprotectin plays a vital role in limiting the availability of zinc, iron and manganese in the inflamed gut[68,71]. *Salmonella* thrives within the inflamed gut by overcoming zinc restriction with a high affinity zinc transporter, ZnuABC, which is required for virulence and maintenance of a systemic infection[68]. Restriction of essential

nutrients is a common host defense strategy to limit the growth of bacteria within the body and prevent disease[57,58,72].

Neutrophils are the most abundant form of white blood cell in circulation, but due to constitutive apoptosis they survive less than 24 hours in the blood[73]. The limited lifespan of neutrophils limits their capacity to become stable carriers of intracellular pathogens, and systemic infections are typically found within macrophages, long-lived innate immune cells[65,74]. Macrophages employ a wide range of antimicrobial strategies upon phagocytosis of a microbial pathogen including acidifying the phagolysosome, generation of reactive oxygen species (ROS) and reactive nitrogen species (RNS)[59,60], and removing essential metal ions from the phagolysosome[61,75] and in the case of some pathogens delivering toxic concentrations of metals into the phagolysosome to poison the intracellular pathogen[63,64]. The importance of metal withholding within macrophages is demonstrated by natural resistance associated macrophage protein 1 (Nramp1) which is a membrane bound divalent metal transporter expressed in lysosomal compartments. Nramp1 transports mainly iron and manganese out of the lumen of the phagolysosome and starves intracellular pathogens of those essential nutrients[76]. Mice who lack a functional Nramp1 are more susceptible to systemic infection from *Salmonella* Typhimurium, are not capable of preventing bacterial replication in the liver and spleen, and typically succumb to infection within a week[75]. Resistant mice, with a functional Nramp1, can control *Salmonella* replication and progressively clear infection from systemic tissue and usually survive infection[65]. Macrophages also remove zinc from the pathogen containing vacuole during infection from *Histoplasma capsulatum*[61] and *Salmonella*[62] but conversely deliver toxic concentrations of zinc and copper ions to the pathogen containing vacuole to poison intracellular *Mycobacterium tuberculosis*[64,72] and *E. coli*[63]. How macrophages decide which pathogen to starve and which to poison is still an open question. Zinc is essential for many organ systems, and is especially important in immune defense. The remodeling of zinc homeostasis and the impacts of these changes on host defense and physiology in response to infection are critical for understanding the host-pathogen interface.

1.6 Zinc Homeostasis

Zinc (Zn^{2+}) is the second most abundant trace element in the human body second to iron. It is a required nutrient for microorganisms, plants, animals and humans. Zn^{2+} is a d-block transition metal and has one naturally occurring oxidation state, Zn^{2+}. In its ionized form, Zn^{2+} has a full $3d^{10}$ valence shell and is redox inert in a biological context[77]. Mammalian cells actively accumulate Zn^{2+} from their extracellular environment. Total cellular Zn^{2+} is in the hundreds of micromolar range while serum or plasma Zn^{2+} is 1-10μM[78]. Within cells, Zn^{2+} is bound to proteins and small molecules with a range of binding affinities keeping the accessible, or labile, Zn^{2+} concentration to the range of hundreds picomolar in the cytoplasm[79–82]. Bioinformatic analysis estimates that about 3000 proteins, or 10% of the human proteome, have binding sites for Zn^{2+} [83]. Zn^{2+} has been found to have structural, catalytic, regulatory, and signaling[84] functions within cells. Given its ubiquity, Zn^{2+} is essential in virtually every process within cells.

Transport and trafficking of Zn^{2+} in humans occurs via active transport by 24 transmembrane proteins[85–87]. There are 14 SLC39A family or Zrt- Irt- like proteins (ZIPs)[87] which transport Zn^{2+} toward the cytosol and 10 SlC30A family or Znt proteins, Zn^{2+} exporters, which direct Zn^{2+} away from the cytosol[85,86]. These transporters are expressed differentially in different cell types and localize to a range of organelles. Buffering of labile Zn^{2+} within cells occurs through Zn^{2+} binding proteins and small sulfur containing molecules in conjunction with the expression level and localization of ZIPs and ZnTs. The most prominent effector of zinc buffering in the cell cytosol are metallothioneins (MTs), cysteine-rich proteins which can bind up to 7 Zn^{2+} ions. MTs bind and release Zn^{2+} to regulate the free Zn^{2+} level to protect against overload and death. MTs also play an important role in binding toxic metals such as cadmium and mercury, and scavenging a wide range of reactive oxygen species.

1.7 Zinc in Health and Nutrition

Dietary acquisition of Zn^{2+} occurs primarily through Zip4 expressed on the basolateral membrane of the intestinal lumen where it is absorbed into the cytosol directly from the chyme[88]. Additionally, Zn^{2+} is trafficked in the endosomal pathway of enterocytes where it is mobilized into the cytosol using

the Zip14 transporter. In mice fed $^{65}Zn^{2+}$ it was shown that $^{65}Zn^{2+}$ was enriched in endosomes isolated from the small intestines of Zip14 knockout mice compared to WT[89]. This occurred because a lack of Zip14 blocked mobilization of Zn^{2+} from early endosomes into the cytosol. This demonstrates that an important mechanism for the uptake of extracellular zinc into cells occurs by micropinocytosis and absorption from endosomes. Zn^{2+} is transported in the blood bound to the proteins albumin and α2-globulins then delivered to cells in the periphery. Zn^{2+} is found primarily in high protein containing foods[90]. Zn^{2+} content within plants is determined by the amount of Zn^{2+} present in the soil in which they are grown[87]. The bioavailability of nutritional Zn^{2+} is reduced in the presence of phytonutrients such as phytates, that chelate Zn^{2+} and other divalent cations and reduce their absorption[91]. A vegetarian or vegan diet reduces Zn^{2+} intake and may also reduce Zn^{2+} absorption[92]. Supplementation is effective for raising serum levels and improving Zn^{2+} adequacy in at risk populations[93–95].

Toxicity of Zn^{2+} is primarily seen in cases of over supplementation. In humans, supplementation of Zn^{2+} at levels above 100-300mg/day for several weeks impairs copper metabolism and reduces absorption of manganese and iron[96]. Poisoning from consumption of Zn^{2+} containing metals such as galvanized metal hardware or coins can occur because stomach acid is strong enough to ionize Zn metal which results in a massive release of ionic Zn^{2+} into the body.

Mild to moderate Zn^{2+}deficiency is an obstacle to optimal health and is a worldwide problem. It is estimated that 2 billion people are mildly or moderately Zn^{2+} deficient[97,98]. Zn^{2+} deficiency is more prevalent in geographic regions where the soil Zn^{2+} content is poor and access to high quality protein is lacking. Good clinical markers for Zn^{2+} status are still lacking, making assessment of Zn^{2+} status difficult[99]. Serum Zn^{2+} levels do not always correlate well with total Zn^{2+} content of surrounding tissues given that cells typically have a higher total zinc content than is found in the serum[78]. Serum Zn^{2+} represents 0.1% of total body Zn^{2+} and has high interindividual variation[99]. Relative serum concentration change from baseline, however, does correlate well with absorption[93]. Severe Zn^{2+} deficiency results in growth retardation, impaired sexual maturation, severe anemia, and cognitive deficits. Moderate Zn^{2+} deficiency reduces sperm production in mice[100]. Mild to moderate Zn^{2+} deficiency impairs innate and adaptive immune function through a variety of mechanisms. Mild Zn^{2+}

deficiency can increase circulation of proinflammatory cytokines, reduce the integrity of the intestinal epithelial barrier[89], increase susceptibility and duration of infections[101], and increases depressive symptoms[102]. Lower serum Zn^{2+} correlates with increased systemic inflammation and higher mortality in human models of sepsis[103–105]. In humans and mice, Zn^{2+} deficiency increases circulating levels of proinflammatory cytokines, while Zn^{2+} supplementation suppresses inflammation[94,106–108].

Cellular Zn^{2+} homeostasis is perturbed in several tissues in response to inflammatory stresses[106,109–111] and can result in clinically significant Zn^{2+} deficiency that, if prolonged, can perpetuate inadequate immune responses affecting a large number of inflammatory diseases. Zinc adequacy is required for optimal inflammation control and also plays a significant role in the survival and proliferation of innate and adaptive immune cells[99,112]. This feed forward loop where inflammation can lower zinc status and lower zinc status can increase inflammation, implies that the required zinc intake will change depending on one's inflammation status in order to restore homeostasis. The interplay between inflammation status and zinc status is still an active area of research.

1.8 Zinc in the Immune System

Zinc is essential for the proper function of all organ systems but the immune system is particularly vulnerable to deficiency[101,113,114]. Zinc deficiency impacts both the innate and the adaptive immune cells (Figure 1). Zinc is capable of modulating the differentiation, cell signaling, proliferation and survival of several myeloid and lymphoid cell types. Within the innate immune cells zinc is required for the differentiation of monocytes, polymorphonuclear cells, dendritic cells, mast cells and natural killer cells. Adaptive immune cells, T- and B- lymphocytes, are negatively impacted during zinc deficiency in their ability to undergo clonal expansion and differentiation. Differentiation and proliferation can be affected by decreased effectiveness in hormone signaling such as is the case of the hormone thymulin, the nonapeptide, which is responsible for Th1 and Th2 differentiation and also requires zinc for its activity[115]. Mild zinc deficiency is enough to reduce the proliferation of Th1 and Th2 cells in humans while moderate to severe deficiency results in thymic atrophy. Conversely, calcitriol-dependent differentiation of monocytes from myeloid precursor cells is enhanced in zinc deficient conditions indicating that zinc acts as a negative regulator of monocyte differentiation[116].

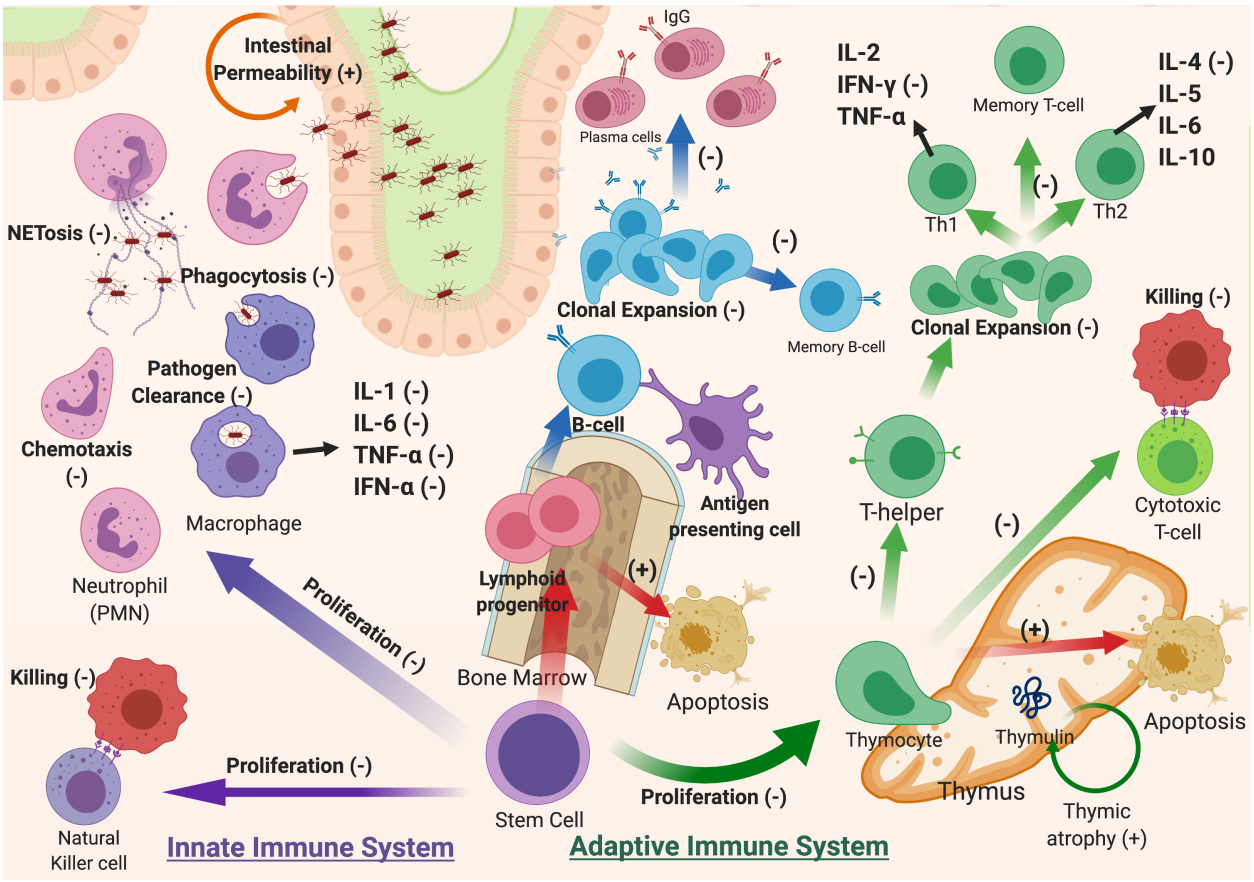

Figure 1.1 The impact of zinc deficiency on the development and function of select immune cells. (-) indicates that the process is decreased in deficiency and (+) denotes an increase in the process in zinc deficiency.

Within innate immune cells, phagocytosis and killing of invading pathogens is impacted by zinc deficiency *in vitro* and *in vivo*[117]. Chelation of zinc using a cell permeable zinc ionophore, TPEN, reduces chemotaxis and phagocytosis of beads by cultured macrophages[118], suggesting that zinc deficiency may compromise basic macrophage functions. One study on zinc deficient mice infected with *Trypanosoma cruzi*, a small protozoan parasite that causes Chagas disease[119], found that the number of macrophages that contained the parasite was reduced compared to zinc sufficient mice. To determine whether the macrophages were better at killing the parasite or had a reduced phagocytic capacity, isolated peritoneal macrophages from the mice were grown under zinc deficient or sufficient conditions, infected with *T. cruzi,* and then internalized parasites per macrophage were counted. They found that severely and moderately zinc deficient macrophages had fewer internalized parasites and

even the mildly zinc deficient macrophages were less capable of killing the parasite. Administration of supplemental zinc completely restored phagocytic capacity while other metals failed to have any effect.

Phagocytosis in neutrophils is also decreased in zinc deficiency and enhanced by supplementation[117]. Neutrophils kill intracellular bacteria through the production of ROS including superoxide anion which is produced from NADPH oxidase. NADPH oxidase is inhibited both by zinc deficiency and zinc excess[120–122]. ROS production is also enhanced in macrophage upon reduction of zinc in the media or chelation with TPEN, and suppressed upon the addition of excess zinc[61,123].

Zinc is essential within the signaling cascade that produces proinflammatory cytokines IL-1ß, IL-6, IL-10 and TNF-α in macrophages, as chelation of intracellular zinc abrogates their release[124]. Zinc is also essential in the regulation of inflammatory signals in the body. Low levels of proinflammatory circulating cytokines TNF-α and IL-6 are seen during mild zinc deficiency in a variety of conditions such as obesity[125–128], rheumatoid arthritis[114], atherosclerosis[129], diabetes mellitus[130], age related zinc deficiency[131,132], and supplementation of zinc reduces those signals[94,108,111]. Zinc influences a variety of signaling mechanisms in inflammation but is also important for the integrity of the epithelial barrier in the gut which keeps out microbial pathogens and proinflammatory molecular patterns[89]. The contributions of zinc to inflammation control may play a role on both fronts. Zinc is an inhibitor of NF-κB signaling[113,133] which is a required signaling pathway for response to stress stimuli including the production of proinflammatory cytokines in myeloid cells[134]. NF-κB is composed of a protein complex of transcriptional activators, homo- or hetero- dimers of RelA(p65), NF-κB1(p50), or NF-κB2 (p52), bound by the inhibitory protein IκB. When IκB is bound it obscures the nuclear localization signal of the NF-κB complex, maintaining cytosolic localization. Stress stimuli such as proinflammatory cytokine signaling, bacterial or viral molecular patterns, free radical damage, or damage associated molecular patterns, activate IκB kinase (IKK) which phosphorylates IκB, targeting it for ubiquitination and proteasomal degradation. Dissociation of IκB allows the NF-κB complex to translocate to the nucleus and initiate transcription of target genes. Zinc is a potent and specific inhibitor of IKKß by directly binding the C-lobe of the kinase domain[133]. Zinc levels are tightly

controlled in cells, but activation by a stress stimulus promotes the upregulation of a zinc importer[133,135,136] which increases intracellular zinc content and can act as a negative regulator of NF-κB signaling. Zinc deficiency augments IKK activity in mice in a cecal ligation and puncture model of sepsis and increases the inflammatory response[133]. Supplemental zinc may be responsible for the reduction of inflammatory signaling through this mechanism.

Inflammatory stresses in the liver such as turpentine stress, LPS exposure, or proinflammatory cytokines cause upregulation of Zip14 in hepatocytes[106,135,137]. Sequestration of serum zinc by the liver during inflammation causes acute hypozincemia[138]. Acute decrease in circulating zinc is different than a chronic deficiency, and as noted earlier, zinc status is not always well correlated with serum zinc concentration. However, low circulating levels of zinc correlate with higher mortality in humans with sepsis[103] and contribute to oxidative damage and inflammation[139]. Acute inflammation can become chronic through the establishment of systemic infections that are stable or recurrent as is the case for systemic pathogens such as *Salmonella*[65]. Hypozincemia is thought to be a host defense response that may serve the purpose of reducing availability for pathogenic microbes and providing more zinc for cellular needs.

Hepatocyte response to stress was first observed during administration of IL-1ß or LPS to mice, both MT2 and Zip14 mRNA levels were significantly upregulated[106,138,140]. IL-6, the main proinflammatory cytokine in response to LPS, was responsible for upregulation of Zip14 and hypozincemia[135]. Knockout of inducible nitric oxide synthase (iNOS), a downstream gene of IL-6 and NF-κB[141], also blocked the LPS mediated Zip14 induction, while treatment of isolated mouse hepatocytes with NO donor S-nitroso-N-acetylpenicillamine increased Zip14 expression[136]. Zip14 knockout mice display significantly decreased intracellular zinc and higher serum concentrations of IL-6, TNF-α, and IL-10[106]. Zip14 mediated zinc transport plays an important role in resolving ER stress in hepatocytes[137]. In pharmacological- or high-fat-diet- induced ER stress, proapoptotic ER-stress markers, phospho-eIF2α, ATF4, and CHOP, are increased concomitant with an increase in apoptosis and hepatic steatosis in the liver of Zip14 KO mice compared to WT mice. Through chromatin immunoprecipitation it was shown that Zip14 upregulation occurred through transcription

factors ATF4 and ATF6α[137]. Together these studies show that Zip14 is a cytokine regulated gene, is the main transporter responsible for hepatic zinc uptake during inflammation, and is transcriptionally activated by ATF4 and ATF6.

Zinc redistribution and hypozincemia during inflammation mediated by Zip14 zinc transport plays a protective role for the liver to adapt to ER stress and resist apoptosis but the immediate consequences of acute hypozincemia during inflammation for the rest of the immune system is still unknown. Other cells within the body respond to stress and inflammatory signals with a similar upregulation of Zip14[142]. White adipose tissue has the highest degree of upregulation of Zip14 of any tissue within the body during inflammation[127,143]. Macrophages upregulate Zip14 in response to LPS[144]. Zip14 expression in those cell types may be regulated in the same manner as hepatocytes and the intracellular zinc may also play a protective role during inflammatory insults. Zinc plays an essential role in immunity and host defense during insults from microbial pathogens and despite the complexity of zinc regulation, new insights continue to highlight its importance for human health. The role of zinc regulation in primary immune competent macrophages during infection from *Salmonella* infection is explored further in Chapter 4.

Chapter 2

Live Cell Imaging of *Salmonella* Effector Proteins in Primary Macrophages Reveals Distinct Phenotypes

2.1 Abstract

Intracellular bacterial pathogens, such as *Salmonella*, express an array of effector proteins that are translocated into mammalian host cells to manipulate host proteins and remodel the intracellular environment. Effector proteins are required for bacterial virulence but many of their functions or functional targets within the host still remain unknown, highlighting a need for tagging and visualization techniques that can be used to identify complex interactions with host cells. We previously adapted a split-GFP fluorescent protein system for tagging and visualizing effector proteins in live epithelial cells. Here, we broadened the applicability of this system by creating a generalized expression platform to tune the expression and the brightness of the tag with different promoters or tandem repeats of the tag. Additionally, we improved our ability to detect GFP fluorescence complementation of new effectors by creating an orthogonal nuclear localized transfection marker that is co-expressed with GFP1-10 in the host cell. We show *Salmonella* effector protein localization in live primary bone marrow derived macrophages for the first time and find that the localization of effector proteins is different between macrophages and epithelial cells.

2.2 Publication Status and Author Contributions

Young, A.M., Minson, M, McQuate, S.E., Palmer, A.E., "Optimized Fluorescence Complementation Platform for Visualizing *Salmonella* Effector Proteins Reveals Distinctly Different Intracellular Niches in Different Cell Types" *ACS Infectious Diseases*, 2017

A.M.Y. designed the experiments, A.M.Y., M.M., S.E.M. carried out the research, A.M.Y., A.E.P. and M.M. wrote the manuscript.

Portions of this chapter were reproduced from this publication.

2.3 Introduction

In order to invade and survive in multiple types of host cells, *Salmonella* and similar intracellular pathogens must adapt to diverse environments. The coordinated action of translocated effector proteins enables pathogens to modulate host cell signaling and transport processes to generate a protective niche, resulting in a highly dynamic interplay between the bacteria and the host cell[6,66,145]. Unraveling the elements of this complex relationship and elucidating the roles of individual effector proteins in establishing *Salmonella*'s niche requires techniques that monitor bacteria together with translocated effector proteins within the different types of infected host cells, as different modes of infection and different intracellular environments may require different subsets of effector proteins. Live cell imaging holds enormous potential for defining the intracellular phenotypes of *Salmonella* infection at the single cell level, tracking the fate of intracellular bacteria and dynamic localization of effector proteins. The modular platform for split-GFP labeling developed in this work enables the amplification of fluorescent signals by tuning effector protein expression level or multimerizing the tag. Additionally, expression of GFP1-10 along with a blue nuclear marker enables facile identification of GFP1-10 expressing cells and aids in verification of low complementation signals. Using these new tools, we visualized a number of different translocated effector proteins over many hours in living cells upon infection. Importantly, we demonstrate the ability of this tool to illuminate the intracellular niche in both epithelial cells and primary macrophages.

2.4 Split-GFP Labeling Platform to Visualize Translocated Effector Proteins in Live Host Cells

To facilitate visualization of Salmonella effector proteins during infection of live cells a modular expression platform was generated. The plasmid-based platform features an exchangeable promoter region, effector, and a GFP11 tag as well as a constitutively expressed fluorescent protein (FP) that serves as a bacterial marker (Fig. 2.1A). Each feature of the platform can be exchanged by standard molecular cloning techniques (Fig. 2.1B). The pACYC177 plasmid was chosen as the backbone because unlike pAYCY184, pWSK29 or plasmids derived from pBR322, it doesn't interfere with growth or pathogenicity when expressed in *Salmonella*[146,147].

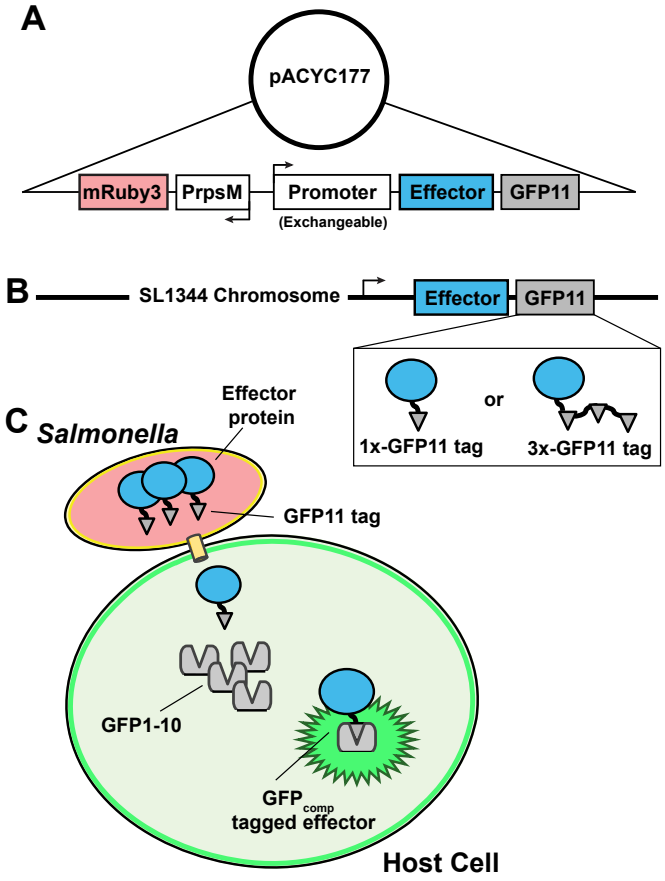

Figure 2.1 Platforms for labeling *Salmonella* effector proteins with split-GFP
(**A**) The plasmid based effector protein-labeling platform with exchangeable promoters, effectors, and tags including a constitutive mRuby bacterial marker. (**B**) Chromosomally integrated effector-labeling using 1X-GFP11 or 3X-GFP11 tags. (**C**) Split-GFP effector protein- labeling to fluorescently tag and visualize effector proteins during infections of live host cells.

2.5 Measuring Effector Protein Expression and Split-GFP Complementation in Bacteria

One of the weaknesses of the previously developed split-GFP system was the inability to rapidly screen for fluorescence complementation in different expression contexts. Thus, we encountered limitations with this original system when we were unable to detect a number of new effector proteins, including SseF, SseG and SlrP, under their endogenous promoters and could not determine whether this issue was due to low expression, poor complementation due to steric constraints, perturbation of translocation, or rapid protein turnover in the host cell. To address this, we created a bacterially optimized version of GFP1-10 to be orthogonally expressed in *Salmonella* that also express a GFP11 tagged effector. Complementation within bacteria allows evaluation of the brightness of GFP_{comp} signal as an early test to determine which version of a new effector protein will be most suitable for imaging with our labeling platform. This enabled direct comparison of GFP11-tagged effector proteins in our platform that were tagged under different conditions such as plasmid expressed and driven by their native promoter, or a generalized promoter, or chromosomally integrated. Because fluorescence complementation occurs within the bacteria, the GFP_{comp} signal does not dilute due to loss of the effectors from secretion since the fully formed GFP occludes the secretion apparatus[7]. This assay enables comparison of effector protein expression levels under the generic *steA* promoter versus an effector's endogenous promoter versus expression from its endogenous locus upon integration of the tag into the chromosome, to identify the best approach for visualization of effector proteins in the context of infection.

Salmonella strains expressing an effector tagged with GFP11 were co-transformed with GFP1-10 and the GFP_{comp} signal intensity was quantified in individual bacteria as a measure of effector protein expression and split-GFP complementation (Fig. 2.2, Fig 2.3). We observed complementation in bacteria for SteA, SlrP, SseF, SseG, and SopA when these effector proteins were expressed from a plasmid under control of the generic *steA* promoter (Fig. 2.2C, Table 2.1). SteA has been tagged previously, while the other four effector proteins have never been tagged for visualization during live cell infection. SopA showed high split-GFP_{comp} signals that were comparable between the endogenous

and the *steA* promoter. SlrP, SseF, and SseG all gave significantly higher split-GFP$_{comp}$ signals when expressed under the *steA* promoter compared to their endogenous promoters, suggesting that the *steA* promoter may be stronger than their endogenous promoters. Consistent with this notion, a previous study using a firefly luciferase reporter system to compare effector protein expression levels found that SseG and SlrP express at low levels compared to a handful of other SPI-2 encoded effector proteins.

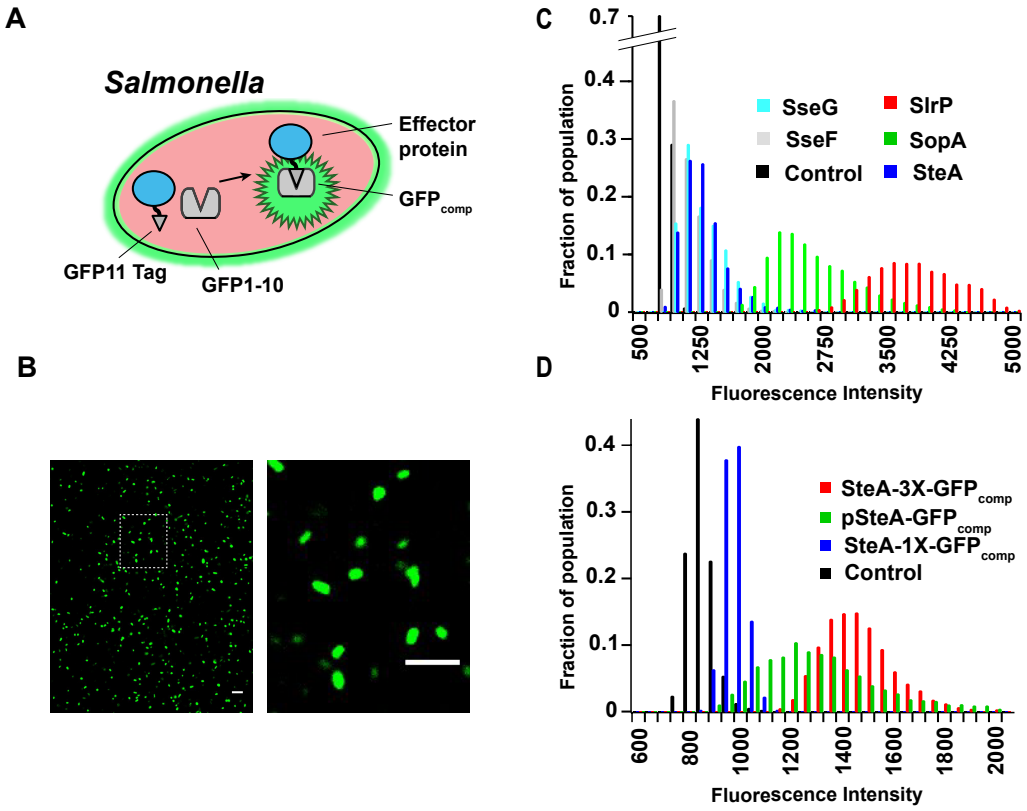

Figure 2.2 Bacterial expression assay to validate effector protein expression and split- GFP complementation efficiencies.
(**A**) Chromosomally integrated or plasmid-based expression of GFP11-tagged effectors are expressed in bacteria alongside GFP1-10. The GFP$_{comp}$ fluorescence signal is used to report on effector protein expression efficiency. (**B**) Representative image of GFP$_{comp}$ fluorescence signal within bacteria used for automated ROI selection and analysis. Right image is a zoom in of box indicated by dashed line. (**C**) Representative effector protein expression and GFP- complementation levels for select bacterial strains using the plasmid based labeling platform. (**D**) The expression and GFP-complementation levels for SteA using chromosomal verses plasmid based labeling platforms. Results represent the pooled total of 3 biological replicates, including 4 technical replicates per condition, n total ≥ 1000 bacteria (ROI) per condition.

The intensity of the fluorescence signal varied based on the expression context (Fig. 2.2D, Table 1). As expected, for all effector proteins, split-GFP signal intensities were higher for plasmid-based expression. Fig. 2.2D shows the data for plasmid-based expression of SteA (pSteA-GFP_{comp}) versus chromosomal expression (SteA-1X-GFP_{comp}). The data for other effector proteins are presented in Figure 2.3. The intensity of the fluorescence signal was amplified by including a 3-fold repeat of the GFP11 tag (Fig. 2D, Table 1). All effector proteins showed an increase in complementation signal intensity for the 3X-GFP11 tag compared to 1X-GFP11 (Fig. 2.3), for example SteA showed an increase in signal intensity that was approximately 3-fold, indicating near stoichiometric complementation.

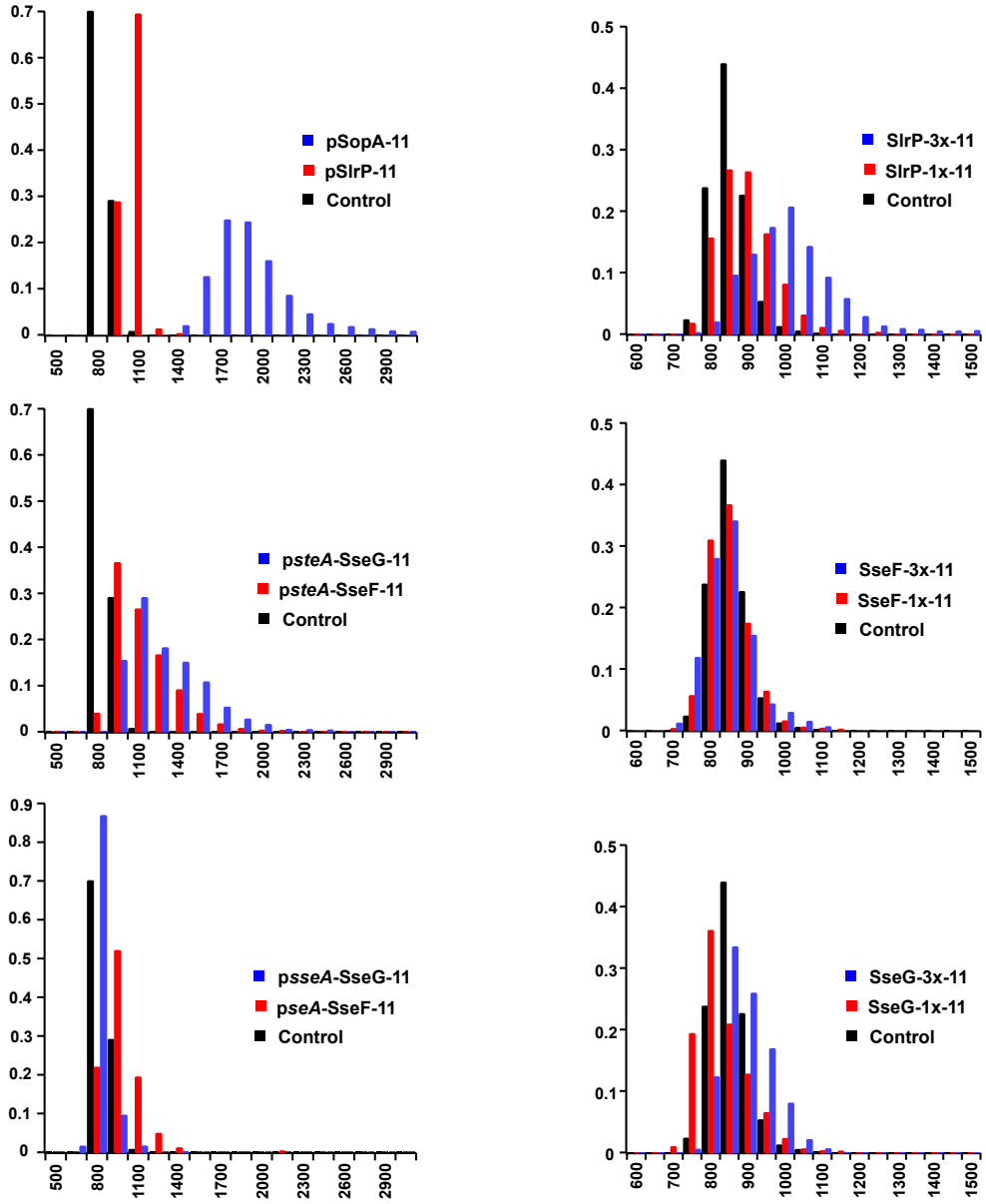

Figure 2.3 GFP_{comp} intensity profiles for effectors tested with the bacterial expression assay.

Chromosomal or plasmid based GFP11-labeled effectors are expressed alongside GFP1-10, which is expressed on a separate plasmid, within bacteria. GFP_{comp} fluorescence signal is used to report on effector protein expression efficiency, the expression and GFP-complementation levels are compared for the *Salmonella* strains expressing GFP11 labeled effectors generated in this study.

Context	Promoter	Effector	Expression	Visualization in Host Cell
Plasmid	steA	SteA	++	Y
		SlrP	++++++	Y
		SseF	+	Y
		SseG	++	Y
		SopA	++++	N
	slrP	SlrP	+	N
	sseA	SseF	+	Y
	sseA	SseG	-	N
	sopA	SopA	+++	N
Context	Effector	Tag		
Chromosome	SteA	1X-GFP11	+	Y
		3X-GFP11	++++	Y
	SlrP	1X-GFP11	-	N
		3X-GFP11	+	N
	SseF	1X-GFP11	-	N
		3X-GFP11	-	N
	SseG	1X-GFP11	-	N
		3X-GFP11	-	N
Plasmid	PipB2	SNAP	+	-

Table 2.1 Comparison of Bacterial expression assay and Split-GFP complementation in infected host cells.
The bacterial expression assay from Figure 2.2D was quantified as follows: − represents no detection of fluorescence signal above the negative control, + is the major peak of fluorescence signal within a population and is within 1 standard deviation of the negative control, +++ is within 3 standard deviations of the negative control, and so on. Visualization within infected host cells was assessed for each condition between 4 and 24 h post-infection, where Y indicates that the effector-GFP_{comp} signal was detectable above background and N indicates no detectable GFP_{comp} signal.

2.6 Creation of a Transfection Marker for Detecting GFP1-10 in Host Cells

Visualization of effector proteins in host cells during infection using the split GFP system is influenced by the effector protein concentration, the efficiency of secretion, the accessibility of the GFP11 tag to the host cytosol where the GFP1-10 is expressed and the concentration of GFP1-10. When we began to apply the split GFP system to new effectors that had never been visualized, we searched for a way to improve our ability to accurately identify putative effector-GFP_{comp} signal that was low compared to the background. This was especially important for imaging in primary bone marrow derived macrophages (BMDMs) since transient transfection of those cells produces much less protein and thus less fluorescence than is typically seen in cells lines. Additionally, we sought to

identify cells expressing GFP1-10 that had not yet been infected so that we could image them throughout the infection time course. All *Salmonella* expressing an effector labeled with our platform also co-express a constitutive mRuby3 marker to facilitate identification of infected cells. But because GFP1-10 is non-fluorescent until complementation with GFP11, we lacked a way of successfully identifying transfected cells expressing GFP1-10.

To address this, we created a bicistronic expression plasmid that expressed GFP1-10 and a nuclear localized (NLS) mTagBFP2 under the control of an internal ribosomal entry site (IRES) to aid in identification of cells expressing GFP1-10. In order to select which nuclear localization signal to use, I tested 2 different versions of nuclear localized mTagBFP2. I used the two classical monopartite NLSs, SV40 large T antigen NLS (PKKKRKV)[148] and the c-Myc NLS (PAAKRVKLD)[149]. I added an an N-terminal SV40 NLS, and a C-terminal c-Myc NLS to mTagBFP2. I imaged each construct after transient transfection in HeLa cells. The N-terminal SV40 NLS mTagBFP2 showed brighter fluorescence intensity in the nucleus and lower signal in the cytosol than the C-terminal cMyc-mTagBFP2 NLS indicating that there was better nuclear targeting (Figure 2.4).

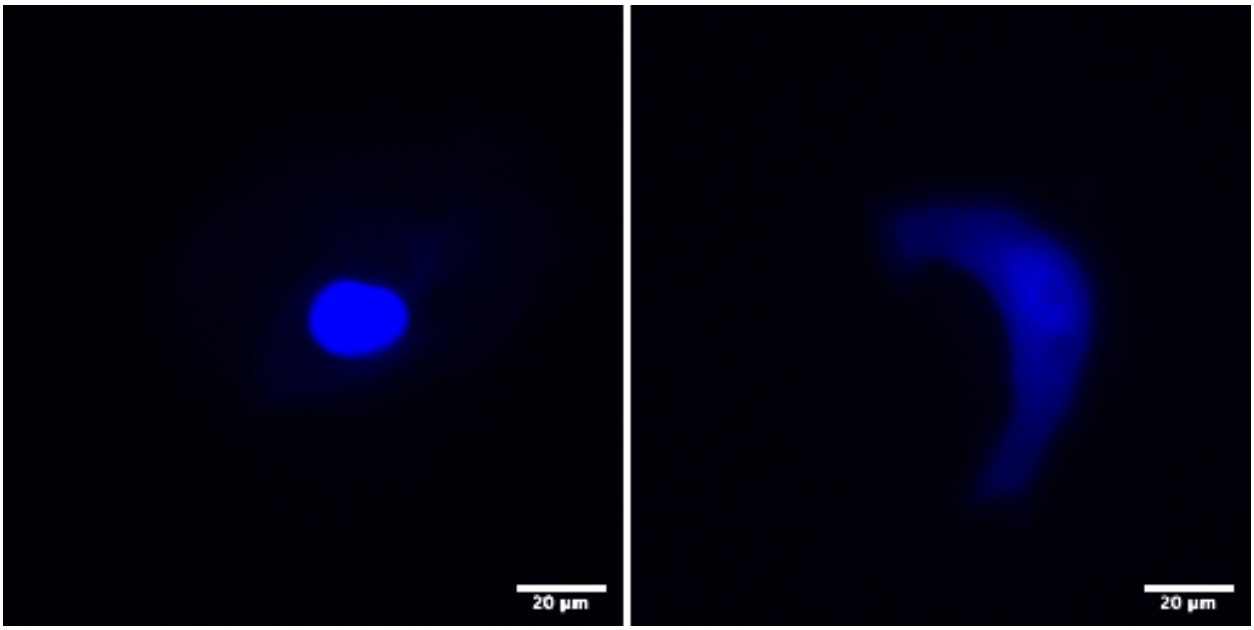

Figure 2.4 N-terminal SV40 NLS mTagBFP2 in pcDNA3.1
(**Left**) shows better nuclear targeting and brightness than C-terminal c-Myc mTagBFP2 NLS (**Right**). The fluorescence signal range is the same in both images.

We found that the poly adenylation (polyA) signal is required for proper expression of the second cistron under the control of the IRES[150]. Initial imaging showed very little expression of the second cistron under the control of the IRES. The PiggyBac Dual cistronic vector (PB513B-1) does not contain a polyA signal after the multiple cloning sequence (MCS) but rather incorporates the SV40 polyA signal much further downstream after the second promoter and the puromycin selection marker. An additional polyA signal was added to the 3' end of the NLS-mTagBFP which restored expression of the IRES_NLS-mTagBFP2 (Figure 2.5)[151]. The expression strength of an IRES is enhanced by the proximity of a polyA signal.

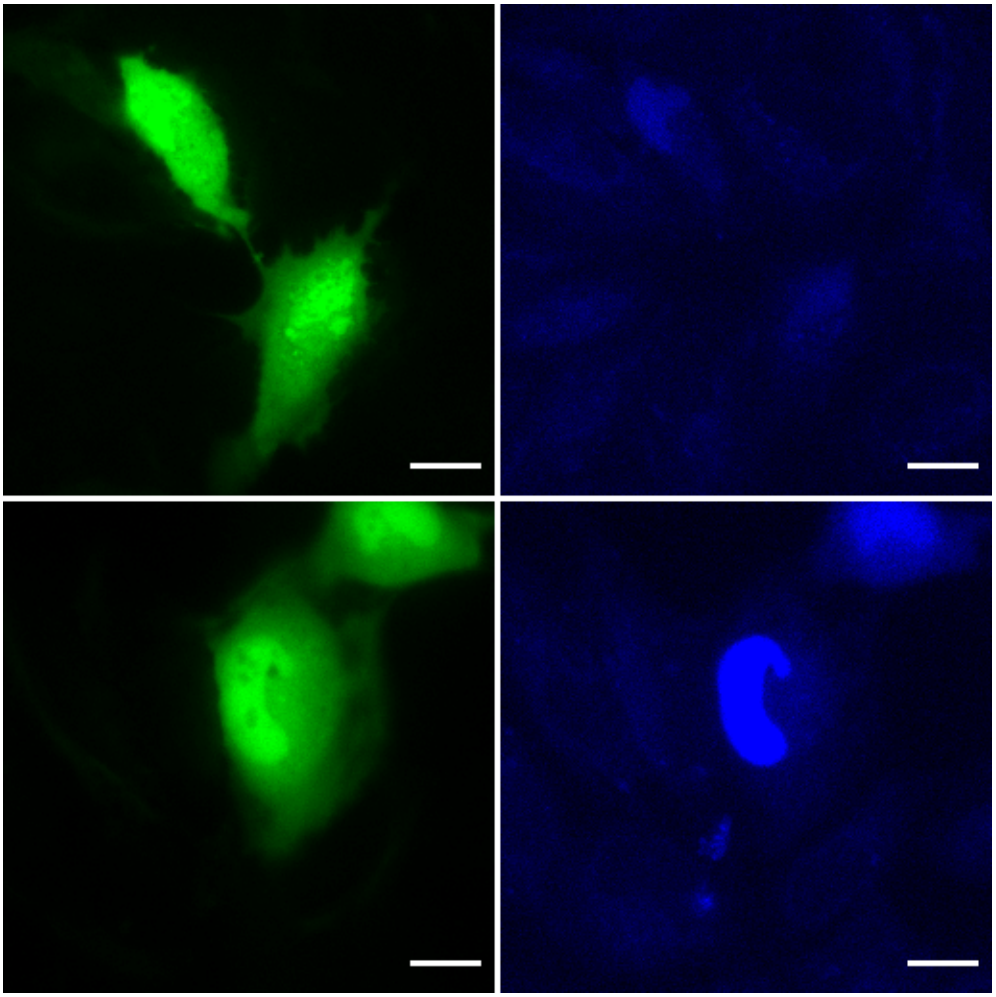

Figure 2.5 HeLa cells coexpressing GFP11-Erk1 and PiggyBac-GFP1-10_IRES_NLS-mTagBFP2
without the 3' polyadenylation signal (**Top**) or with the 3' polyadenylation signal included (**Bottom**). The polyA signal restores expression of the BFP expressed under the IRES. Scale bar is 20 μm. The GFP and BFP fluorescent signal range are set to be the same between the bottom and top image.

2.7 Visualization of Effector Proteins in Live Host Cells

Based on the bacterial expression assay, we anticipated being able to visualize SteA, SlrP, SseF, SseG, and SopA when expressed from a plasmid under control of the SteA promoter. Indeed, we observed all of these effectors except SopA upon live cell infection of HeLa cells (Table 2.1, Fig 2.2A). Cells were imaged beginning at 4 hours post infection, however the labeled effector proteins were not observed until approximately 7 hours post infection. SseF and SseG both localized to the SCV and associated filaments in live HeLa cells for the duration of 7-28 hours post infection, in agreement with previous immunofluorescence-based studies[151,152] SseF and SseG containing filaments were highly dynamic and displayed an increase in effector-GFP_{comp} signal over time, suggesting these effectors accumulate in the host cell over time (Fig. 2.6). SlrP was observed from 9-28 hours post infection and appeared diffuse in the cytosol of the host cell. This result agrees with a 2009 study that identified the cytosolic host cell protein thioredoxin as an interaction partner for SlrP[153]. Expressed under the steA promoter, SlrP-GFP_{comp} signal appeared to increase in the host cell cytosol over time (Fig. 2.6). To our knowledge, this is the first time that these three effector proteins have been visualized live, over time, in the context of infection.

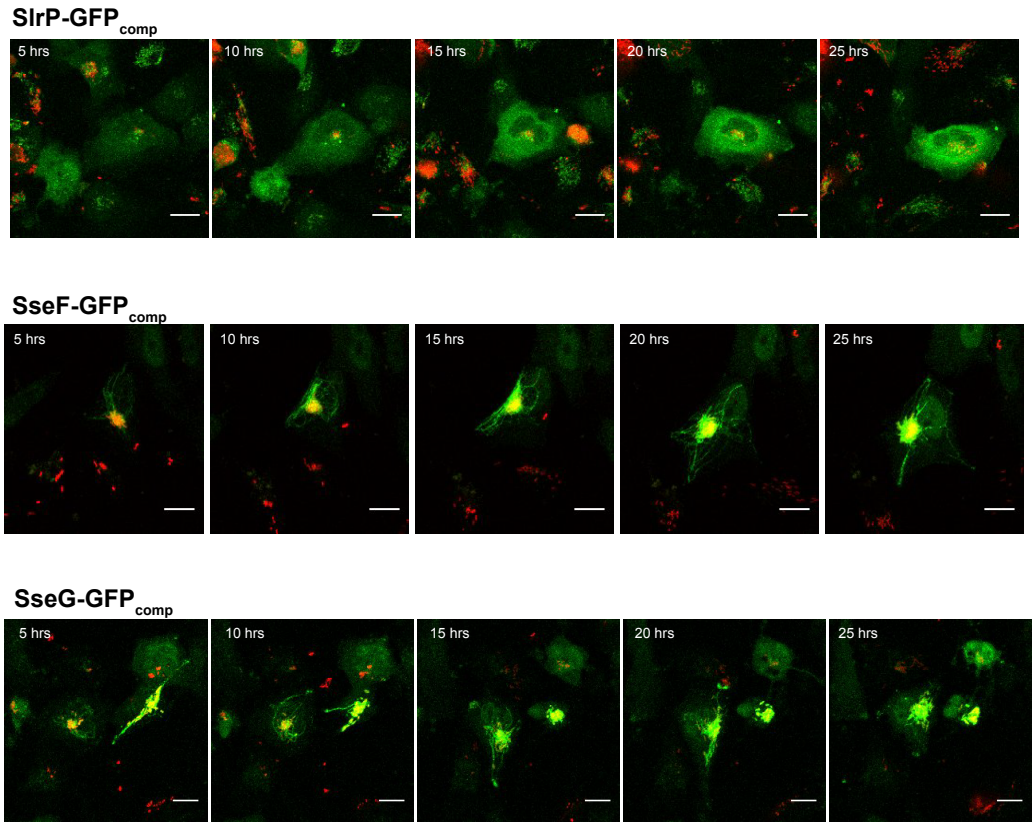

Figure 2.6 Time course images for GFP_{comp}-labeled effector proteins in infected HeLa cells. Snap shots at distinct time points from long term imaging of live infections are represented to show the development of GFP_{comp} signal for different labeled effector proteins over time. Images are an overlay of red fluorescence (Salmonella) and green fluorescence (effector-GFPcomp). All images for a given experiment are scaled to the same intensity range to permit direct comparison of relative brightness. Scale bars are 20 µm.

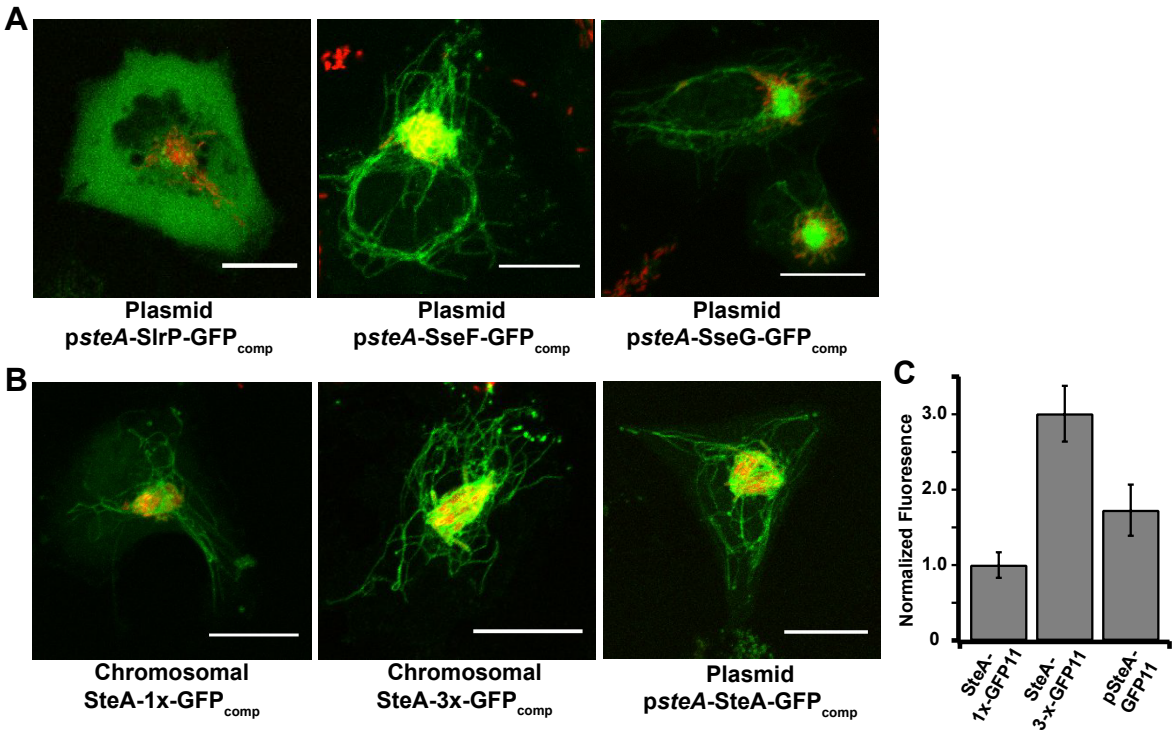

Figure 2.7 Visualizing translocated effector proteins inside live host cells.
(**A**) The effector proteins SteA, SlrP, SseF, and SseG were expressed under the steA promoter for visualization in HeLa cells 16-20hrs post infection. The green channel is GFP_{comp} labeled effectors and the red channel is *Salmonella* constitutively expressing mRuby3. Scale bars represent 20µm. (**B**) Plasmid and chromosomal based expression of SteA-GFP_{comp} or SteA-3xGFP_{comp} is visualized in HeLa cells 18hr post infection. GFP fluorescence was acquired for all images using identical settings and all images are scaled to the same intensity. Scale bars represent 20µm. (**C**) Average fluorescence intensities of SCV localized SteA-GFP_{comp} are compared for the plasmid based labeling platform for SteA-GFP11 verses chromosomal expression of SteA-1X-GFP11 and SteA-3X-GFP11. Fluorescence signal intensities are normalized to chromosomal SteA- 1xGFP_{comp}. n = 20 per condition. Error bars are SD.

As predicted from the bacterial expression assay, only SteA and SseF were detected when expressed from a plasmid with their endogenous promoters. SseF localization was consistent between endogenous or *steA* driven expression, with an increase in the detectable GFP_{comp} signal for *steA* driven expression. The bacterial expression assay also allowed us to predict that the only effector likely to be observed under native transcriptional and translational regulation upon chromosomal integration of the GFP11 tag was SteA. Consistent with this prediction, SteA was the only chromosomally labeled effector protein successfully visualized within infected host cells. SseF, SseG and SlrP are likely expressed too low under endogenous conditions for visualization within infected host cells with split-

GFP. We found that multimerizing the GFP11 tag boosted the fluorescence signal in mammalian cells (Fig 2.2B,C, Fig. 2.7B). Finally, although chromosomal expression of SlrP-3X-GFP_{comp} and SteA-1X-GFP_{comp} gave comparable split-GFP complementation efficiencies in the bacterial expression assay, we were not able to detect SlrP-3X-GFP_{comp} in infected cells. We speculate that this could result from the fact that SteA protein is concentrated on the SCV, while SlrP is diffuse in the cytosol, leading to less contrast over the background fluorescence of cells.

2.8 SseG Localization is Mediated by SseF

Given our ability to visualize SseG in live host cells, we set out to examine how the localization of SseG depends on SseF. SseF and SseG have been shown to physically and functionally interact to coordinate SCV localization and maintenance[151,154–156]. These proteins have been suggested to tether the SCV to the Golgi by jointly interacting with the host Golgi network associated protein ACBD3[156]. SseF and SseG have also been shown to associate with endocytic membranes and microtubules[154,157] and are hypothesized to redirect host exocytic traffic from the Golgi[151] by recruiting dynein to the SCV[158]. Transfected SseG showed a scattered distribution in a majority of cells (80%) that was globular in appearance and co-localized with the trans-Golgi network marker TGN46[157]. In a minority of cells, transfected SseG was filamentous, co-localized with microtubules, and appeared similar to translocated SseG localization during infection[157] suggesting differential localization when SseG is expressed alone versus translocated with the rest of the effector cohort. Given these observations, we set out to determine whether the difference in localization was due to the mode of delivery (transfection versus T3SS-mediated translocation) or the absence of SseF.

To examine the localization of SseG in the absence of SseF during infections, we generated a *Salmonella* strain containing an isogenic *sseF/sseG* deletion while expressing SseG-GFP11 under the control of the *steA* promoter on our plasmid based platform. SseG localized to the SCV in the presence and absence of SseF (Figure 2.8A). However, in the absence of SseF there was a globular population of SseG at the host cell periphery (Figure 2.8A) in approximately 70% of cells (n = 65), whereas less than 10% of cells display peripheral SseG in the presence of SseF (n = 73) (Figure 2.8B). Thus, in the absence of SseF, T3SS translocated SseG displays a localization pattern similar to transfected SseG,

suggesting that SseF is required for proper SseG localization. There was also a change in the morphology of filaments emanating from the SCV in the absence of SseF, where SseG containing filaments appeared either punctate or thinner than in WT infections (Figure 2.9). Thin LAMP1-associated filaments have been observed for infections using *Salmonella* strains lacking either SseF or SseG[45]. Additionally, Krieger *et al.* 2014 showed that a subset of SCV associated filaments are composed of double membranes that enclose portions of host cell cytosol and cytoskeletal filaments within its inner lumen and that the formation of these double membranes requires the function of SseF and SseG[159]. Our results are consistent with the observation that SseF and SseG are involved in acquiring and redirecting host cell endosomal compartments and exocytic traffic to maintain the SCV and associated filaments[154,160], and that they physically interact with one another[155,156].

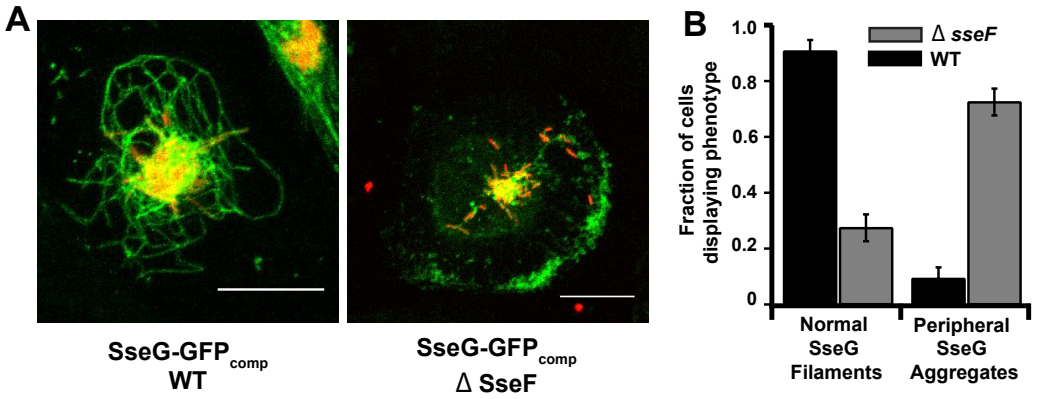

Figure 2.8 SseG gathers at the host cell periphery in the absence of SseF.
(**A**) representative images of infected HeLa cells at 14 h post-infection displaying localization of SseG-GFP$_{comp}$ in the presence of SseF (WT, left) and the absence of SseF (ΔsseF, right) (**B**) average fraction of infected cells that display SseG-GFP$_{comp}$ uniformly distributed across filaments compared to cells that contain SseG-GFP$_{comp}$ aggregates at the host cell periphery. N total = 65 cells (ΔsseF), 73 cells (WT). Error bars are SD across three separate infection experiments.

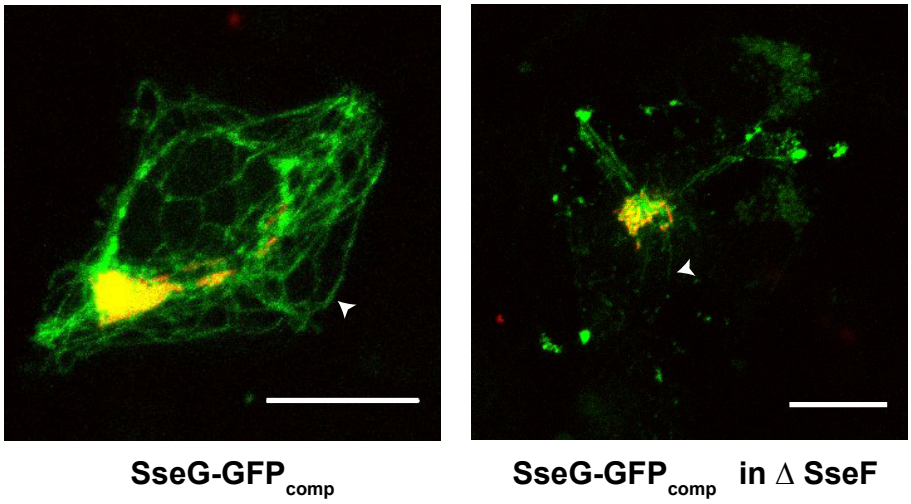

Figure 2.9 SseG filaments are thin and punctate in the absence of SseF.
HeLa cells expressing GFP1-10 were infected with *Salmonella* strains expressing mRuby3 and SseG-GFP11, in the presence or absence of SseF. Representative images of complementation from 16 hours post infection are shown for SseG-GFP$_{comp}$ filaments in the presence of SseF (**left**) and in the absence of SseF (**right**). Red is *Salmonella* and green is SseG-GFP$_{comp}$. The arrows indicate a select SseG associated filament. Scale bars are 20 μm.

2.9 SlrP is Localized to the Cytosol in Infected Host Cells

One advantage of the split-GFP system is the ability to target the GFP1-10 to subcellular compartments in the host cell to address questions about the specific localization of effector proteins. By comparing fluorescence complementation signals from split-GFP where the GFP1-10 fragment is directed to the cytosol with a version targeted to an organelle, we can distinguish whether an effector protein resides inside an organelle versus associated at the cytosolic face of the organelle. Additionally, if an effector protein changes localization at different stages of infection, as has been demonstrated for SopB[161], these dynamic changes in localization can be visualized over time.

SlrP was used as a model to establish our system within host cell organelles because SlrP has been suggested to have dual localization within the host, with populations of SlrP residing in the cytosol and the ER lumen. Motivated by the possibility of dual localization proposed by Bernal-Bayard *et al.* 2010[153], we aimed to distinguish two distinct populations of SlrP, one cytosolic and one ER localized,

as opposed to a dynamic population that changes localization at different stages of the infection process. To assess these scenarios, we carried out long-term imaging of live cells infected with *Salmonella* expressing SlrP-GFP11, from 4-28 hours post infection. To exclusively visualize ER populations of SlrP, we used an ER lumen localized version of GFP1-10 (ER-GFP1-10)[160]. Using ER-GFP1-10 together with the ER luminal protein disulfide isomerase tagged with GFP11[160], we first verified that split-GFP localized to the ER is able to recombine and recapitulate robust fluorescence in the environment of the ER lumen (Figure 2.10A). We were unable to detect signal for SlrP-GFP_{comp} in the ER lumen at any time 4-28hrs post infection (Figure 2.10C), but we consistently observed cytosolic complementation beginning at 7 hours post infection and continuing for the duration of imaging (Figure 2.10B). These results were observed for plasmid based expression of SlrP-GFP11 under the *steA* promoter as well as chromosomal expression of SlrP-1X-GFP11 and SlrP-3X-GFP11. Our results indicate that SlrP maintains a cytosolic C-terminus throughout 7-28 hrs post infection.

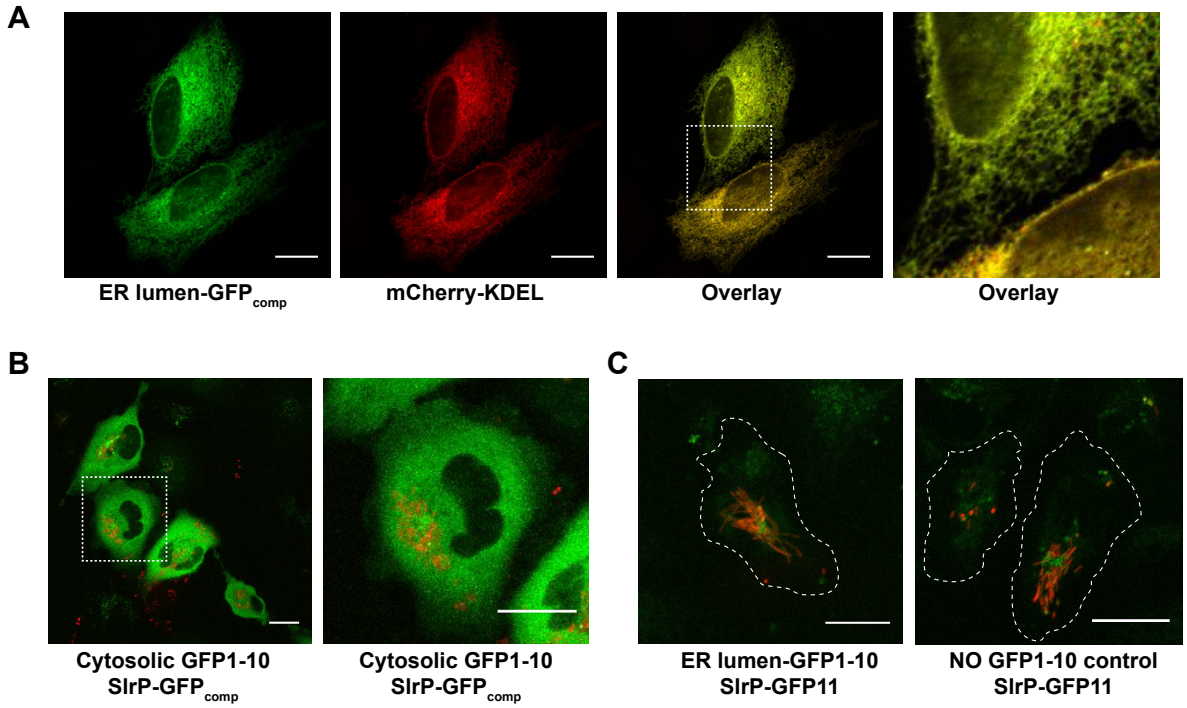

Figure 2.10 Defining subcellular localization of SlrP during live cell infections.
(**A**) Split-GFP components were localized to the ER lumen for complementation and fluorescence signal verification. (**B,C**) Host cells expressing cytosolic GFP1-10 (**B**) or ER localized GFP1-10 (**C**) were infected with *Salmonella* expressing SlrP-GFP11. (**B**) Representative infected cells transiently expressing cytosolic GFP1-10. Second panel shows a zoomed in perspective. (**C**) Representative infected cells with and without transient expression of ER localized GFP1-10. GFP fluorescence was acquired for all images using identical settings and all images are scaled to the same intensity. Scale bars represent 20µm.

2.10 Visualization of *Salmonella* Effector Proteins in Primary Macrophage Cells Using Split-GFP

Salmonella target both epithelial cells and macrophages during infection of a host organism and these niches give rise to very different host-pathogen interfaces[16,66,145,162,163]. For example, compared to epithelial cells, infected macrophages produce high levels of reactive oxygen species (ROS)[164] as well as reactive nitrogen intermediates (RNI)[163] that require the expression of SPI-2 and subsequent maintenance of the SCV to confer protection to intracellular *Salmonella* and enable the bacteria to survive and replicate. Alternatively, in epithelial cells *Salmonella* displays a bimodal lifestyle with a SPI-1 dependent population that is able to replicate to a greater extent in the cytosol compared to the

SPI-2 dependent population that resides in the SCV[66]. In fact, the mode of *Salmonella* internalization, the strategies used for intracellular survival, and the fate of the infected host cell varies based on cell type and depends on the temporal expression of *Salmonella* secretion systems[162]. For instance, macrophage cells take up bacteria through phagocytosis[67], whereas epithelial cells are forcibly modified by the action of SPI-1 translocated effector proteins in order to facilitate bacterial engulfment through macropinocytosis. Once intracellular, the role of *Salmonella* SPI-1 expression differs for the different host cell types. SPI-1 expression was shown to elicit innate immune responses in epithelial cells through mitogen-activated protein (MAP) kinase and NF-kB signaling[165], while producing the opposite effect in macrophage cells by suppressing levels of select chemokines and RhoA to reduce the host innate response[166]. Furthermore, SPI-1 expression delays apoptosis in epithelial cells through suppression of the c-Jun N-terminal Kinase (JNK) apoptotic pathway[167] and concomitant activation of Akt, a kinase that can exert pro-survival effects[168]. However, SPI-1 expression was shown to stimulate rapid cell death by Caspase-1 dependent pyroptosis in macrophages[169,170]. Collectively, these studies suggest that it would be valuable to be able to visualize effector proteins in live cell infection models for both epithelial cells and macrophages in order to define differences in the discrete roles effector proteins play in manipulating the host to establish distinct niches in different types of host cells. Moreover, many previous studies focused on macrophage infection used immunocompromised macrophage-like model cell lines (RAW 264.7), however there are central outstanding questions about the precise nature of the niche in primary bone marrow derived macrophage.

In this study we set out to develop approaches for using the split-GFP effector labeling platform in primary BMDMs to visualize effector proteins for the first time in live immune cells. BMDMs are notoriously challenging to transfect because they are differentiated, have decreased proliferation rates, and can be readily activated or undergo cell death upon exposure to foreign DNA. To overcome this limitation, we used Nucleofector™ Technology to express the GFP1-10 in primary BMDMs. To further facilitate visualization, we incorporated a blue nuclear marker (NLS-mTagBFP2) downstream of the gene encoding GFP1-10, and separated by an internal ribosomal entry site (IRES). This construct facilitated identification of transfected cells since the GFP1-10 is non-fluorescent in the

absence of complementation with GFP11. Nucleofection of GFP1-10-IRES-NLS-mTagBFP led to identification of transfected cells via visualization of blue nuclear fluorescence and confirmation of split-GFP complementation via co-transfection of an ERK-GFP11 positive control (Figure 2.11).

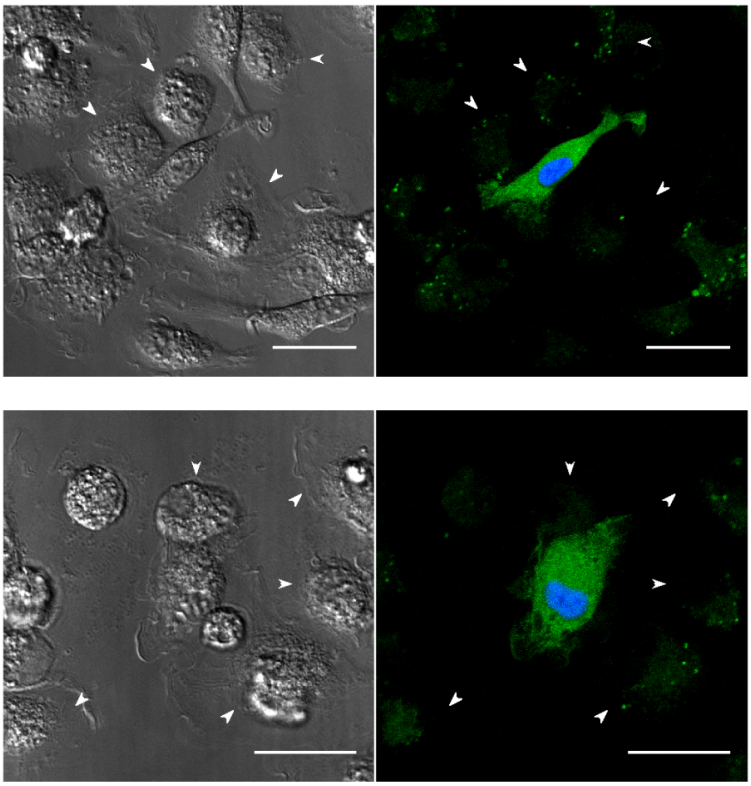

Figure 2.11 Fluorescence images demonstrating split-GFP fluorescence complementation in cells nucleofected with GFP1-10-IRES-NLS-mTagBFP.
Fluorescence images show blue nuclear marker (NLS-mTagBFP2) and green split-GFP complementation (GFP1-10 complemented with co-transfected Erk1-GFP11). Importantly cells without blue nuclear marker (depicted by arrows) show decreased/no fluorescence signal in the green channel. Images are scaled to the same intensity range to allow for direct comparison of relative intensity of fluorescence signal. Scale bar represents 20 µm.

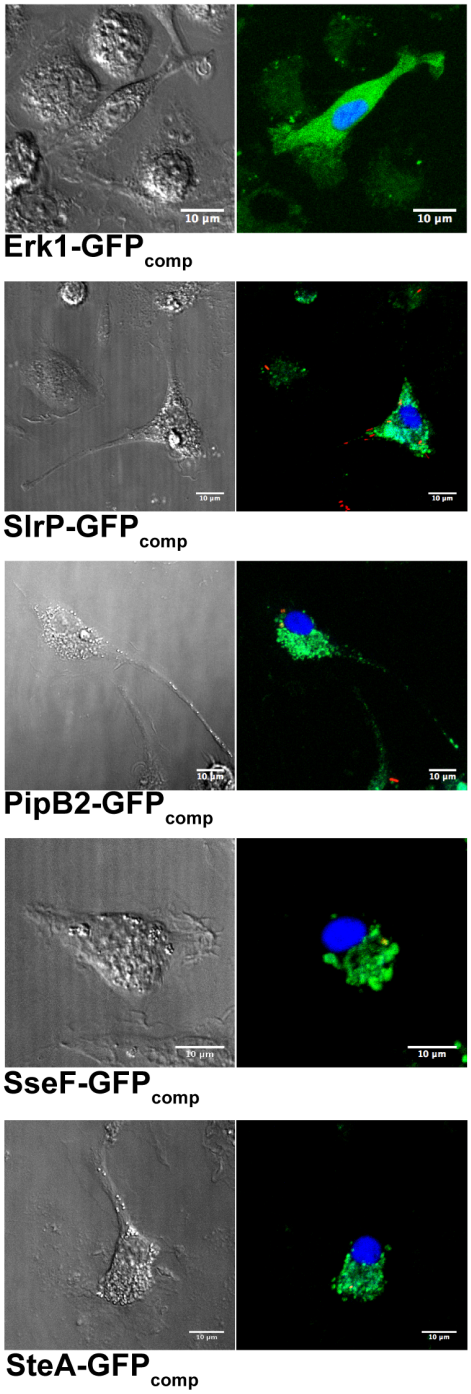

Figure 2.12 Fluorescence images demonstrating split-GFP fluorescence complementation in BMDMs nucleofected with GFP1-10-IRES-NLS-mTagBFP.
DIC (**left**) and fluorescence overlay (**right**; blue NLS-mTagBFP2, green GFP_{comp}, red *Salmonella* expressing mRuby3) images of BMDMs expressing GFP1-10-IRES-NLS-mTagBFP2. In the top row cells were co-transfected with ERK-GFP11 as a positive control. Remaining rows represent cells nucleofected with GFP1-10-IRES-NLS-mTagBFP2 and infected with *Salmonella* strains expressing mRuby3 and the specified effector tagged with GFP-11. Representative images collected from 12-14 hours post infection are shown. Scale bar represents 10 µm.

We successfully visualized SlrP, SteA, PipB2, SseG, and SseF in primary BMDMs (Figure 2.12). The SlrP-GFP$_{comp}$ signal appeared diffuse and cytosolic, indicating that localization in BMDMs is consistent with that observed in HeLa cells. The localization of SteA, PipB2, SseG, and SseF was consistent with localization to intracellular membranes and similar to the pattern observed for LAMP-1 (Figure 2.14), which is frequently used to mark the SCV.

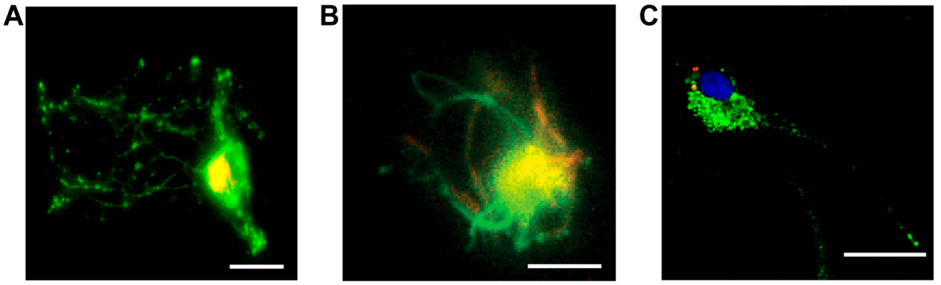

D

	Epithelial cell line	Macrophage cell line	Primary macrophage
Type of host cell:	HeLa cell	RAW264.7 cell	BMDM cell
Bacterial replication:	High replication	High replication	Limited replication
SCV phenotype:	Compact SCV	Compact SCV	Dispersed SCV
PipB2 localization:	PipB2 filaments	PipB2 filaments	No PipB2 filaments

Figure 2.13 *Salmonella* infection of different host cell types results in different intracellular niches.
Representative images of different types of host cells infected with Salmonella (red) displaying PipB2-GFPcomp fluorescence (green) are compared. An infected HeLa cell (**A**), a RAW264.7 cell (image modified from Van Engelenburg and Palmer)[17] (**B**), and a primary BMDM cell (**C**) are shown. The observed phenotypes for bacterial replication, SCV appearance, and PipB2 localization are detailed (**D**) for the different infected cell types. Scale bars are 20 µm.

Intriguingly, we observed distinct differences in the localization of these effector proteins compared to RAW264.7 cells, suggesting a significantly different intracellular niche in the macrophage cell line versus primary macrophage from immunocompetent mice (Figure 2.13). We previously found that SteA and PipB2 accumulated on the SCV and membrane tubules in both HeLa and RAW cells[17]. However, primary BMDMs often lack a compact SCV, and instead internalized bacteria are more commonly enclosed within a membrane-bound compartment but spread throughout the cell[171] (Figure 2.14), as was observed in infection of human monocyte-derived macrophages[74]. In the primary BMDMs used in this study, SteA, PipB2, SseG, and SseF generally co-localized with internalized bacteria, but

consistent with the lack of a concentrated SCV, effector localization was more spread out on intracellular membranes.

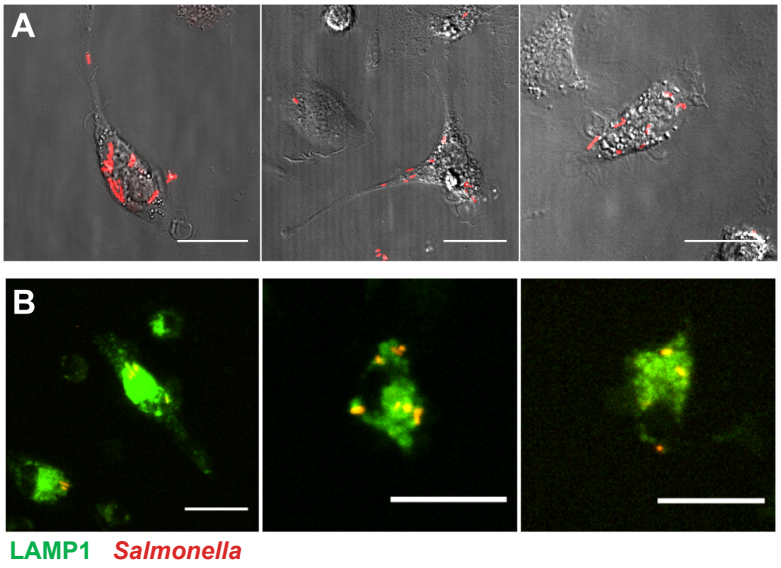

Figure 2.14 Images of infected primary BMDMs illustrating dispersed as opposed to compact bacteria.
(**A**) Overlay images showing primary BMDMs (DIC images) and bacteria (*Salmonella*, red). Images reveal that in primary BMDMs bacteria often don't cluster in a massive compact SCV but are more disperse. (**B**) Overlay of LAMP1-GFP (green) and bacteria (*Salmonella*, red) showing that in infected primary BMDM cells LAMP1 doesn't cluster in a massive SCV but is more disperse throughout cytosol. Scale bar represents 20 μm.

These results reveal different phenotypes, suggesting different niches, in different kinds of cells and demonstrate that the split-GFP effector protein labeling platform can be used in multiple cell types to study effector protein localization under different model infection conditions. Further, these results suggest that effector proteins may play different roles in different niches. The tools developed here open up the possibility of comparing localization, dynamics, and lifetime of effector proteins in different types of infected host cells to identify the different roles these effector proteins play in different infection models.

2.11 Development of SNAP-tag for Tagging Salmonella Effector Proteins

The split-GFP system has three main limitations that we sought to overcome by building a new tool for tagging effectors. First, it has limited time resolution for tracking effectors at early stages of

infection due to the time it takes for fluorophore maturation, ~2 hours. Second, it is a two component system that requires the expression the GFP1-10 in the infected host cell making application difficult in cells that are resistant to transient transfection or viral transduction. Third, it is not bright enough to visualize low abundance effectors. Self-ligating enzyme tags such as SNAP-tag allow for versatility in the types of chemical and fluorescent probes that can be attached to the tag[172]. This enables the use of fluorescent tags that are bright enough for single-molecule imaging[173] and the use of environment-sensitive fluorophores that permit no-wash imaging in live cells[174]. We set out to adapt a more robust tag for tracking effector proteins by investigating the use of the SNAP-tag labeling system in *Salmonella*. The 19.4 kDa SNAP-tag was engineered from human O6-alkylguanine-DNA alkyltransferase, a DNA repair enzyme[175]. The active site of the SNAP-tag contains a reactive cysteine that self-ligates to benzylguanine substrates. Several genetic fusions with effector proteins have been efficiently secreted through the T3SS, including the 28 kDa catalytic domain of CyaA[176], the SopE1-104SIV-Gag4-284 chimera[177], and various other short epitope tags, which all provide a precedent for the efficient secretion of other types of tags. Thus, we decided to test SNAP-tag as a possible substrate for T3SS in the context of a genetic fusion with a secreted effector protein.

I created a genetic fusion of the SNAP-tag to the SPI-2 effector PipB2 connected by a short flexible linker under the control of its endogenous promoter on the plasmid pACYC177. We chose PipB2 as a test case since it has been thoroughly characterized by ourselves and others. Effector proteins are known to be constitutively secreted into the culture medium under SPI-1 or SPI-2 inducing conditions. In order to test the secretion competence of PipB2-SNAP, I grew Salmonella expressing a plasmid containing the PipB2 effector fused to either SNAP-tag or 3XFLAG in SPI-2 inducing conditions (low magnesium, pH 5.4). I harvested protein from bacterial supernatants and bacterial lysates of strains of *Salmonella* expressing either PipB2-SNAP, PipB2-3XFLAG, or WT SL1344 with no tagged protein.

Secreted effector proteins were harvested by TCA precipitation of sterile filtered supernatant. Bacterial whole cell lysate of each induced strain was used as a positive control for expression. Secreted effector precipitates and whole cell lysates were prepared by heating in SDS loading dye and equal amounts of protein were run side by side with a purified SNAP-tag protein on an SDS PAGE gel

and then transferred to a PVDF membrane for antibody staining. Western blot analysis detected both PipB2-SNAP and PipB2-3XFLAG in the whole cell bacterial lysate, but only PipB2-3XFLAG was detectable in the supernatant (Figure 2.15).

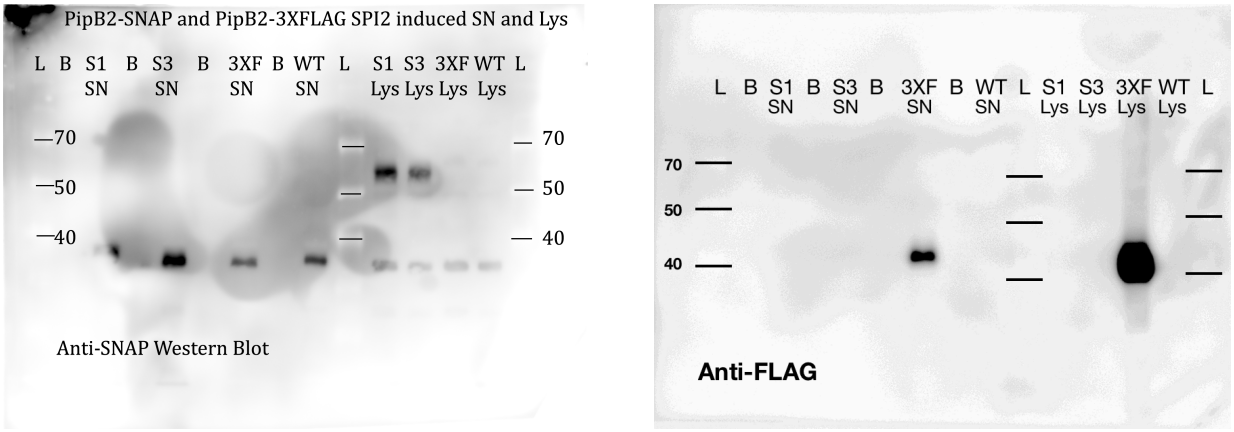

Figure 2.15 Western blot of PipB2-SNAP and PipB2-3XFLAG
Western blot of PipB2-SNAP and PipB2-3XFLAG isolated from the supernatant (SN) or bacterial cell lysate (Lys) from *Salmonella* cultured in SPI-2 inducing media. S1 and S3 are two clones of PipB2-SNAP. The lane in between each SN sample was left bank (B). WT Salmonella was used as a negative control to control for non-specific staining from the anti-SNAP antibody. Staining for the SNAP-tag (**Left**) shows the PipB2-SNAP fusion protein (~58 kDa) present in the lysate but not in the supernatant. Staining for FLAG (**Right**) show the PipB2-3XFLAG fusion protein (~41 kDa) present in both the lysate and the supernatant.

The ability of an effector protein fusion to be secreted from the T3SS has been linked to the thermodynamic stability of the fusion protein[7]. In the case of an effector-GFP fusion, the stability of the ß-barrel prevents the secretion of the protein due to its inability to be unfolded by the secretion machinery. SNAP-tag is also a thermodynamically stable protein[178]. The ΔG of unfolding for the SNAP-tag is higher than GFP as measured by single molecule force pulling[179]. Analysis of single molecule force pulling traces of a Titin-GFP-SNAP fusion revealed that both Titin and GFP unfold before SNAP-tag. If the SNAP-tag protein is more stable than GFP, then it is conceivable that the SNAP-tag would be unable to be unfolded by the T3SS, preventing efficient secretion of an effector protein fusion made with the SNAP-tag. The mechanism of single molecule force pulling is distinct from the way a protein is unfolded by the T3SS, however, because it does not account for the action of chaperones and ATPase action of the InvC protein within the export apparatus. Because the

mechanism of unfolding in the T3SS and the single molecule force spectroscopy are different, we decided to test whether the T3SS machinery would be able to unfold the SNAP-tag protein. We failed to detect the PipB2-SNAP-tag fusion protein in the supernatant of Salmonella grown in SPI-2 inducing culture media. We conclude that SNAP-tag is not secretion competent in the context of a fusion with PipB2 through the SPI-2 T3SS.

2.12 Discussion

In this work, we successfully demonstrated the use of the split-GFP protein for tagging and visualizing *Salmonella* secreted effector proteins in live infections in multiple cell types. We show that it is possible to track and quantify the spatial and temporal dynamics of effector proteins in individual host cells throughout the time course of the infection. Furthermore, we show for the first time that it is possible to track the effector localization and accumulation inside of primary macrophages from immunocompetent mice.

The development of innovative imaging approaches and fluorescence-based tools has enormous potential for defining the intracellular phenotypes of *Salmonella* infection at the single cell level. Because methods based on fixation and immuno-staining infected host cells are limited by the fact that the fate of intracellular bacteria, and the localization of effector proteins within the host cell cannot be followed over time throughout the course of infection, we have focused on developing approaches for live cell imaging. Current approaches developed by us and others have addressed the challenge that tagged effectors must be compatible with translocation through the narrow T3SS[17,46,47,180], and in this work, we further tackle the necessity for a versatile tool capable of illuminating effectors that are expressed at low levels. The modular platform for split-GFP labeling developed in this work enables the amplification of fluorescent signals by tuning effector protein expression level or by multimerizing the tag. Additionally, we generated a platform for expression of GFP1-10 along with a blue nuclear marker that serves to reveal GFP1-10 expressing host cells and aid in the verification of low complementation signals.

We find that effector localizations are different within primary macrophages from immune competent mice compared to a commonly used macrophage-like cell line suggesting that internalized

Salmonella can experience large differences in their host environment that may impact the function of individual effectors by disrupting their spatial and temporal localizations. Murine macrophages and macrophage-like cells have been widely used to study how *Salmonella* infects immune cells but few tools have been applied for live cell imaging. Previously, our lab developed methodology for quantifying *Salmonella* replication within primary BMDMs from immunocompetent mice (SV129S6), as a model for systemic infection[171]. SV129S6 mice contain a functional NRAMP1 metal transport protein and *Salmonella* can persist within macrophages of Nramp1$^{+/+}$ mice for up to 1 year, establishing this system as a model for chronic infection[65,75,181]. In our previous study we used a fluorescent marker constitutively expressed by *Salmonella* to track bacterial replication, and used genetic deletions to identify important roles for effectors in defining the replicative niche[171]. However, we did not previously visualize effector proteins within these cells due the challenges associated with genetically manipulating primary BMDMs. The immortalized macrophage-like cell line, RAW264.7, derived from immunocompromised NRAMP1$^{-/-}$ mice is easier to transfect and has often been used to investigate the role of effector proteins in macrophage infection. RAW264.7 cells differ significantly from primary BMDMs in their infection phenotype due to differences in proteomics and phagosome maturation[182] and in their susceptibility to infection and intracellular *Salmonella* replication dynmics[75,183,184]. RAW264.7 cells that lack a functional NRAMP-1 are unable to counteract the *Salmonella*-dependent mechanism that remodels the SCV and blocks fusion with vesicle traffic that contain bactericidal agents[183]. Macrophage-like cell lines have also been found to be unable to recapitulate the speed and magnitude of an antimicrobial response during early phase activation[185] and the surface receptor phenotype degrades with continuous culture[186]. Due to the differences in macrophage cell line infection model phenotypes we find the physiological relevance lacking.

With the use of nucleofector technology, transfection of primary macrophages is facile, making this more physiologically relevant infection model accessible for imaging of live cell infections. Importantly, because there are differences between RAW264.7 cells and immune competent BMDMs both in the phenotype of the SCV, compact VS dispersed, and in the localization of effectors, the need to understand how these differences impact effector functions increases. There are still questions

about effector proteins in immune competent macrophages in general. For example, which effector proteins are translocated, when they are present, and where they localize remains to be defined. The tools developed here open up the possibility of comparing localization, dynamics and lifetime of effector proteins in different types of infected host cells to help characterize these effector proteins in different infection models.

Chapter 3

Visualization of Translocated *Listeria* Effector Proteins in Live-Cell Infection Using a Multicolor Palette.

3.1 Abstract

Listeria monocytogenes is an intracellular food-borne pathogen that has evolved to enter mammalian host cells, survive within them, spread from cell to cell, and disseminate throughout the body. Translocated virulence proteins from *Listeria* are responsible for manipulation of host-cell defense mechanisms and adaptation to the intracellular lifestyle. Identifying when and where these virulence proteins are located in live cells over the course of *Listeria* infection can provide valuable information on the roles these proteins play in defining the host-pathogen interface. The dynamics and protein levels within host cells are heterogeneous both temporally and spatially. No assay to visualize *Listeria* or other Gram-positive bacteria virulence proteins during live-cell infection has been developed. We adapted a live, long-term fluorescence tagging system to visualize a model *Listeria* protein on a single-cell level in infection. We demonstrate accumulation and distribution within the host cell of the model virulence protein InlC in infection over time with red and green split-fluorescent proteins and compared usage of a strong constitutive promoter versus the endogenous promoter for InlC production. This split-fluorescent protein approach is versatile and may be used to investigate other Listeria virulence proteins for unique mechanistic insights in infection progression.

3.2 Publication Status and Author Contributions

Batan, D., Braselmann, E., Minson, M., Nguyen, D.M.T., Cossart, P., Palmer, A.E., "A Multicolor Split-Fluorescent Protein Approach to Visualize Listeria Protein Secretion in Infection" *Biophysical Journal,* 2018

D.B., E.B., A.E.P. designed research; D.B., E.B., M.M., D.M.T.N. performed research; D.B., E.B., M.M., D.M.T.N. analyzed data; P.C. contributed reagents and experimental advice; D.B., E.B., A.E.P. wrote the manuscript.

Portions of this chapter are reproduced from this manuscript.

3.3 Introduction

The facultative intracellular pathogen *Listeria monocytogenes* is the causative agent of the food-borne disease listeriosis and has emerged as a model system to study host-pathogen interactions on a cellular [25,187–190] and organismal level[191,192]. *Listeria* infection progression often displays heterogeneous phenotypes on a single-cell level, including intracellular replication patterns that vary from cell to cell both in space and time[193,194] and nonsynchronized spread from cell to cell[33]. Approaches to investigate single-cell infection dynamics, including fluorescence microscopy assays[195], can provide insights in *Listeria* infections that cannot be gathered by bulk assays. Live-cell fluorescence-tagging approaches of secreted proteins from *Listeria* or other Gram-positive pathogens have not been demonstrated. Therefore, we sought to test if the split-fluorescent protein system could be adapted to visualize secreted *Listeria* proteins of interest in the context of infection.

Internalin C (InlC) is a *Listeria* protein from the internalin family[196] that is secreted via the Sec pathway[28] and controlled by the PrfA transcriptional regulator[197]. In whole-animal mouse studies, virulence of an inlC deletion strain was significantly attenuated[196], but bacterial uptake and intracellular replication were not affected by deletion of InlC[198]. InlC's role in infection is underscored by the fact that inlC is absent in nonpathogenic *Listeria* strains and expression is high in infection conditions, namely in the intestine and blood[199]. Two functions of InlC have been described in the literature. Gouin et al. demonstrated that InlC interferes with the host innate immune response by

directly interacting with IKKα[200], whereas Rajabian et al. found that InlC promotes cell-to-cell spread by relieving membrane tension via interaction with the adaptor protein Tuba[198]. We chose InlC as an ideal test case to establish split-fluorescent protein tagging for the following reasons. First, InlC was produced with C-terminal fusions in various contexts, including tagging with a myc tag[200] and usage of an affinity tag for protein purification[201], indicating that a C-terminal tag is unlikely to interfere with protein production or function. Furthermore, the crystal structure of InlC is known[201], and manual inspection suggests that the InlC C-terminus is accessible and that a tag is unlikely to interfere with function (Fig. 5.1 c). GFP complementation in infection takes ~2 h[17,50] and is therefore ideal for robust visualization of virulence proteins at later infection time points. Indeed, several studies indicate high levels of InlC accumulation in infected epithelial cells at late infection stages (>4 h) both by Western blotting analysis[200] and immunofluorescence[200,202–204]. Lastly, the available immunofluorescence data in the literature[200,202–204] allow for assessment of InlC localization patterns by our split-fluorescent protein system. Together, visualizing secretion dynamics of tagged InlC in infection serves as a robust platform to establish the split-fluorescent protein tool in *Listeria*.

A series of inlC fusion constructs were generated to enable live-cell visualization of InlC in the context of infection of mammalian cells. We first fused the 11th strand of GFP with a flexible linker to the C-terminus of InlC analogous to a previous approach in which secreted effector proteins from the Gram-negative pathogen *Salmonella* were tagged with GFP11[17,50]. Production of the resulting nonfluorescent fusion protein was under control of the constitutive Phyper promoter on the multicopy plasmid pAT18[195] (Fig. 5.1 b). This initial construct allowed for maximal protein production in *Listeria* to assess the feasibility of split-GFP complementation in the context of *Listeria* infections.

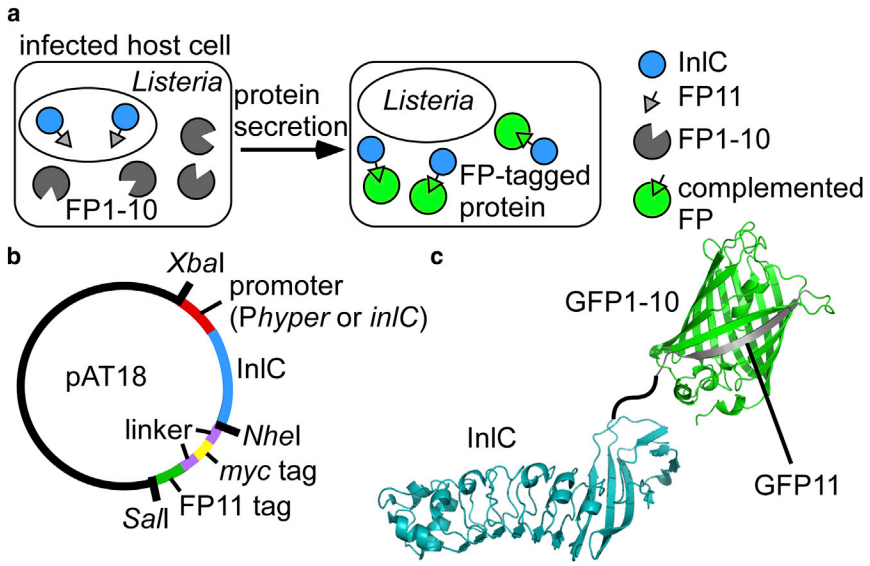

Figure 3.1 Overview of strategy for tagging *Listeria* virulence proteins with split-fluorescent proteins (FPs).
(**a**) An illustration of split-FP application in Listeria infection is shown. *Listeria* cells produce InlC with a C-terminal FP11 tag (the 11th strand of a fluorescent protein of interest, see Table 5.4 for sequence information of the tag). The host cell produces the remaining portion of the FP (FP1-10, see Table 5.5 for sequence information). After secretion of InlC-FP11, the two components of the FP complement, producing a fluorescent protein tag. (**b**) A plasmid overview for production of InlC-FP11 variants in *Listeria* is shown. In this study, two different promoters (Phyper and the endogenous inlC promoter) and three different FP11 tags were used (GFP11, mNeonGreen11, and super-folder Cherry11). The FP11 tag is fused to InlC via a flexible linker that includes a myc tag (see Table 5.4). (**c**) Structures of InlC[201] and GFP[205] illustrating C-terminal tagging of InlC via a flexible linker are shown.

3.4 Infectivity of *Listeria* Strains by CFU

Bacterial strains harboring plasmids sometimes exhibit decreased infectivity[146]. We compared bacterial load of the engineered strain Δ*inlC*$_{\text{Phyper-inlC-GFP11}}$ with the wt and ΔinlC strains at 7, 13, and 29 h post infection (Fig. 3.2). To measure bacterial load, a CFU assay was performed in which HeLa cells were infected with each strain and CFUs were quantified at each time point. At 7 and 13 h, there was a decrease in bacterial load for strains harboring plasmids with tagged InlC compared to the WT and ΔinlC strains, but the rate of growth of the plasmid bearing engineered strains between 13 and 24 h matched or exceeded the rate of growth for the WT and ΔinlC control strains. This observation is in line with a previous finding in which no difference in the infectivity of cultured cells was observed for

Listeria monocytogenes EGD ΔinlC versus its WT parent[200]. We concluded that infectivity in our cell infection assay is affected for our engineered strains but the intracellular replication behaves the same as the parent strains.

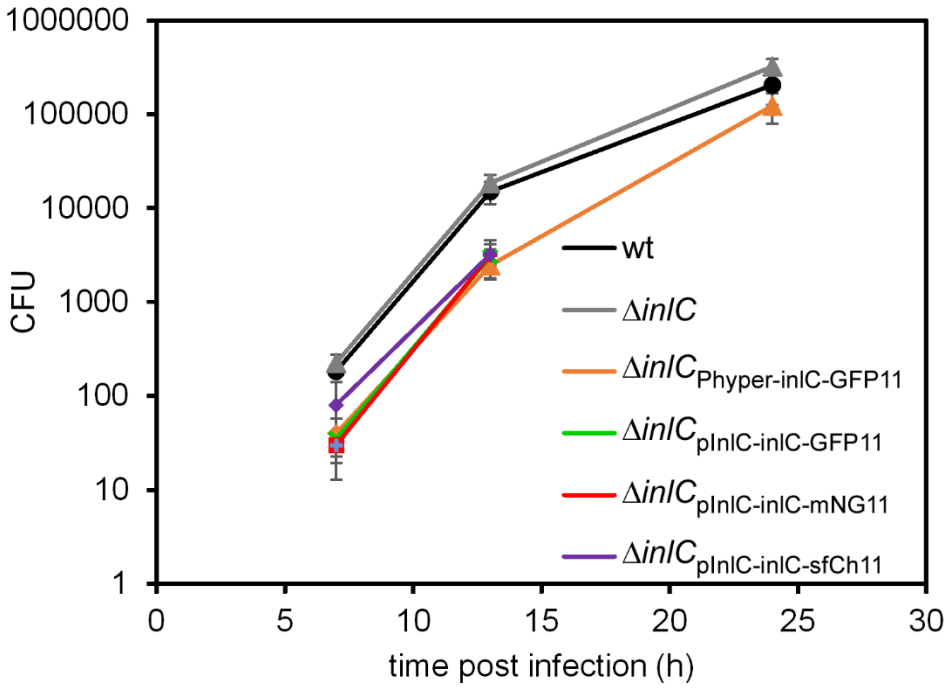

Figure 3.2 CFU analysis of HeLa cells infected for different lengths with the indicated strains (average from n=3 independent experiments, error bars indicate STD). 7 h time point: $p = 0.015$; 13 h time point: $p = 0.0035$, 24 h time point: $p = 0.0045$ (ANOVA test).

3.5 Visualizing *Listeria* Effector InlC-GFP in Fixed and Live Cell Imaging

Although secreted *Listeria* proteins including InlC have been routinely visualized in fixed infections by immunofluorescence[200,202–204], no tools have been applied to track virulence proteins in live infections. To determine whether the split-GFP system can be used to track secreted InlC, HeLa cells were transfected with DNA encoding for GFP1-10 before *Listeria* infection. The plasmid encoding GFP1-10 included a transfection marker producing nuclear TagBFP. Fig. 3.3 presents the results of cells that were transfected with GFP1-10 and infected with Δ*inl*C$_{\text{Phyper-inlC-GFP11}}$. *Listeria* infections were observed in the DIC channel via the distinct rod-like shape of the bacteria (Fig. 3.3 a, inset).

Green fluorescence signal was detected in HeLa cells infected with the Δ*inlC*$_{Phyper\text{-}inlC\text{-}GFP11}$ strain but not for an uninfected control (Fig. 3.3 a).

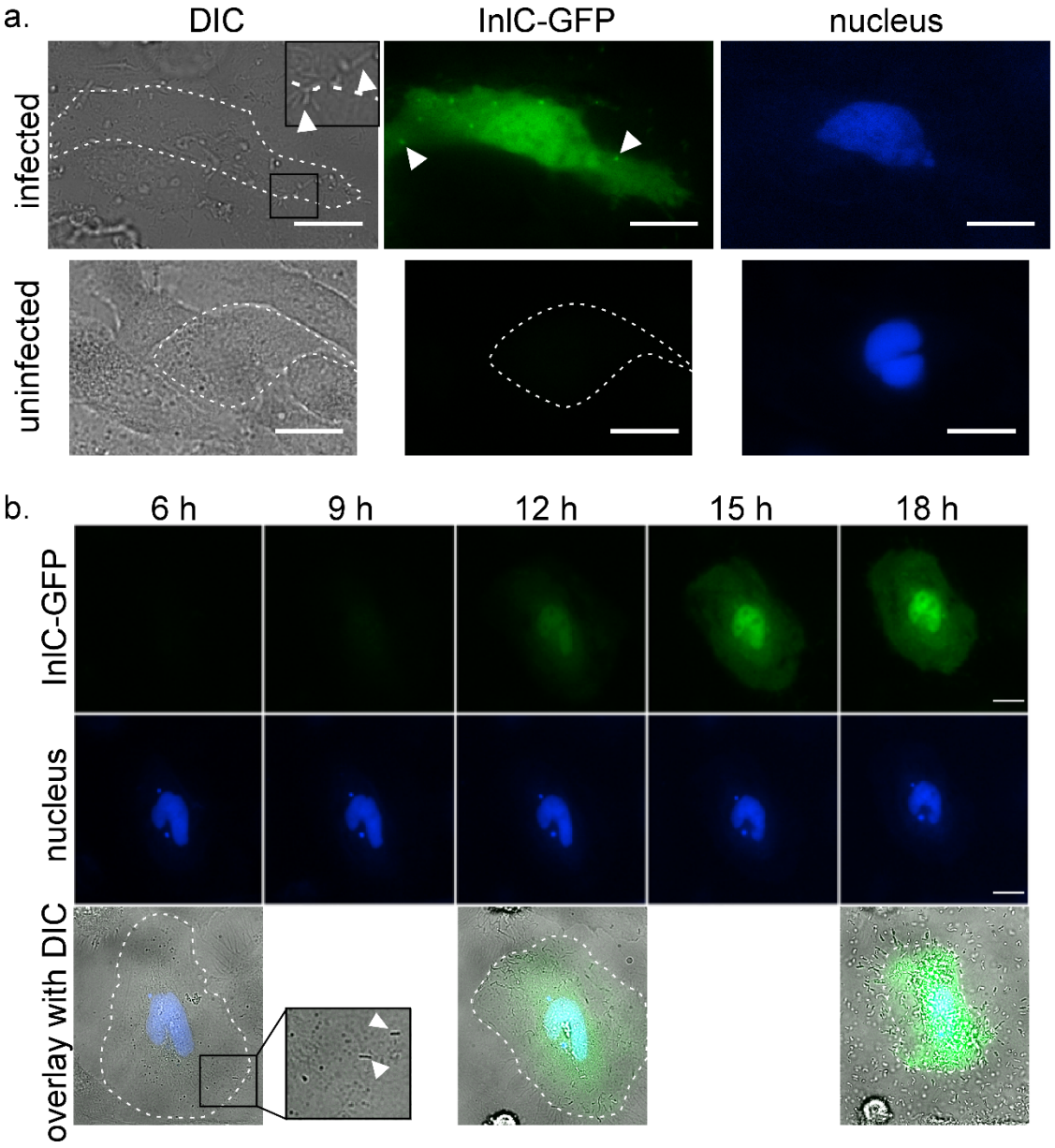

Figure 3.3 Split-GFP tagging of InlC during infection of epithelial cells**.**
(**a**) Microscopy images of HeLa cells producing GFP1-10 (see Table 5.5 for sequence information) and a nuclear TagBFP transfection marker. Shown are cells infected with Δ*inlC*$_{Phyper\text{-}InlC\text{-}GFP11}$ (see Table 5.4 for tag sequence information) at 18 hours post infection (top panel, 2 experiments, 15 cells) and an uninfected control (bottom panel). Inserts in DIC channel: example of *Listeria*. Arrows in green channel: example of InlC cell membrane puncta. (**b**) Microscopy images of live HeLa at different time points post infection with Δ*inlC*$_{Phyper\text{-}InlC\text{-}GFP11}$. *Listeria* entered the cell shown here at 6 h post infection (see arrows in DIC insert) and accumulate within the host cell throughout the time course. Cells were transfected to produce GFP1-10 and a nuclear transfection marker. Scale bar = 20 µm.

These results confirm complementation of GFP1-10 and GFP11 upon InlC-GFP11 secretion during *Listeria* infection. We observed diffuse cytosolic signal of the complemented InlC-GFP (Fig. 3.3 a), in line with cytosolic InlC signal detected by immunofluorescence by us (Fig. 3.4) and others[200,202,204]. Interestingly, studies in the literature also report localization of InlC at cell protrusions that form during *Listeria* cell-to-cell spread[202]. We observed similar protrusions that appear as brighter green puncta in live cells (Fig. 3.3 a, arrow) and occasionally in fixed immunofluorescence images (Fig. 3.5, arrow). The complemented GFP fluorescence could be preserved upon fixation, and the pattern of localization generally matched the fluorescence signal from anti-InlC immunofluorescence (Fig. 3.6). When InlC puncta were visible in IF images (via GFP comp or anti-InlC), they were juxtaposed with *Listeria* (detected via DIC) and actin bundles (detected via phalloidin), consistent with the suggestion that InlC may promote cell-to-cell spreading (Fig. 3.6). Together, we conclude that our split-GFP tagging system reports on InlC localization and resembles localization patterns of endogenous InlC.

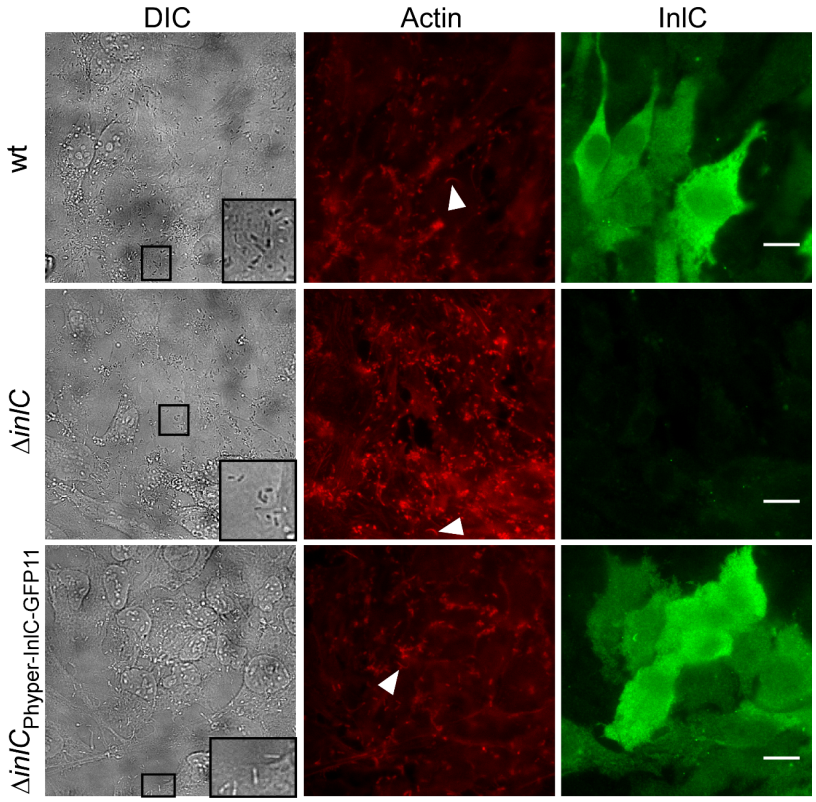

Figure 3.4 Tagged InlC is produced and secreted into the HeLa host cell in the context of *Listeria* infection.
HeLa cells were infected with the indicated strains and cells were fixed 25 h post infection. Actin was detected via Alexa 594-phalloidin and InlC was detected by immunofluorescence using a polyclonal anti-InlC antibody[204] and a Alexa Fluor 488 labeled secondary antibody. Representative *Listeria* cells are indicated in the inserts in the DIC channel and actin tails are indicated by arrows in the red channel. Images are presented at the same intensity levels for each channel. Scale bar = 20 µm (wt infection: n=36 infected cells total; Δ*inlC*: n=29 infected cells total; Δ*inlC*$_{\text{Phyper-InlC-GFP11}}$: n=63 infected cells total).

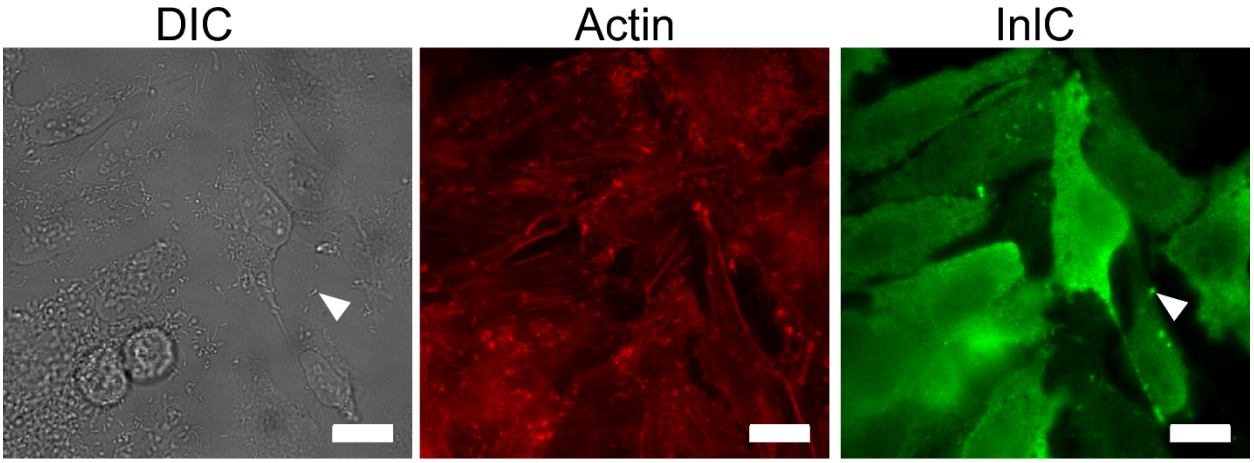

Figure 3.5 InlC occasionally localizes to cell protrusions from Listeria
InlC occasionally localizes to puncta consistent with cell protrusions from *Listeria* spreading from cell to cell (white arrow). Shown is a select region of interest for infection of HeLa cells with Δ*inlC*$_{\text{Phyper-InlC-GFP11}}$ (see Fig. 3.4 for details). Scale bar = 20 µm.

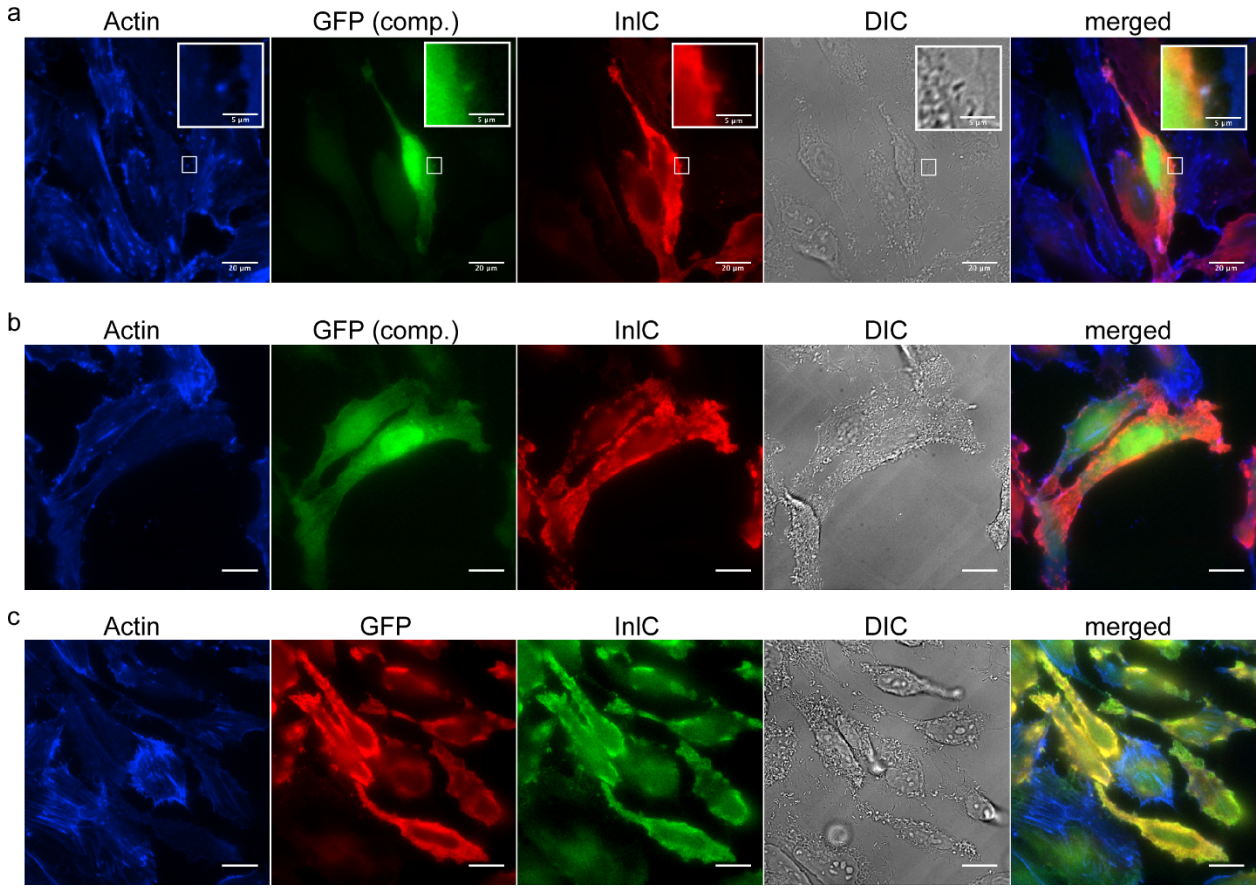

Figure 3.6 GFP signal after complementation colocalizes with fluorescence signal from anti-InlC immunofluorescence.
(**a, b**) HeLa cells producing GFP1-10 were infected with Δ*inlC*$_{\text{pInlC-inlC-GFP11}}$ overnight and cells were fixed. After permeabilization, actin was stained with Phalloidin-coumarin and InlC was detected by immunofluorescence. The overall pattern and the insert in (a) demonstrate colocalization of complemented GFP signal and InlC. Note that the InlC signal in the nucleus appears brighter when detected by complemented GFP vs. anti-InlC immunofluorescence. This could be due to incomplete permeabilization of the nuclear envelope, which may limit the accessibility of anti-InlC antibodies. Panels (**a**) and (**b**) show representative fields of view. (**c**) HeLa cells were infected with Δ*inlC*$_{\text{pInlC-inlC-GFP11}}$ overnight and cells were fixed. After permeabilization, actin was stained with Phalloidin-coumarin and InlC as well as GFP was detected by immunofluorescence. Scale bar = 20 µm (scale bar for insert in panel (a) = 5 µm).

3.6 Measuring *Listeria* Effector Protein Dynamics in Live Cells

Because the split-GFP system enables time-resolved visualization of tagged protein dynamics, we monitored GFP fluorescence for several hours during infection of epithelial cells (Fig. 3.3 b). HeLa cells were transfected with GFP1-10 including the nuclear TagBFP transfection marker and infected with the strain Δ*inl*C$_{\text{Phyper-inlC-GFP11}}$. Because *Listeria* infections are heterogeneous both in space and time, it is often difficult to track infection progression in a bulk assay. The time course presented in Fig. 3.3 b shows *Listeria* that enter a single HeLa cell at 6 h post infection (see DIC inset in Fig. 3.3 b), precisely indicating the infection starting point. We monitored the GFP channel for 12 h past this time point and observed an increase of the green fluorescence signal in the cytosol and nucleus, in line with intracellular accumulation of InlC. As seen with western blot assays in the literature[200], high levels of InlC accumulated late in the infection process, leading us to conclude that our split-GFP approach is suitable for spatiotemporal resolution of secreted proteins in infection.

We next assessed InlC-visualization in live infections when the InlC-GFP11 fusion was produced from the endogenous *inlC* promoter to closer mimic the WT *Listeria* strain. For a direct comparison between the *inlC* and P*hyper* promoters, we infected HeLa cells transfected with GFP1-10 (Table S4) with strains Δ*inlC*$_{\text{Phyper-inlC-GFP11}}$ and Δ*inlC*$_{\text{pInlC-inlC-GFP11}}$ side by side for 24 h (Fig. 3.7, see Table 5.3 and 5.4 for sequence information of the promoters and tags). As seen before with Δ*inlC*$_{\text{Phyper-inlC-GFP11}}$ (Fig. 3.3), we observed diffuse cytosolic signal in the GFP channel for both strains (Fig. 3.7a), confirming successful complementation of GFP1-10 with InlC-GFP11. No GFP fluorescence was seen for infected cells that were not transfected with GFP1-10, confirmed by the absence of the nuclear TagBFP marker (Fig. 3.7a, stars in DIC images). As before (Fig. 3.3a), we observed bright green puncta in the GFP channel in addition to cytosolic GFP fluorescence (Fig. 3.7a, arrows in GFP channel). These likely represent protrusions from *Listeria* during cell to cell spread, as observed by others[202] and by us in immunofluorescence images (Fig. 3.5 arrow, Fig. 3.6 insert). Occasionally, we also observed elongated protrusions in the xy plane in the GFP channel (Fig. 3.7a, contrast enhanced insert). We concluded that these structures also represent membrane protrusions while *Listeria* spreads from cell to cell. To directly confirm that the GFP signal after complementation corresponds to signal from InlC, we

repeated the complementation experiment with Δ*inlC*$_{\text{pInlC-inlC-GFP11}}$, fixed cells, and performed immunofluorescence against InlC (Fig. 3.6, a and b). Both the overall fluorescence pattern, as well as protrusions at the cell membrane (Fig. 3.6 a), overlapped for the signal from complemented GFP and InlC. Overall, usage of the endogenous inlC promoter and the Phyper promoter resulted in comparable phenotypic GFP complementation patterns.

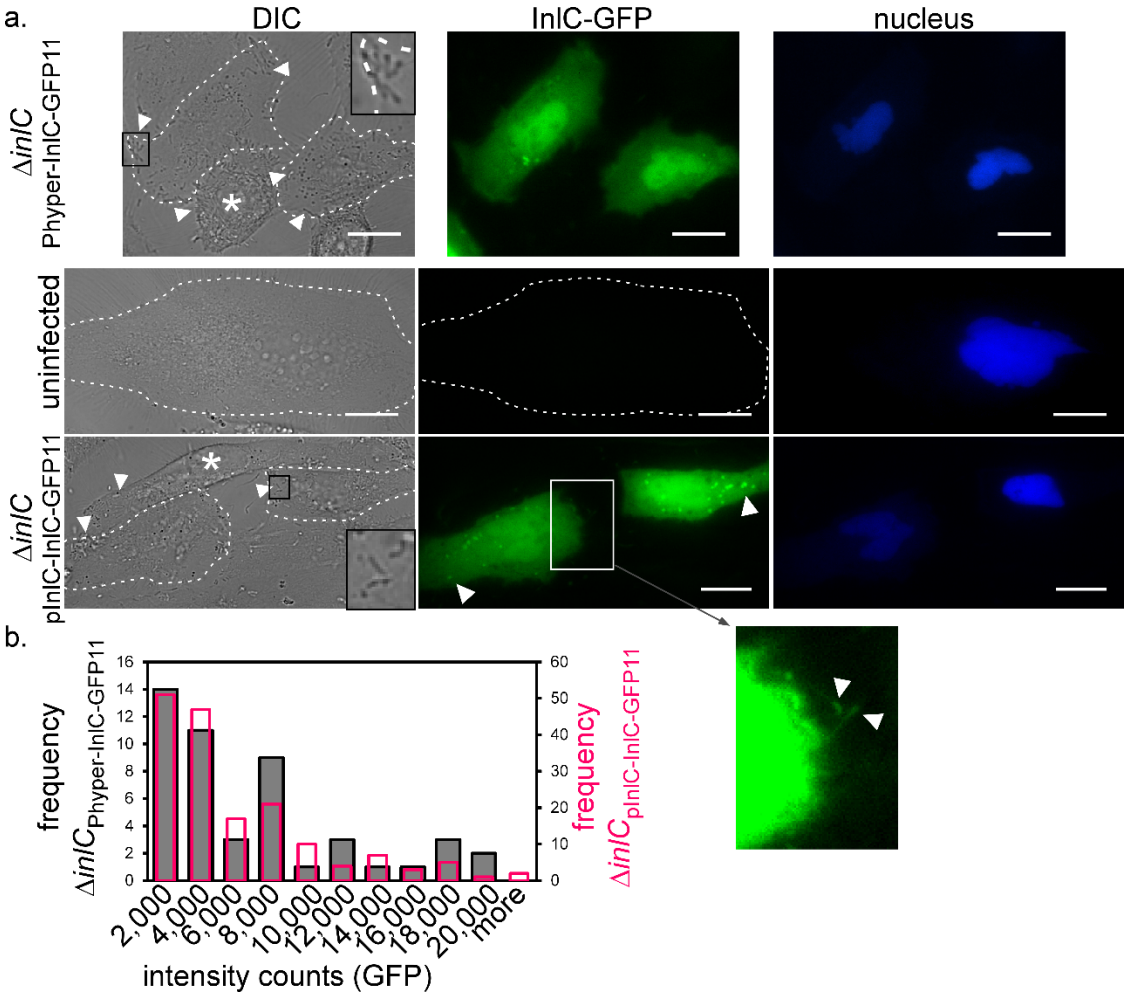

Figure 3.7 Visualization of complemented InlC-GFP under control of different promoters. (**a**) HeLa cells were transfected with a plasmid to produce GFP1-10 (Table 5.5) and a nuclear TagBFP transfection marker and infected with indicated *Listeria* strains (see sequence information in Tables 5.3 and 5.4) for 24 h. Images in the GFP channel are presented at the same intensity levels. Arrows and inserts in the DIC channel indicate *Listeria* cells. Stars in the DIC channel indicate cells that were infected but not transfected (confirmed by absence of the nuclear TagBFP marker). Arrows in the InlC-GFP channel for Δ*inlC*$_{\text{pInlC-InlC-GFP11}}$ indicate InlC membrane protrusions (as in Figure 3.3a). Scale bar = 20 µm. Insert for Δ*inlC*$_{\text{pInlC-InlC-GFP11}}$: Contrast-enhanced image indicating elongated membrane protrusions. (**b**) The mean intensity in the GFP channel was quantified for individual cells 24 h post infection using identical acquisition settings (grey filled bars: Δ*inlC*$_{\text{Phyper-InlC-GFP11}}$, 3 independent experiments, 48 cells; pink open bars: Δ*inlC*$_{\text{pInlC-InlC-GFP11}}$, 2 independent experiments, 168 cells).

For a quantitative comparison of the *inlC* and P*hyper* promoters, we compared the mean cytosolic fluorescence signal in each infected cell for Δ*inlC*$_{\text{Phyper-inlC-GFP11}}$ and Δ*inlC*$_{\text{pInlC-inlC-GFP11}}$ at 24 h post infection (Fig. 3.7b). The mean fluorescence intensity for both strains was comparable (average fluorescence intensity in arbitrary units of 5,878 counts for Δ*inlC*$_{\text{Phyper-inlC-GFP11}}$ vs. 5,031 counts for Δ*inlC*$_{\text{pInlC-inlC-GFP11}}$). Median counts were 3,411 vs. 3,239, respectively. Similarly, while the distribution of intensities between cells was heterogeneous and spanned an order of magnitude for both strains, no difference in intensity distribution was apparent (Fig. 3.7b). For an additional robust comparison of the InlC and P*hyper* promoters, we infected HeLa cells with the Δ*inlC*$_{\text{Phyper-inlC-GFP11}}$ vs. Δ*inlC*$_{\text{pInlC-inlC-GFP11}}$ strain and visualized infection and GFP complementation on a high content analysis (HCA) microscope (Fig. 3.8). This experimental setup allowed for parallel imaging of both infections at the same time. The HeLa cell line stably produced GFP1-10 (Table 5.5) and the nuclear TagBFP marker[50]. We quantified GFP fluorescence at two time points during the time course, 3 h post infection vs. 6.5 h post infection. As expected, fluorescence counts increased over time for both strains (Fig. 3.8c). However, no statistically significant difference in GFP intensity was observed when comparing the two strains at each time point. While the P*hyper* promoter is strong and induces constitutive protein expression[195], the *inlC* promoter is only active in infection for high level InlC production[195,199]. This indicates that both promoter strengths produce comparable translocated InlC levels in our experimental conditions (Fig. 3.7, Fig. 3.8). We concluded that the P*hyper* promoter may serve as a robust promoter for split-GFP tagging of secreted proteins from *Listeria*, and that the system is compatible with using endogenous promoters as well.

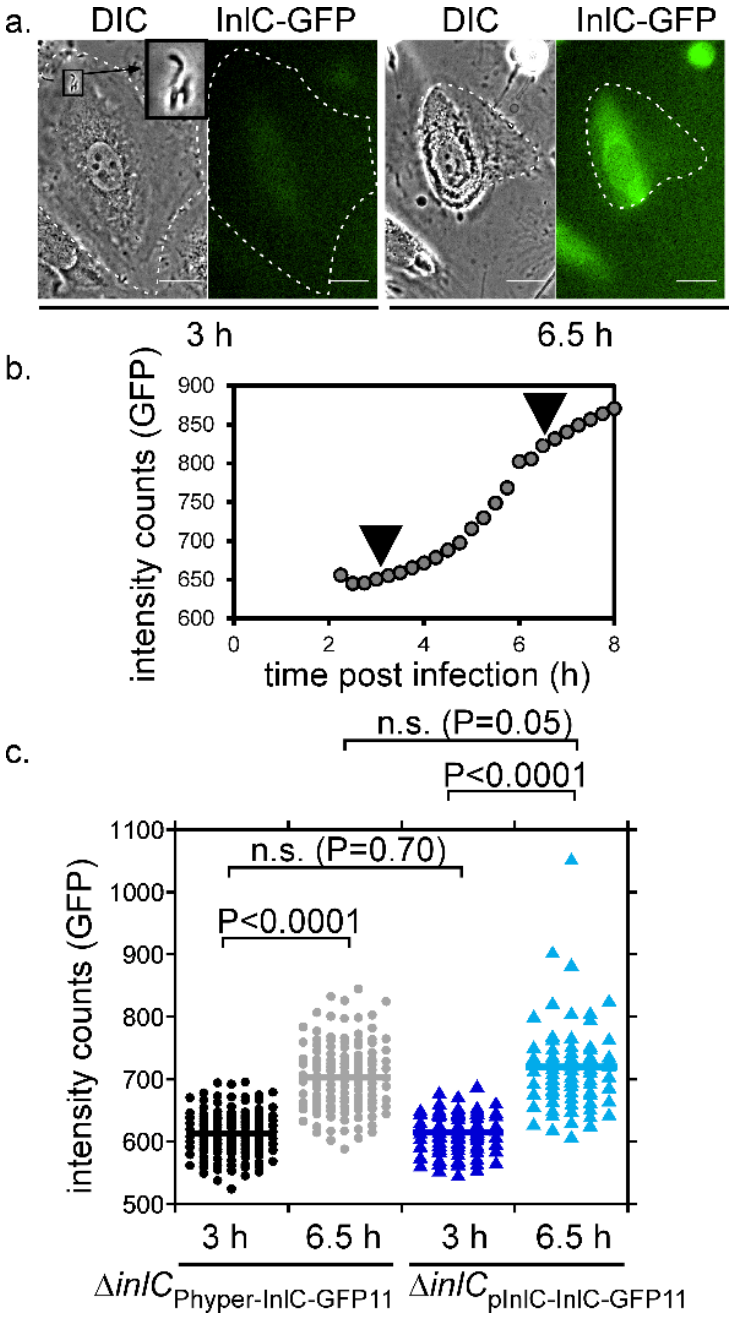

Figure 3.8 High throughout quantification of GFP complementation during *Listeria* infection.

(**a**) HeLa cells were infected with Δ*inlC*$_{\text{Phyper-InlC-GFP11}}$ and Δ*inlC*$_{\text{pInlC-InlC-GFP11}}$ side by side and infections were visualized over time in parallel in the same experimental setup. A representative infection (Δ*inlC*$_{\text{pInlC-InlC-GFP11}}$) at 3 h post infection (left panel) vs. 6.5 h post infection (right panel) is shown. Insert indicates examples of *Listeria* cells in the DIC channel. Scale bar = 20 µm. Images in the GFP channel are presented at the same intensity levels. (**b**) Quantification of GFP fluorescence intensity for the time course shown in (a). Arrows indicate 3 h and 6.5 h post infection. (**c**) The mean GFP fluorescence signal for all cells in the experiment was determined at 3 h post infection vs. 6.5 h post infection (one experiment; n=128 cells for Δ*inlC*$_{\text{Phyper-InlC-GFP11}}$ and n=75 cells for Δ*inlC*$_{\text{pInlC-InlC-GFP11}}$). Statistical significance was determined using a Tukey HSD ANOVA test.

3.7 Visualizing InlC-GFP$_{Comp}$ in BMDMs

In addition to infecting epithelial cells, *Listeria* also infects macrophages. To assess whether the split-GFP system could also be used to monitor *Listeria* effectors, we transfected BMDMs with GFP1-10 and the nuclear TagBFP and infected them with Δ*inlC*$_{pInlC\text{-}inlC\text{-}GFP11}$. Cells containing GFP1-10 are readily identified via blue nuclear marker expressed from an internal ribosome entry site from the GFP1-10 plasmid. As observed for *Salmonella*, the fluorescence complementation signal is weaker than in HeLa cells, but is significantly above the background fluorescence (Fig. 3.9). Because BMDMs in culture are phagocytic, InlC localization is not strictly cytosolic, and the protein seems to accumulate in phagosome and early lysosomes. This system can be used to track Listeria effectors in this physiologically relevant model system.

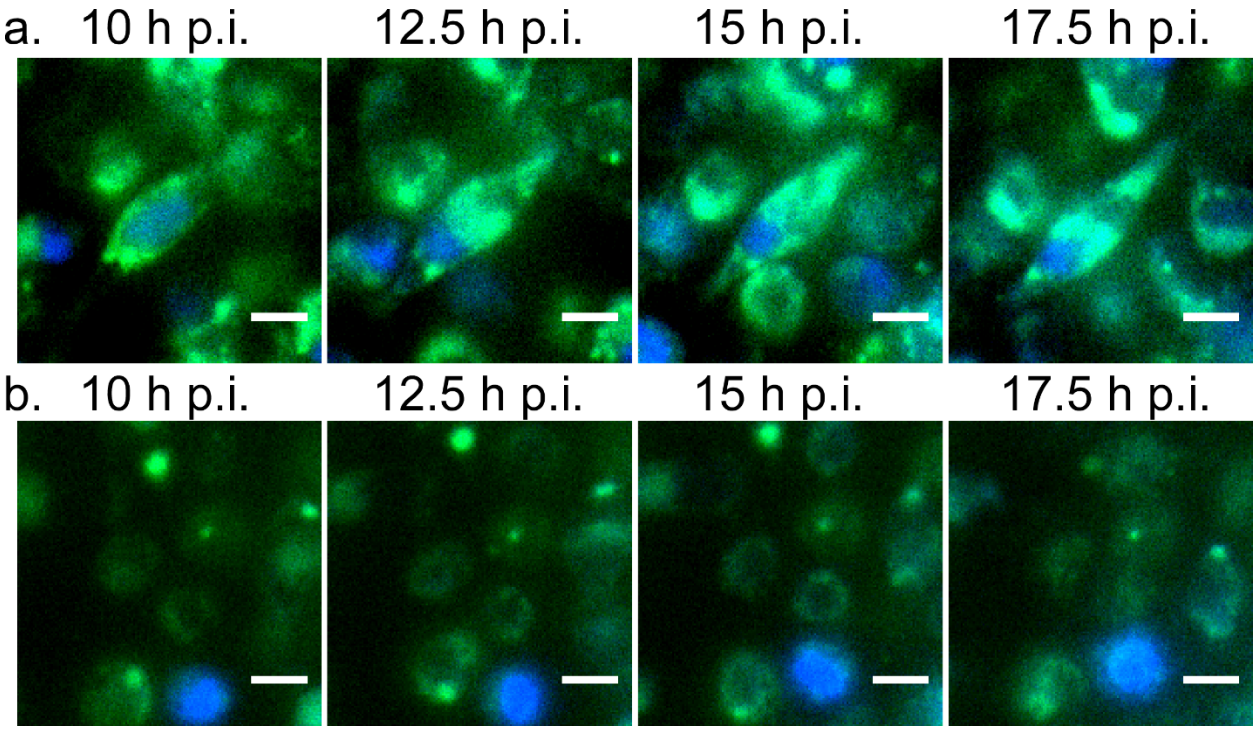

Figure 3.9 BMDMs expressing GFP1-10 and the nuclear TagBFP infected with Δ*inlC*$_{pInlC\text{-}InlC\text{-}GFP11}$.
GFP complementation signal increases over the course of infection for infected cells (**a**) but not for uninfected cells (**b**). The fluorescence signal was adjusted to have the same thresholds for panel (**a**) and (**b**). GFP complementation may accumulate in non-transfected cells as macrophages consume other transfected and infected cells. Scale bar = 20 µm.

3.8 New Split Fluorescent Proteins for Monitoring Effector Translocation

Although split-GFP tagging for secreted bacterial proteins in infection has been used previously in *Salmonella* infections[17,50], usage of split-fluorescent proteins of different colors would allow for broad flexibility in multicolor fluorescent imaging assays. Our *Listeria* expression plasmid is modular, and the split-fluorescent protein tag can be exchanged easily (Fig. 3.1 b). Guided by the recent optimization of split mNeonGreen and split super-folder Cherry [53,206], we exchanged the GFP11 tag with the 11th strand of mNeonGreen (called here mNG11, derived from mNG2 in [53]) and the 11th strand of super-folder Cherry (called here sfCh11, derived from sfCherry2 in [53], see Table 5.4 for sequence information of mNG11 and sfCh11). Both InlC fusions were produced under control of the inlC promoter (Table 5.3). We transfected HeLa cells with sfCh1-10, encoding for the non-fluorescent strands 1–10 of super-folder Cherry (see Table 5.5 for sequence information), followed by infection with $\Delta inlC_{\text{pInlC-inlC-sfCh11}}$ for 24 h. As expected for a 24 h infection, all HeLa cells in the field of view presented in Fig. 3.10a were infected with *Listeria* (Fig. 3.10a, inset and arrows in DIC channel). We observed fluorescence above background in the red fluorescent channel for some cells, consistent with complementation of sfCh11 and sfCh1-10. Some infected cells were nonfluorescent, in line with the assumption that not all cells were transfected with sfCh1-10 (Fig. 3.10a, stars in DIC channel indicate infected cells without red fluorescence). Note that sfCh1-10 and mNG1-10 do not include a transfection marker as does GFP1-10. As seen for split-GFP (Figs. 3.3), the red fluorescence signal was diffusely distributed throughout the cytosol, and we also observed fluorescent puncta (Fig. 3.10a, arrow in InlC-sfCh channel) that resemble cell protrusions found during *Listeria* cell-to-cell spread.

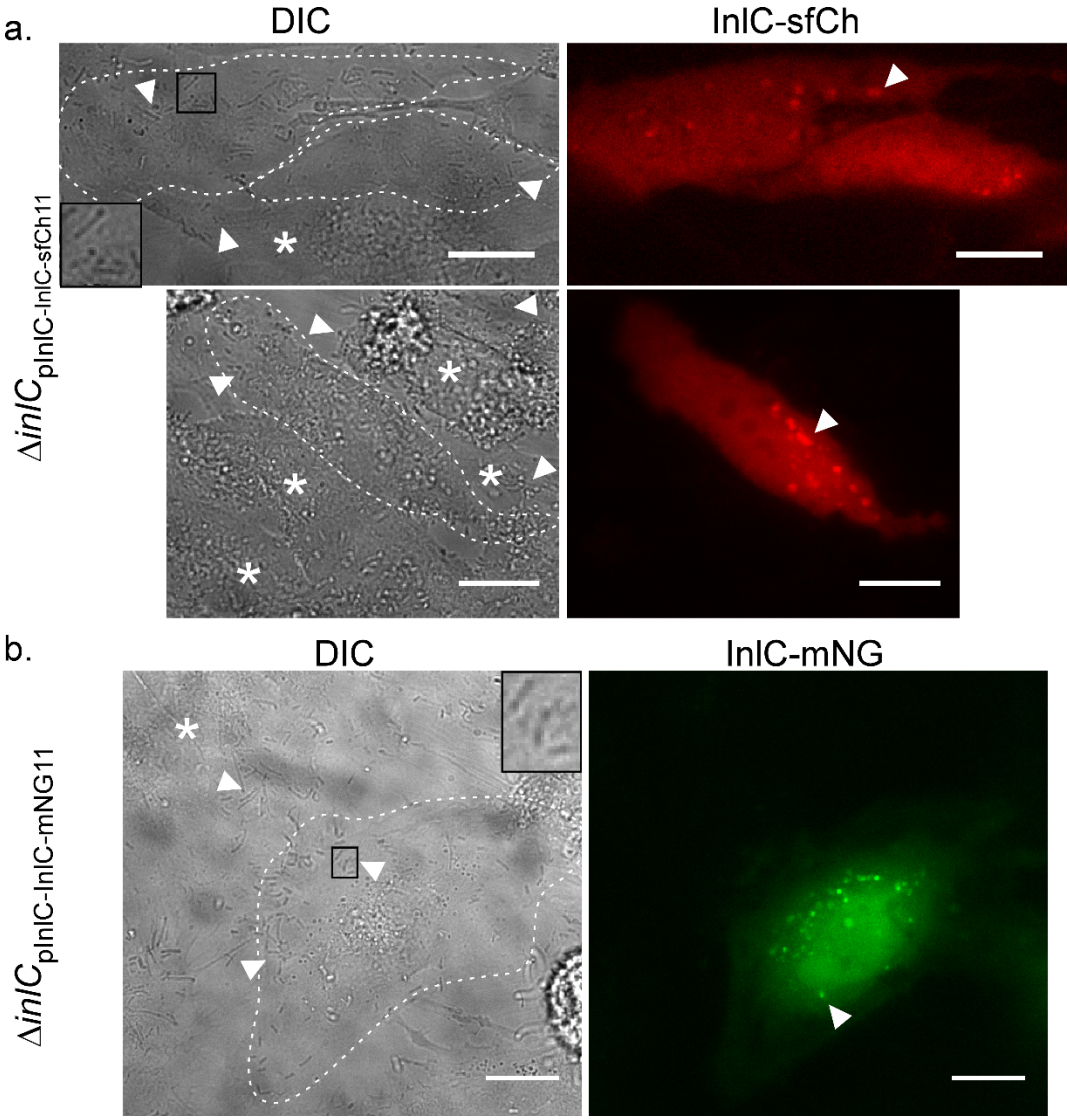

Figure 3.10 Visualization of InlC via super-folder Cherry and mNeonGreen complementation in infection.
(**a**) HeLa cells were transfected with sfCh1-10 (see Table 5.5 for sequence information) and infected with Δ*inlC*$_{\text{pInlC-InlC-sfCh11}}$ (see Table 5.3, 5.4 for promoter and tag sequence information) for 24 h. Shown are two representative fields of view with sfCh signal above background. Raw fluorescence counts above background are variable (upper panel: ~2,000 cytosolic counts, lower panel: ~8,000 cytosolic counts). Stars: Infected cells that display background sfCh counts and were presumably not transfected with sfCh1-10 (typical background counts: <1,000). Arrows and insert in DIC channel point to *Listeria*. Arrows in the InlC-sfCh channel indicate InlC cell protrusions as in Figure 3.3 and 5. Scale bar = 20 µm (2 experiments, 10 cells). (**b**) HeLa cells were transfected with the non-fluorescent mNG1-10 (see Table S4 for sequence information) and infected with Δ*inlC*$_{\text{pInlC-InlC-mNG11}}$(see Table 5.3, 5.4 for promoter and tag information) for 24 h. Arrows and insert in the DIC channel indicate *Listeria* cells and the star in the DIC channel indicates a HeLa cell that is infected but displays background green fluorescence signal. The arrow in the InlC-mNG channel indicates bright puncta presumably corresponding to cell protrusions during *Listeria* cell-to-cell spread. Scale bar = 20 µm (2 experiments, 16 cells).

To assess complementation of mNeonGreen, HeLa cells were transfected with DNA encoding for the nonfluorescent mNG1-10 and infected with Δ*inlC*$_{pInlC\text{-}inlC\text{-}mNG11}$ for 24 h. As for GFP and super-folder Cherry complementation, we readily observed infected HeLa cells displaying bright green fluorescence throughout the cytosol, indicating successful complementation (Fig. 3.10b). We also observed bright puncta (Fig. 3.10 b, arrow in InlC-mNG channel) as observed for GFP and super-folder Cherry complementation, resembling cell protrusions during Listeria spread. Together, we concluded that tagging secreted *Listeria* proteins with split-fluorescent proteins is highly modular and compatible with proteins of different fluorescent colors, including GFP, mNeonGreen, and super-folder Cherry.

3.9 Discussion

Visualization of virulence proteins in bacterial infections on a single-cell level is a powerful tool to gain insights into the spatiotemporal dynamics of the complex infection process. Here we demonstrated a proof of principle application of tagging the secreted protein InlC from *Listeria* in epithelial cells and primary macrophages. InlC localization and accumulation throughout the infection can be readily quantified, while also capturing the heterogeneity of the infection between different cells. We envision that split-fluorescent protein tagging of secreted proteins can be widely applicable in diverse biological contexts. Our previous work on labeling secreted effector proteins from *Salmonella*[17,50] was limited to tagging proteins secreted by the type III secretion mechanism, a specialized secretion pathway for virulence proteins in Gram-negative bacteria[207]. The application in *Listeria* secretion demonstrates compatibility with the Sec secretion pathway, a general and ubiquitous secretion pathway in all bacteria with more than one third of the bacterial proteome as clients[208]. Besides in-depth investigations of diverse bacterial infections in different mammalian cell systems, dynamic visualization of secreted proteins may be used for various other applications including biofilm formation, labeling of cell wall or membrane proteins, or synthetic biology systems. Lastly, the evolutionary similarity between the bacterial Sec secretion system and mammalian secretion systems in organelles[209] suggests that the split-fluorescent technology may be used to investigate mammalian secretion systems as well.

We demonstrated that two new split fluorescent proteins, mNeonGreen 1-10/11 and super-folder Cherry 1-10/11 are both capable of tagging effector proteins, increasing the palette of colors available for studying the dynamics of effector proteins throughout the cycle of infection. The establishment of these new brighter split fluorescent proteins provides exciting possibilities for dual labeling of effector proteins. Effector proteins often interact with one another and can drive the localization of one another as is the case with SseF and SseG in *Salmonella*, two effector proteins that physically and functionally interact to coordinate the localization and maintenance of the SCV[151,154–156]. Tagging SseF and SseG with mNG11 and sfCh11 and imaging the two simultaneously in a live cell would be a great way to measure the extent of interaction and colocalization of these two proteins, and also the specific lifetimes and accumulation dynamics. Visualization of other membrane bound *Salmonella* effectors that contribute to the maintenance and stability of *Salmonella* induced filaments such as SteA, PipB2, and SifA would also greatly add to the understanding of the process of SIF formation and dynamics. The timing and colocalization of each of these proteins would be useful to measure because the timing of secretion may be different given that some of these effectors are substrates of both SPI-1 and SPI-2 secretion systems[16,210]. Another example of the type of scientific study that could be enabled by the tools developed in this chapter is dual-color labeling of individual effector proteins. Many effector proteins are modular, made up of two separate domains separated by a caspase cleavage motif that are processed inside the host cell and have distinct localization patterns and functions[23]. Dual labeling of the separate domains of an effector protein and tracking the processing and destination of these individual domains would be a significant improvement on current methods for determining their localization, and would reveal finer resolution for defining time dependent events and interaction partners.

There are a number of important considerations for using split-fluorescent protein systems. Tagging a protein of interest with the 11th strand of a fluorescent protein is limited to situations where the tag is accessible to bind with and complement the remaining 1-10 fragment. Terminal tagging at the C-terminus is ideal to avoid interfering with an N-terminal signal sequence. Depending on each protein's function, C-terminal tagging may interfere with its function, and each protein of interest

must be evaluated for this potential problem, a general caveat of fluorescent protein tagging[211]. We produced tagged InlC from a high-copy plasmid, resulting in overexpression of the fusion. Although our proof of principle live InlC imaging produced results consistent with literature results on fixed cells, subtler biologically relevant phenotypes may be extracted when the tagged virulence protein is integrated in the genome. Complementation of GFP in the context of infection takes at least 2 h[17], limiting the time resolution of detection for early secretion events. mNeonGreen 1-10/11 and super-folder Cherry 1-10/11 are based on faster folding variants of fluorescent proteins, and mNeonGreen 1-10/11 is brighter than GFP1-10/11, thus they may be able to be visualized earlier in infection and may require less accumulation of the complemented protein before visualization can be achieved. The improved brightness of mNeonGreen 1-10/11 may also enable visualization of low-abundance effector proteins or visualization in cell types where the abundance of the 1-10 fragment is low such as primary macrophages.

Chapter 4

Zinc Adequacy Improves Clearance of *Salmonella* in Infected Immune Competent Primary Macrophages

4.1 Abstract

Zinc (Zn^{2+}) is a required micronutrient for the growth of both mammalian cells and their bacterial pathogens. Intracellular pathogens such as *Salmonella sp.* colonize macrophages to form systemic infections and must acquire enough Zn^{2+} to survive and replicate within their host cell. The interface of this infection is defined largely by a tug of war for Zn^{2+}. In addition to being a limiting resource for pathogen growth, Zn^{2+} is essential for maintaining redox homeostasis and resisting damage from the oxidative burst of macrophages. In response to infection, macrophages actively sequester Zn^{2+} from the extracellular milieu and store it in metallothioneins (MTs). We examine what the consequence of increased MT expression meant for the labile Zn^{2+} pool, and whether or not it impacted the outcome of the infection. We used bone marrow derived macrophages (BMDMs) from immune competent mice and subtle Zn^{2+} manipulations to characterize infection with *Salmonella* Typhimurium under Zn^{2+} adequate or Zn^{2+} deficient conditions. We measured intracellular *Salmonella* replication in BMDMS and show enhanced replication under Zn^{2+} adequate conditions but also see that infection load is increased as Zn^{2+} is depleted from the extracellular media. We quantified an increase in the cytosolic labile Zn^{2+} pool of infected BMDMs after 12 hours post infection using a genetically encoded Zn^{2+} sensor and concomitantly show upregulation of the Zn^{2+} transporter SLC39A14 (Zip14). Additionally, splicing of Xbp1 mRNA in infected BMDMs is reduced upon Zn^{2+} treatment. We suggest that Zn^{2+} adequacy is more beneficial to the host due to enhanced bacterial clearance and resistance to ER stress.

4.2 Publication Status

This work is unpublished.

4.3 Introduction

Intracellular pathogens such as M*ycobacterium* or *Salmonella* thrive inside of host macrophages where a key feature of their infection is the ability to manipulate host metal cation traffic in order to ensure their survival inside the phagosome[13–15,63,65,67,72]. Acquisition of nutrients including iron, manganese, zinc and copper are limiting for the growth of the pathogen[56,212]. Host defense mechanisms actively sequester these nutrients either through efflux from the phagosome with divalent metal cation transporters such as natural resistance associated macrophage protein-1 (Nramp-1) or through the expression of metal binding proteins, like transferrin, ferritin, and metallothionein (MT)[55,75]. On a physiological level, exposure to pathogen molecular patterns (PAMPs) like lipopolysaccharide (LPS) trigger rapid changes to Zn^{2+} homeostasis and redistribution of Zn^{2+} into vital organs causing hypozincemia[135,138,140,213]. The role of acute hypozincemia is thought to be host protective while simultaneously restricting the access of zinc to invading pathogens.

Zn^{2+} redistribution in response to microbial insults is not limited to essential organs. Macrophages continue the paradigm of Zn^{2+} sequestration once they've been activated by phagocytosis of a pathogen or exposure to proinflammatory stimulus. The first observation of altered Zn^{2+} homeostasis in monocytes in response LPS showed an increase in MT production[214]. It was hypothesized that the increase in MT protein expression might actually drive Zn^{2+} sequestration and that would reduce the labile Zn^{2+} pool inside the cell. Since then, several studies have attempted to measure Zn^{2+} levels to some extent in macrophage models of infection[61,62,123,133,215]. All of those studies confirm that total Zn^{2+} increases within macrophages in response to intracellular pathogens in both human and mouse models. They also confirm a similar mechanism, increased expression of at least one SLC39A (Zip) transporter and an increase in MT expression.

Macrophages display a surprising divergence in the mechanisms by which they attempt to clear an intracellular pathogen based on the identity of the pathogen. In addition to the oxidative burst,

macrophages infected with *Mycobacterium tuberculosis* load toxic amounts of zinc and copper into the phagolysosome in an attempt to poison the bacterium[63]. Macrophages that are pre-activated with granulocyte-macrophage colony stimulating factor (GM-CSF) and infected with the fungal pathogen *Histopasma capsulatum* will remove Zn^{2+} from the pathogen containing vacuole in an attempt to starve and limit pathogen survival[61]. How certain macrophages decide which strategy to use against which pathogen is still unknown. In a human model of *Salmonella* infection, one group showed that *Salmonella* is able to subvert the fusion of Zn^{2+} containing vesicles with the *Salmonella* containing vacuole (SCV) in a SPI-1 dependent manner, but *E. coli* was not able to prevent such fusion[62]. So, it may be that subjecting pathogens to Zn^{2+} stress is a typical strategy of macrophage but some pathogens such as *Salmonella* have evolved a mechanism to combat this.

Critical comparison between nutritional immunity studies is difficult because there are major differences in the types of macrophage models used across studies. For example, RAW264.7 cells, a popular mouse macrophage cell line used to study intracellular pathogens, are derived from C57BL/6 mice which lack a functional NRAMP-1, a transporter for iron and manganese. This makes the cell more susceptible to infection and reduces its ability to clear intracellular pathogens[64,75,183]. Primary cells derived from mice of this genetic background are also compromised in the same way. 24% of orthologous genes in human monocyte derived macrophages (HMDMs) and bone marrow derived macrophages (BMDMs) from C57BL/6 mice are divergently regulated in response to LPS stimulus[216]. Among the divergently regulated genes are immune response genes such as NOS2 and inflammatory cytokines IL-1b and IL-6. Cell lines also behave differently from primary cells. A study of *M. tuberculosis* infection in C57BL/6 BMDMs compared with the J774 cell line revealed that the speed and magnitude of differentially regulated response genes from the primary cells was greater, indicating that important differences exist in these macrophage models where both were classified as resistant to *M. tuberculosis*[185]. Another important difference between cell lines and primary cells is that the surface receptors and downstream signaling capacities of a cell line can change with continuous culture[186].

Comparison between studies is further complicated by the variety of Zn^{2+} treatments, or lack thereof, to assess the functional role of Zn^{2+} on host biology or infection outcome. Several studies attempt to make functional assumptions about host cell biology when they use a Zn^{2+} treatment of >100 μM on infected cells[61–63,123] while serum Zn^{2+} concentration is typically between 10 and 30 μM[81,217,218]. Equally as problematic is that studies often report a "Zn^{2+} deficient" model by using a cell permeable Zn^{2+} chelator such as N,N,N′,N′-tetrakis-(2-pyridylmethyl)-ethylenediamine (TPEN) or Tris(2-pyridylmethyl)amine (TPA). Cell permeable Zn^{2+} chelators have very low dissociation constants for Zn^{2+} binding, 2.6 x 10^{-16} M for TPEN and 10^{-11} M for TPA[219], and can be quite toxic to cells due to their ability to strip metalloproteins of their zinc. TPEN not only affects Zn^{2+}, its highest affinity is for Cu^{2+} binding (K_d = 3 x 10^{-20} M). The 24 hour IC_{50} for HeLa cells is 38 ± 1 μM for TPA and 25 ± 2 μM for TPEN[219]. Data from our lab shows greater than 80% cell death in MCF10A cells treated with 3 μM TPEN for 24 hours, while in the same cells 5 μM TPA causes less than 15% cell death over 24 hours. While TPA is less toxic than TPEN, there is considerable variability in the sensitivity of different cell types to chemical zinc chelation so care must be taken to consider the impact on cell viability for a given treatment.

Several open questions remain in regards to zinc dyshomeostasis in macrophages. How does the macrophage mechanism of Zn^{2+} stress or starvation affect the clearance of the pathogen? Are the mechanisms of Zn^{2+} sequestration adequate for reducing zinc availability to the pathogen? Does the nutritional Zn^{2+} status of the macrophage impact the mechanism of zinc redistribution? How does the nutritional Zn^{2+} status of the macrophage impact the clearance of the pathogen?

We employ primary BMDMs from immune competent 129SV mice and use WT *Salmonella* Typhimurim (here after referred to as *Salmonella*) as an infection model for investigating the nature of zinc regulation at the host pathogen interface[65]. We quantified the cytosolic labile Zn^{2+} pool in resting and infection conditions and find that cytosolic labile [Zn^{2+}] increases 12 hours post infection and remains elevated up to 24 hours post infection. We observed changes in the expression of 5500 genes in response to infection and see that many Zn^{2+} regulatory genes are impacted, including the upregulation of Zip14. We measured the replication and bacterial load of infected BMDMs over the

course of infection upon manipulation of Zn^{2+} conditions. We find that Zn^{2+} adequacy increases replication in intracellular bacteria but also decreases bacterial burden compared to Zn^{2+} deficient conditions. We show that Zn^{2+} addition reduces splicing of Xbp1 mRNA compared to Zn^{2+} deficient conditions across the infection time course, indicating that ER stress is enhanced under zinc deficiency.

4.4 Quantification of labile Zn^{2+} in *Salmonella*-infected BMDMs

The hypothesis that increased MT expression drives the sequestration of labile Zn^{2+} and whether or not the added buffering capacity these molecules is sufficient to lower the labile zinc pool within the cell has not been adequately addressed. The most popular method for measuring Zn^{2+} uses staining with a fluorogenic Zn^{2+} dye such as FluoZin3 or Zinpyr-1 and then imaging or analyzing cells with flow cytometry. One complication with small molecule indicators for zinc is their unpredictable localization within a cell. Fluozin3-AM, arguably the most common indicator for zinc in use, has been shown to localize to the cytosol[220–222], golgi[223], lysosomes[224], and vesicles[225,226] and localizations may differ among cell types[223]. While this can be advantageous for measuring specific Zn^{2+} pools within a cell, care must be taken to ensure that the probe doesn't report Zn^{2+} from multiple cellular locations. The localization of FluoZin3 in THP1 cells and HMDMs appears to localize to vesicles or early endosomes[62,133], in RAW264.7 cells Fluozin3 localizes to the cytosol and puncta[123]. Of the studies that have attempted to measure zinc inside of activated or infected macrophage, none have successfully answered whether the labile zinc pool inside the cytosol of these macrophages is lowered by MTs.

To address this, we used the genetically encoded zinc sensor NES-ZapCV2 in immune competent BMDMs at rest or infected with *Salmonella* at various times post infection (Figure 4.1). NES-ZapCV2 is a Förster resonance energy transfer (FRET) based zinc sensor that is localized to the cytosol that registers changes in zinc concentration as changes in FRET efficiency. The benefit of using a ratiometric sensor is that it can provide a more accurate quantification of labile Zn^{2+} than intensiometric sensors[227]. BMDMs from 129SV mice were transiently transfected on day 6 post differentiation using Nuclefector technology. Transfected cells were plated into imaging dishes and allowed to lay down and recover for 15 hours before infection or before imaging (Figure 4.1A). A representative image of transfected BMDMs expressing sensor is presented in Figure 4.1B. Dishes

were imaged on a widefield microscope, collecting multiple fields of view, while a sensor calibration was carried out to enable quantification of labile Zn^{2+}. Time lapse movies were processed in Matlab using a segmentation algorithm to extract single cell traces of each fluorescence channel and calculate the FRET ratio (Figure 4.1C). Resting FRET ratios were collected for approximately 10 minutes until a cell permeable Zn^{2+} chelator TPA was added to measure the minimum FRET response of the sensor in each cell. After the minimum FRET signal was collected, TPA was washed out and a solution containing buffered Zn^{2+} and the ionophore pyrithione was added to the cells to measure the maximum FRET response. The resting, minimum, and maximum FRET ratios for each cell were used to calculate the fractional saturation, the dynamic range, and the reported $[Zn^{2+}]$ from the sensor in each cell. The dynamic range of the sensor can be impacted by both over expression and under expression of the sensor which has a negative impact on the fidelity of the apparent $[Zn^{2+}]$[228]. For this reason, cells were excluded from the analysis if they fell outside of an acceptable dynamic range, 1.6 – 2.3 for the NES-ZapCV2 sensor.

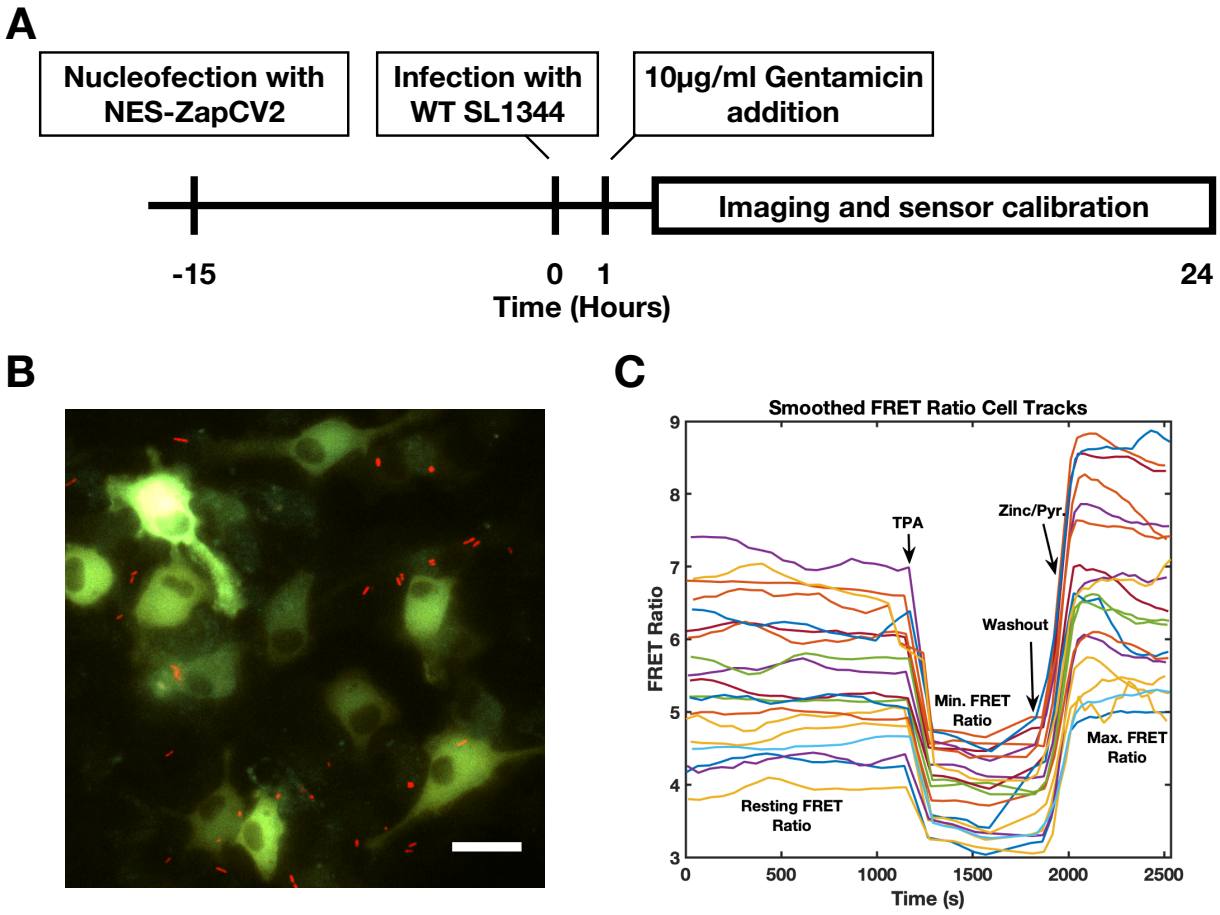

Figure 4.1 Transfection of BMDMs with NES-ZapCV2 allows for quantification of labile cytosolic zinc levels in single cells under infection conditions.
A) Timeline of transfection and infection experiments. On day 6 of differentiation, isolated BMDMs were transfected with NES-ZapCV2 and seeded into imaging dishes for 15 hours prior to infection. Imaging dishes were infected with WT SL1344 for 1 hour. Infected dishes are washed and media containing 10 µg/ml gentamicin is added to inhibit growth of extracellular bacteria. Infections are imaged at time points post infection and sensor calibrations are performed to quantify sensor response. **B**) Representative fluorescence overlay image of BMDMs expressing NES-ZapCV2 (in green) infected with WT SL1344 constitutively expressing mRuby3 under the rpsm promoter (in red). Scale bar is 20 µm. **C**) Representative FRET ratio traces from single cells in a sensor calibration. The resting FRET ratio was collected initially to establish a baseline FRET ratio. Zinc was then chelated with TPA, to establish the minimum FRET ratio of the sensor. TPA was washed out and a buffered zinc solution containing the ionophore pyrithione was added to saturate the sensor and measure the maximum FRET ratio response. Each trace shows an individual cell.

Fractional saturation of NES-ZapCV2 in BMDMs infected with *Salmonella* for 1 to 8 hours post infection indicates a slight decrease in zinc compared to control, while from 12 – 24 hours post infection it is significantly elevated (Figure 4.2).

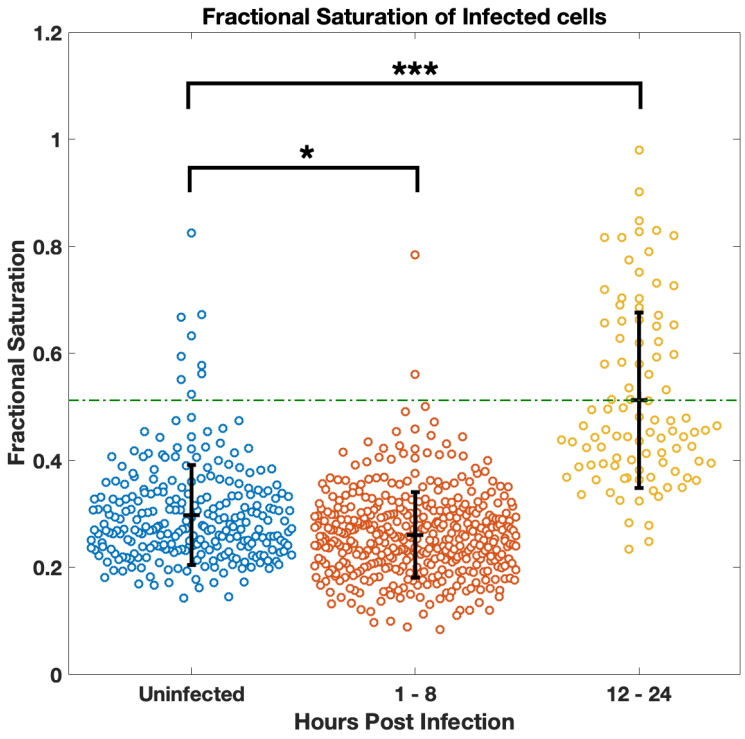

Figure 4.2 Quantification of cytosolic labile Zn^{2+} in *Salmonella*-infected BMDMs
Fractional saturation (FS) of NES-ZapCV2 sensor in *Salmonella*-infected and uninfected BMDMs shows differences in labile zinc levels at different time points post infection. Each point represents the resting FS of the ZapCV2 sensor for an individual cell measured under each condition listed. Uninfected cells have a mean FS of 0.30, $[Zn^{2+}]$ = 80 pM, n = 267 cells. FS remained low for infected dishes measured from 1 to 8 hours post infection, those early infection populations are pooled, with a mean FS of 0.26, $[Zn^{2+}]$ = 45 pM, n = 417 cells. FS increased after 12 hours post infection and remained elevated up to 24 hours post infection. Late infection populations (12-24 HPI) are pooled for this analysis with a mean FS of 0.51, $[Zn^{2+}]$ = 2.9 nM, n = 99 cells. *** P-value = 1.95 e-40. * P-value = 2.30 e-07

For the purposes of this analysis, cells imaged from 1 to 8 hours post infection were pooled because there was a similar fractional saturation, suggesting similar $[Zn^{2+}]$ at each time point. Cells analyzed from 12 to 24 hours were pooled for the same reason. Uninfected cells report a mean FS of 0.30 which corresponds to a $[Zn^{2+}]$ of 80 picomolar. Early infected cells report a mean FS of 0.26 which corresponds to a $[Zn^{2+}]$ of 45 picomolar. Late infected cells had a mean FS of 0.51 which is about 2.9 nanomolar $[Zn^{2+}]$. Our data show that labile zinc in the cytosol does indeed increase later in the infection. While

this does not directly address the buffering capacity of MT, it does show that despite increased MT expression the exchangeable Zn^{2+} pool is increased later in the infection. One possible explanation for this observation is that the buffering capacity of MTs is governed not only by their quantity, but also by their redox state[229] and the pH of the intracellular environment. Infected macrophages undergo a respiratory burst early in infection that is dependent on phox47 and generate reactive oxygen species (ROS)[164]. A longer, more sustained amount of reactive nitrogen species (RNS) are produced throughout infection by inducible NO synthase (iNOS)[163]. ROS and RNS react with free cysteine residues and modulate the redox environment within the infected macrophage. The labile Zn^{2+} pool within the cytosol may be directly tied to the redox status of the cell[229].

4.5 Global Changes to Zn^{2+} Regulatory Genes in Response to Infection

In order to determine the genes involved in contributing to our observed zinc phenotype, we measured the gene changes in BMDMs in response to *Salmonella* infection at 2 and 18 hours post infection using global RNAseq (Figure 4.3). Data collection and analysis was performed by Lara Janiszewski. At 18 hours post infection we see changes in 5500 genes including significant changes in genes involved in Zn^{2+} and metal homeostasis (Figure 4.3A). At 2 hours post infection we see increased MT2 expression, a decrease in Zip4, and no large changes in ZnT genes which fits with the slight decrease we see in labile [Zn^{2+}] (Figure 4.3B). At 18 hours post infection, the largest change in expression of the zinc regulatory genes is in the zinc importer Zip14. There is also an increase in MT2 and Zip4 and a decrease in several zinc exporters, ZnT1, Znt5, and ZnT4. Together, the directional changes of the Zn^{2+} regulatory genes support a model of increased Zn^{2+} sequestration and increased influx of Zn^{2+} into the cytosol of the BMDMs. We also see an increase in Nramp1, the gene involved in resistance to intracellular pathogens, including *Salmonella*, which is a good indicator that this gene is important in this model system. Importantly, we see a decrease in the expression level of Zip8 at 18 hours, a gene reported to be upregulated in response to LPS in both HMDMs and RAW264.7 cells[133], indicating that there may be an important difference between these genetic backgrounds. The upregulation of Zip14 in BMDMs of this genetic background is consistent with what has been reported in BMDMs treated with LPS[144] and it may share a common regulation pattern with hepatocytes. Zip14

is the Zn^{2+} regulatory gene most upregulated in mouse liver in conditions of inflammation or LPS treatment which is responsible for inducing acute hypozincemia[135]. Zip14 is required for resistance to ER stress in hepatocytes and is regulated by ATF4 and ATF6a transcription factors, which are essential in the unfolded protein response (UPR) [137].

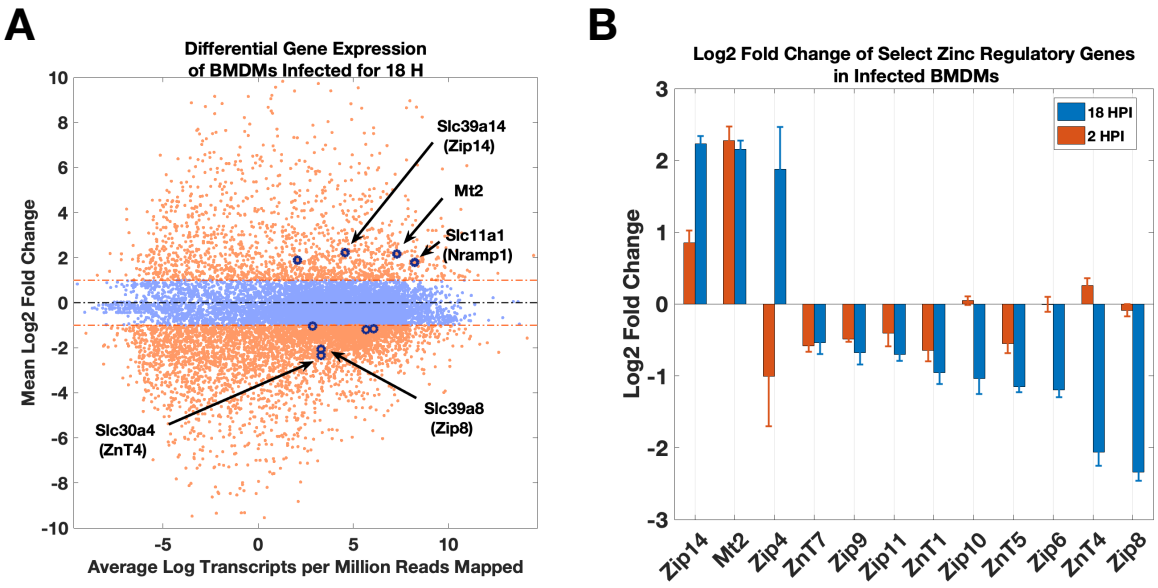

Figure 4.3 Global RNAseq of *Salmonella*-infected BMDMs show changes in zinc homeostasis genes. RNAseq of *Salmonella*-infected BMDMs shows changes in expression of over 5500 genes including many zinc regulatory genes and genes related to metal homeostasis. Comparison of changes made in zinc genes between 2 hours post infection and 18 hours post infection demonstrates the dynamic nature of zinc homeostasis genes across the infection landscape. **A**) Differential gene expression of *Salmonella*-infected BMDMs at 18 hours post infection compared to uninfected cells, displayed as a function of the average log of transcripts per million reads mapped. Select genes involved in zinc homeostasis are highlighted with a dark circle. Also highlighted is Nramp-1, a metal ion transporter that is critical for host resistance to many intracellular pathogens including *Salmonella*. The most strongly upregulated gene is the zinc transporter Slc39a14 (Zip14). **B**) Log2 fold change of select zinc homeostasis genes at 2 and 18 hours post infection compared to uninfected cells are displayed from highest upregulated to lowest down regulated gene.

4.6 Intracellular *Salmonella* Replication is Influenced by Nutritional Zn^{2+} Status

The changes in labile [Zn^{2+}] that we observed were measured in the cytosol but the intracellular *Salmonella* are contained in the SCV. We wondered what affect, if any, the increase in intracellular

Zn^{2+} had on the pathogen. Additionally, since an increase in Zip14 expression in the liver due to inflammation leads to a reduction in serum [Zn^{2+}], we sought to probe the role of nutritional Zn^{2+} on the infection outcome using defined concentrations of Zn^{2+} in cell culture media in a range that is similar to zinc concentrations seen in physiological conditions. To do this, we used a *Salmonella* strain harboring the fluorescence dilution plasmid pDiGc developed in the in the Holden lab by Sofie Helaine et. al[184,230,231]. pDiGc encodes for two fluorescent proteins, DsRed under control of an arabinose inducible promoter and eGFP under control of the constitutive rpsm promoter. Bacteria are grown in arabinose containing LB to induce to expression of the DsRed protein before infection. Bacterial replication can be monitored by comparing the intensities of the GFP and the DsRed as the DsRed signal is diluted between mother and daughter cells and is not replenished in the absence of additional arabinose. BMDMs were grown in untreated media until day 7 of differentiation when they were infected with arabinose induced SL1344 pDiGc MOI 10 or MOI 30 for 1 hour when the media was changed to one containing 10μg/ml gentamicin to inhibit the growth of extracellular bacteria. At 2 hours post infection the media was changed to media containing 20% chelex treated serum, 10μg/ml gentamicin, and one of three Zn^{2+} manipulations to create 4 conditions; chelex treated media alone, 30 μM Zn^{2+}, 3 μM ZX1, or 1 μM TPA. ZX1 is a cell impermeable Zn^{2+} chelator based on dipicolylamine and sulfonate groups[232]. At specific time points, cells were fixed. Prior to fixing, a small aliquot of cells was taken to plate for CFU. Samples were collected at 2, 10, 18, and 24 hours post infection. Each sample was analyzed using flow cytometry to measure eGFP and DsRed fluorescence, 488 nm and 561 nm respectively. The gating strategy is presented in Figure 4.4. All events were gated for single cells based on forward and side scatter. GFP positive cells were gated above the uninfected cell population in the 488 nm channel (Figure 4.4A). Cells containing replicating bacteria were identified by selecting cells that had a 488 nm : 561 nm ratio that was higher than the initial inoculation population (Figure 4.4B). Replication positive cells were compared for fluorescence dilution in the 561 nm channel at each time point to assess the extent of replication (Figure 4.4C).

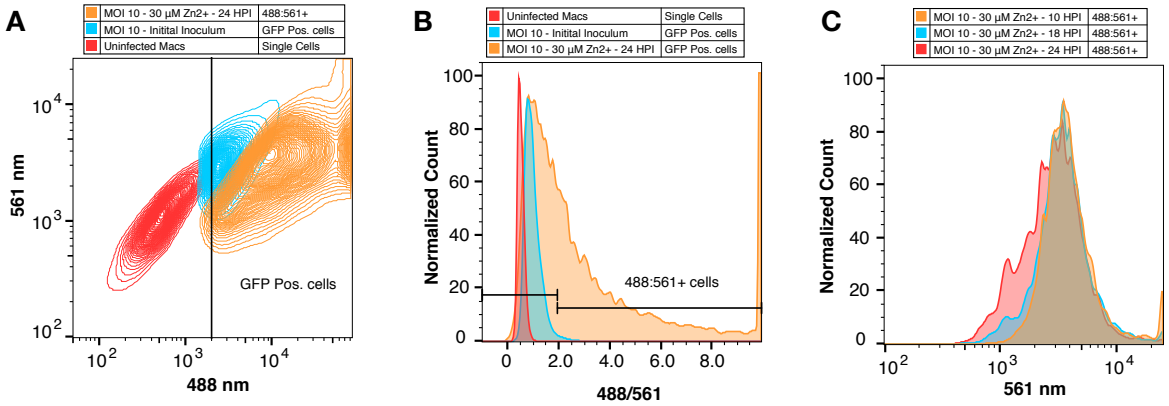

Figure 4.4 Gating strategy of flow cytometry analysis of BMDMs infected with WT SL1344 pDiGc. **A**) Contour plot of the 488 nm excitation and 561 nm excitation fluorescence signal intensities showing an overlay of uninfected single BMDMs (red), single cells that were GFP positive BMDMs from the initial infection conditions (blue), and BMDMs infected for 24 hours and gated on the ratio of 488nm:561nm fluorescence channels (orange). The GFP positive gate was set above the max fluorescence intensity of the uninfected population (vertical line). **B**) A normalized histogram of the ratio of 488nm:561nm fluorescence channels showing the overlay of uninfected (red), initially infected (blue), and 24 hour infected (orange) populations. The gate for selecting the replicating population of cells was set to be above (right side of plot) 98% of the initial infection or unreplicated population (blue). The 24 hour infected cells demonstrate how fluorescence dilution from bacterial replication shifts the population to have a higher 488:561 ratio. **C**) A normalized histogram of the 561 nm fluorescence channel of a representative infection shows how red fluorescence is diluted over the course of the infection. 10 hours post infection (orange) shows higher 561 nm fluorescence compared to both 18 hours post infection (blue) and 24 hours post infection (red).

The fluorescence intensity of the events in the TPA treated samples were lower than non-TPA treated cells. We are unsure of the reason for the fluorescence intensity shift, but possible explanations include: a shift in background fluorescence upon TPA treatment, a decrease in DsRed intensity, or a decrease in the viability of the whole population, as suggested by the significantly reduced frequency of events gated from the parent population, which enriched for cells that had replicated more. Direct comparison of the TPA condition with the other Zn^{2+} manipulations shows that the entire population of cells shifted making the assessment of replication difficult (Figure 4.5). Consequently, we chose to exclude TPA from the analysis where direct comparison is made to the other zinc treatments.

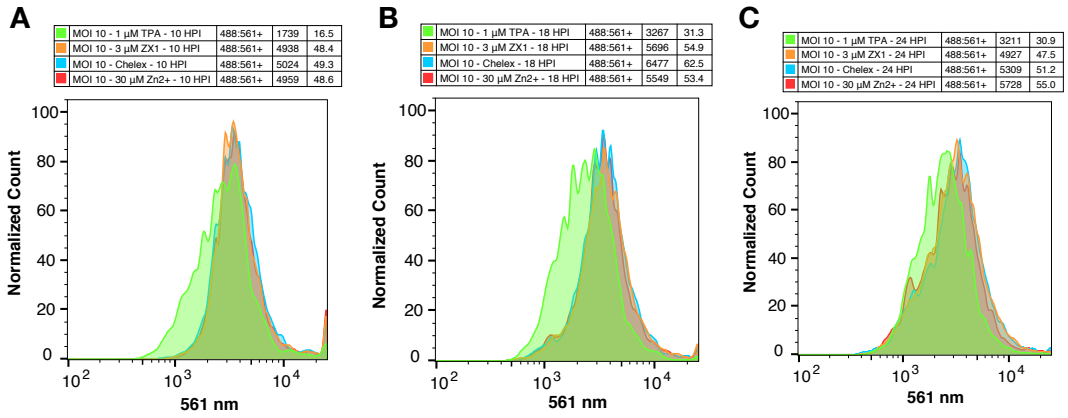

Figure 4.5 TPA treated cells show distinct fluorescence from other zinc conditions. Normalized histogram overlays of the four zinc conditions show that TPA treated cells are distinct from each of the other samples at each time point of infection: **A**) 10 hours post infection, **B**) 18 hours post infection, **C**) 24 hours post infection. Each legend lists the name and color of the condition, the number of cells included from each subpopulation, and the percentage of the parent population. While the shape of the TPA treated population is similar to the other samples, the whole population appears dimmer than the others making it difficult to make direct comparisons using this gating method. TPA will be excluded from direct comparison to the other zinc conditions for rest of the analysis.

Comparison of the 561 nm replication profile for time points of each Zn^{2+} manipulation shows that replication is occurring from 10 hours to 18 hours and from 18 to 24 hours in each condition (Figure 4.6A – C). 30 μM Zn^{2+} treatment displays a more prominent replication shoulder that fades as each treatment becomes more depleted in Zn^{2+} levels. Direct comparison of each Zn^{2+} manipulation for each time point shows that the replication profile is nearly identical at 10 hours (Figure 4.6D) and 18 hours, with a slightly greater shift in the 30 μM Zn^{2+} treatment (Figure 4.6E). At 24 hours, the 30 μM Zn^{2+} treatment gives rise to more replication than either the Chelex treated or the ZX1 treated media (Figure 4.6F). This indicates that Zn^{2+} adequate conditions increase the amount of intracellular bacterial replication. The cytosolic Zn^{2+} elevation may be accessible to bacteria inside of their SCV, or it could be that elevated zinc reduces the host cell's ability to limit bacterial replication by some other mechanism. The 488 nm:561 nm (+) subpopulation characteristics of these samples are listed in Table 4.1.

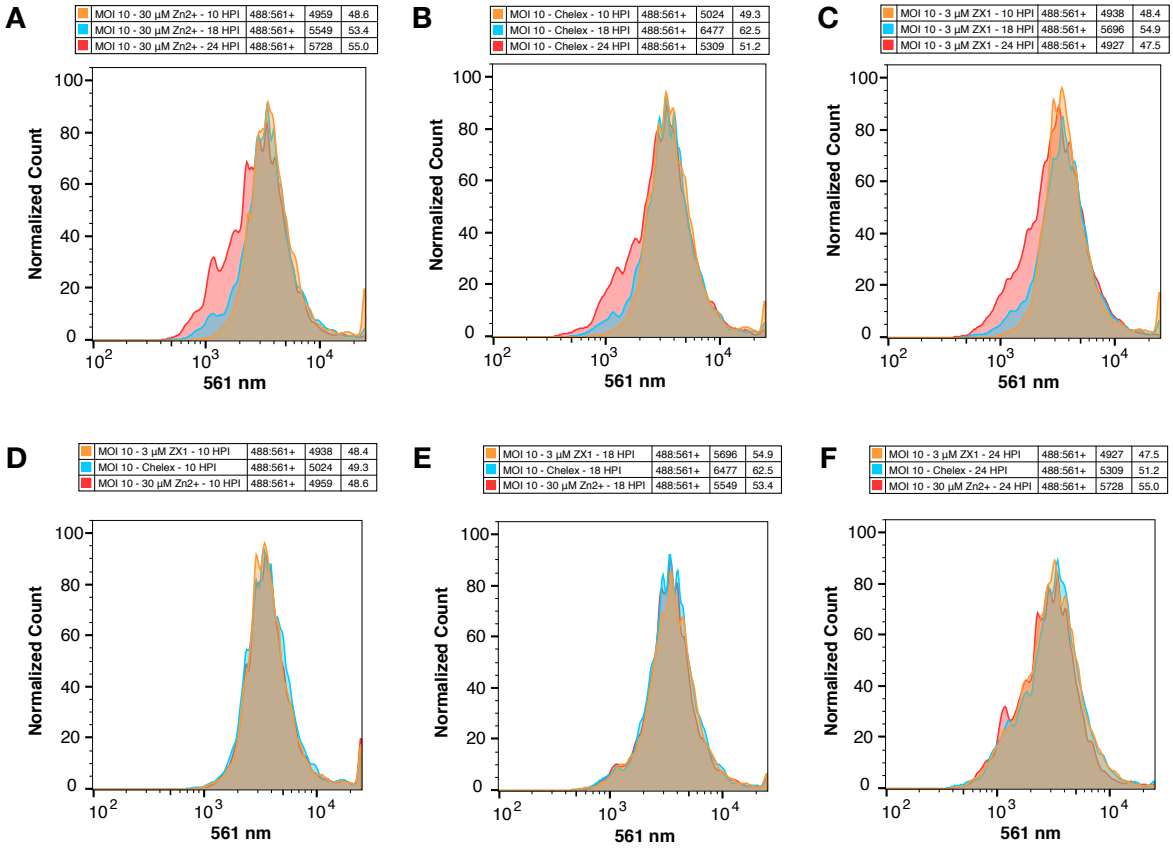

Figure 4.6 Comparison of fluorescence dilution profiles of each zinc condition.
Normalized histograms in the 561 nm channel of each zinc condition overlaid with their respective time course (**A - C**) or overlaid with each other at each time point (**D - F**). Each legend lists the name and color of the condition, the number of cells included from each subpopulation, and the percentage of the parent population. Population characteristics are listed in Table 1 and 2. The 561 nm fluorescence profiles of each condition are similar at each timepoint indicating similar replication dynamics with the exception of the 24 hour timepoint. At 24 hours there is a shoulder that appears for the 30 µM Zn^{2+} condition that fades in treatment conditions that are more depleted of zinc. Direct comparison of this timepoint (**F**) shows that there is indeed more fluorescence dilution or replication that is occurring in the 30 µM Zn^{2+} condition.

		MOI 10				MOI 30			
Sample	Subset	Count	Percent	Mean 561	ΔMean 10HPI	Count	Percent	Mean 561	ΔMean 10HPI
30μM Zn2+ - 10 HPI	488:561+	4959	48.6	3867	0	4775	46.7	4472	0
30μM Zn2+ - 18 HPI	488:561+	5549	53.4	3411	-456	5583	53.7	6277	***
30μM Zn2+ - 24 HPI	488:561+	5728	55	2771	-1096	5082	49	3186	-1286
Chelex - 10 HPI	488:561+	5024	49.3	3817	0	4953	48.5	4090	0
Chelex - 18 HPI	488:561+	6477	62.5	3483	-334	5591	54.3	3708	-382
Chelex - 24 HPI	488:561+	5309	51.2	3000	-817	5325	51.3	3215	-875
3μM ZX1 - 10 HPI	488:561+	4938	48.4	3840	0	5224	51.1	4569	0
3μM ZX1 - 18 HPI	488:561+	5696	54.9	3553	-287	5976	56.9	6900	***
3μM ZX1 - 24 HPI	488:561+	4927	47.5	2975	-865	5902	56.7	3319	-1250
1μM TPA - 10 HPI	488:561+	1739	16.5	2735	0	2223	21.5	3499	0
1μM TPA - 18 HPI	488:561+	3267	31.3	2374	-361	3860	37.1	2537	-962
1μM TPA - 24 HPI	488:561+	3211	30.9	2370	-365	3788	36.7	2541	-958
DMSO - 10 HPI	488:561+	3382	41.8	4338	0	4264	47.7	4497	0
DMSO - 18 HPI	488:561+	5156	57.5	3322	-1016	4665	51.6	3659	-838
DMSO - 24 HPI	488:561+	4654	52.4	2862	-1476	3956	44.3	3245	-1252
200 nM ISRIB - 10 HPI	488:561+	4857	47.2	3726	0	4991	49	4697	0
200 nM ISRIB - 18 HPI	488:561+	5096	49.4	3321	-405	4793	46.7	3540	-1157
200 nM ISRIB - 24 HPI	488:561+	5700	54.8	2792	-934	5456	52.6	3201	-1496
600 nM ISRIB - 10 HPI	488:561+	3640	38.3	6796	***	3715	42.4	4339	0
600 nM ISRIB - 18 HPI	488:561+	4155	49.1	3298		3807	43.5	3877	-462
600 nM ISRIB - 24 HPI	488:561+	4046	45.7	3135					

Table 4.1 Characteristics table of the 488:561+ subpopulations.
The geometric mean of the 561 nm fluorescence channel is displayed under "Mean 561". The ΔMean 10 HPI is the change in the geometric mean using the treatment condition's own 10 hour timepoint as the control allowing for the quantification of replication that occurs from 10 hours to the subsequent time points. For the zinc treatment populations, 30μM Zn^{2+} treatment displays the most replication at 24 hours for both MOI 10 and MOI 30. *** indicates that the sample was not fixed using formaldehyde, changing the fluorescence characteristics so the sample could not be included in the analysis.

4.7 Intracellular *Salmonella* Replication is Affected by the Integrated Stress Response Inhibitor, ISRIB

In hepatocytes, Zn^{2+} accumulation and Zip14 upregulation were required for adaptation to ER stress[137]. The Zip14 promoter has binding sites for two transcription factors that are products of the unfolded protein response (UPR), ATF6α and ATF4, which is a product of PERK mediated phosphorylation of eIF2α[137]. We reasoned that if the increase in Zip14 observed at late stages of infection was related to the ER stress response in BMDMs then we could reduce the strength of the response upon pharmacological inhibition of PERK mediated phosphorylation. If we could reduce phospho-eIF2α and downstream activation of ATF4, then perhaps we could reduce Zip14 mRNA upregulation and potentially lower labile Zn^{2+} accumulation. Integrated Stress Response Inhibitor (ISRIB) is a drug that reverses the effects PERK mediated phosphorylation of eIF2α which serves to

restore protein translation under mild stress conditions[233]. We used ISRIB or DMSO as a treatment in the fluorescence dilution assay to monitor the effect of ISRIB on intracellular *Salmonella* replication. The IC_{50} of ISRIB is 20 nM. We used two concentrations of ISRIB, 200 nM and 600 nM, and DMSO as the vehicle control. Comparison of the 561 nm replication profile of each timepoint for each condition shows that replication is occurring at each time and it appears that the most replication occurs in the 200 nM ISRIB condition (Figure 4.7A – C). Comparing each condition directly at each timepoint shows more clearly that the 200 nM ISRIB treatment has more bacterial replication than DMSO (Figure 4.7D – F). 600 nM ISRIB treatment seems to have nearly identical replication as DMSO at 18 hours (Figure 4.7E), but at 24 hours has less replication than DMSO. The 488 nm:561 nm (+) subpopulation characteristics of these samples are listed in Table 4.1.

The 600 nM ISRIB treatment seems to reverse the replication pattern seen for 200 nM ISRIB treatment which is unexpected since a dose dependent response does not seem to occur. However, this observation may be explained by the mechanism of action for ISRIB. During translation initiation the five subunits of eIF2B form a decamer to bind its substrate, eIF2, and methionine initiator tRNA and GTP[234]. Several kinases are capable of phosphorylating eIF2α under cellular stresses such as protein misfolding in the ER or increases in redox stress. Phospho-eIF2α binds the eIF2B decameric complex and acts as a competitive inhibitor of the formation of the ternary complex preventing the association with unphosphorylated eIF2 for nucleotide exchange[235,236]. ISRIB binds and stabilizes the eIF2B(βγδε) complex to form a dimer of tetramers before the binding of $eIF2B(\alpha)_2$ and enhances its GEF activity[237]. In the presence of 200 nM ISRIB the eIF2B(βγδε) complex has a 3-fold increase in GEF activity, and higher concentrations of ISRIB failed to have any effect. A look at the cryo-EM structure of eIF2B(βγδε) with ISRIB shows that ISRIB binds the symmetric cleft of each tetramer at the interface of the dimerization site stabilizing its formation, but at higher concentrations, ISRIB occupies the half sites of the eIF2B tetramer, interfering with octamer formation and therefore limiting the formation and activity of the decameric holoenzyme[238]. This suggests that there is a limited range of concentrations within which ISRIB can function and may explain why the 600 nM ISRIB treatment failed to elicit an effect compared to DMSO.

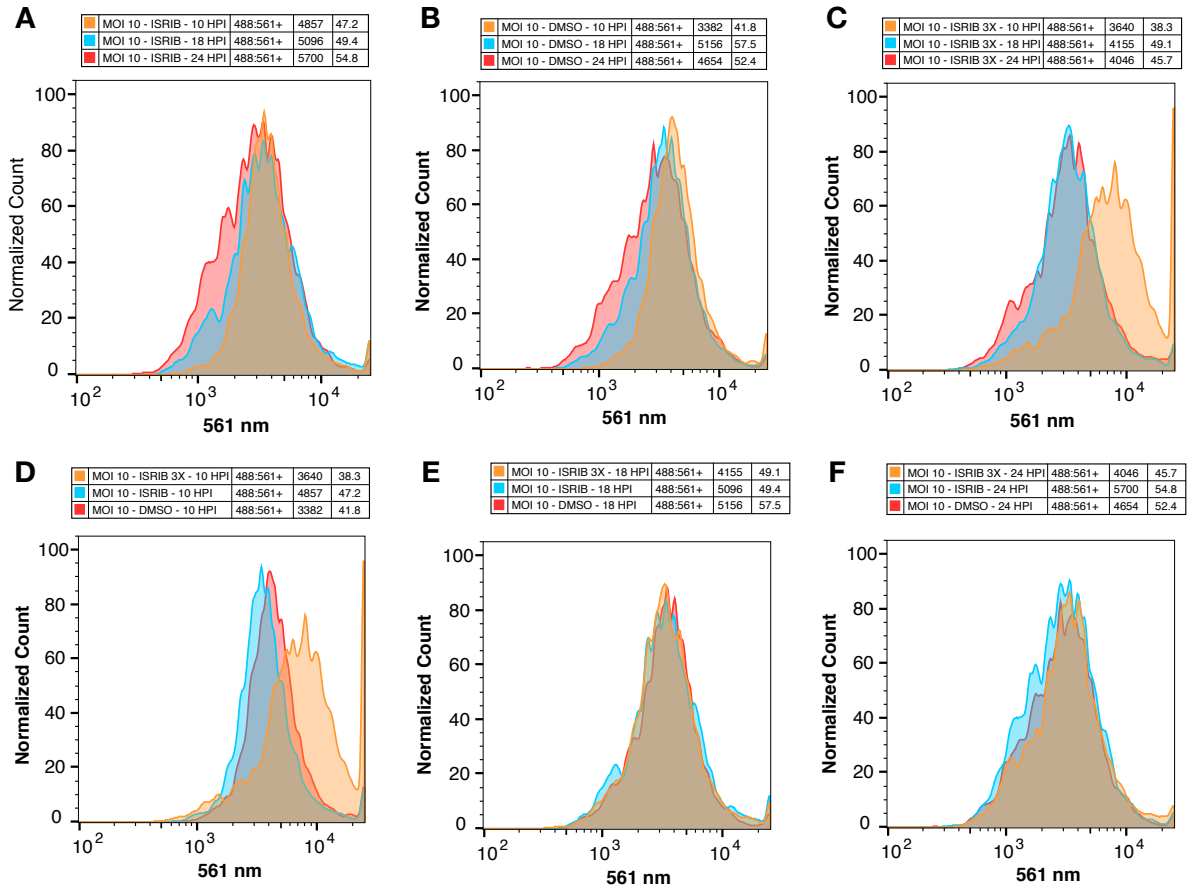

Figure 4.7 Comparison of fluorescence dilution profiles of ISRIB treatment of DMSO control. Normalized histograms in the 561 nm channel of ISRIB treatment or DMSO control treatment overlaid with their respective time course (**A** – **C**) or each treatment overlaid with each other at distinct time points (**D** – **F**). Each legend lists the name and color of the condition, the number of cells included from each subpopulation, and the percentage of the parent population. Population characteristics are listed in Table 1 and 2. 200 nM ISRIB alone shows more replication than DMSO at 24 hours post infection, while 600 nM ISRIB treatment (listed as 3X ISRIB) appears to reduce the extent of replication to below DMSO levels (**F**). The MOI 10 - ISRIB 3X sample was not fixed using formaldehyde, so the fluorescence intensity of the population is higher than all the other samples making direct comparison difficult (**C & D**).

4.8 Intracellular *Salmonella* Burden Enhanced During Nutritional Zn^{2+} Depletion or by Treatment With ISRIB

The intracellular bacterial burden depends on the rate of replication and the rate of bacterial killing. Since we measured an increase in intracellular *Salmonella* replication after treatment with 30μM Zn^{2+}, we wanted to know what effect each Zn^{2+} treatment or drug treatment had on the number

of *Salmonella* that could be recovered from the infection. To do this we took an aliquot of each infected sample of BMDMs prior to fixing for the fluorescence dilution assay, lysed them with 0.1% triton-X to release intracellular bacteria, and plated them on LB-agar to count CFU. In parallel we measured the percentage occurrence of GFP positive cells within the population of single cells collected in the fluorescence dilution assay and find that this shows a similar trend as CFU count (Figure 4.8). Numerical results are summarized in Table 4.2.

Bacterial load, as measured by CFU, and percent GFP positive cells show that bacterial burden increases over time for 30 μM Zn^{2+} treatment, chelex treated media and 3μM ZX1 treatment from 2 hours post infection to 18 hours post infection for both MOI 10 (Figure 4.8A) and MOI 30 (Figure 4.8B). At 24 hours post infection, 30 μM Zn^{2+} treatment shows a reduced bacterial burden, compared to the lower Zn^{2+} conditions, in both MOI 10 and MOI 30 as measured by CFU and percent GFP positive population. 1 μM TPA treatment universally and drastically reduced intracellular *Salmonella* burden. This is consistent with results from another study[123] and is not surprising given that TPA is membrane permeable and is therefore likely capable of entering into the SCV. The total bacterial load depends on the rate of killing and the rate of replication. For *Salmonella* incubated in 1 μM TPA the rate of replication is much lower than other treatments. A measurement of the amount of replication that occurs in 1 μM TPA treatment is given in the ΔMean 10HPI column of Table 4.1. 1 μM TPA treated cells have a small amount of replication that occurs from 10 hours post infection to 18 hours post infection but from 18 to 24 hours post infection there is no change in replication. This means that the rate of decline of *Salmonella* within the 1 μM TPA condition is due predominantly from the rate of killing of the macrophages, assuming no losses in host cell viability. It is important to note that TPA treatment may enhance the rate at which macrophages can kill intracellular bacteria, and that effect is not measured here.

Considering that 30 μM Zn^{2+} treatment enhanced intracellular *Salmonella* replication and Zn^{2+} restriction reduced it, yet the overall burden of *Salmonella* was reduced in 30 μM Zn^{2+} treatment, the rate at which macrophages can kill intracellular bacteria must have been enhanced for the 30 μM Zn^{2+} treated cells, or the rate at which macrophages can kill intracellular bacteria was reduced by Zn^{2+}

deprivation. Previously it was shown in HMDMs that 200 μM $ZnSO_4$ treatment reduced intracellular *Salmonella* burden by 24 hours post infection[62]. In that study they did not measure replication rate. To our knowledge, this is the first time that modest and physiologically similar zinc concentrations were shown to have an effect on the outcome of intracellular *Salmonella* infection.

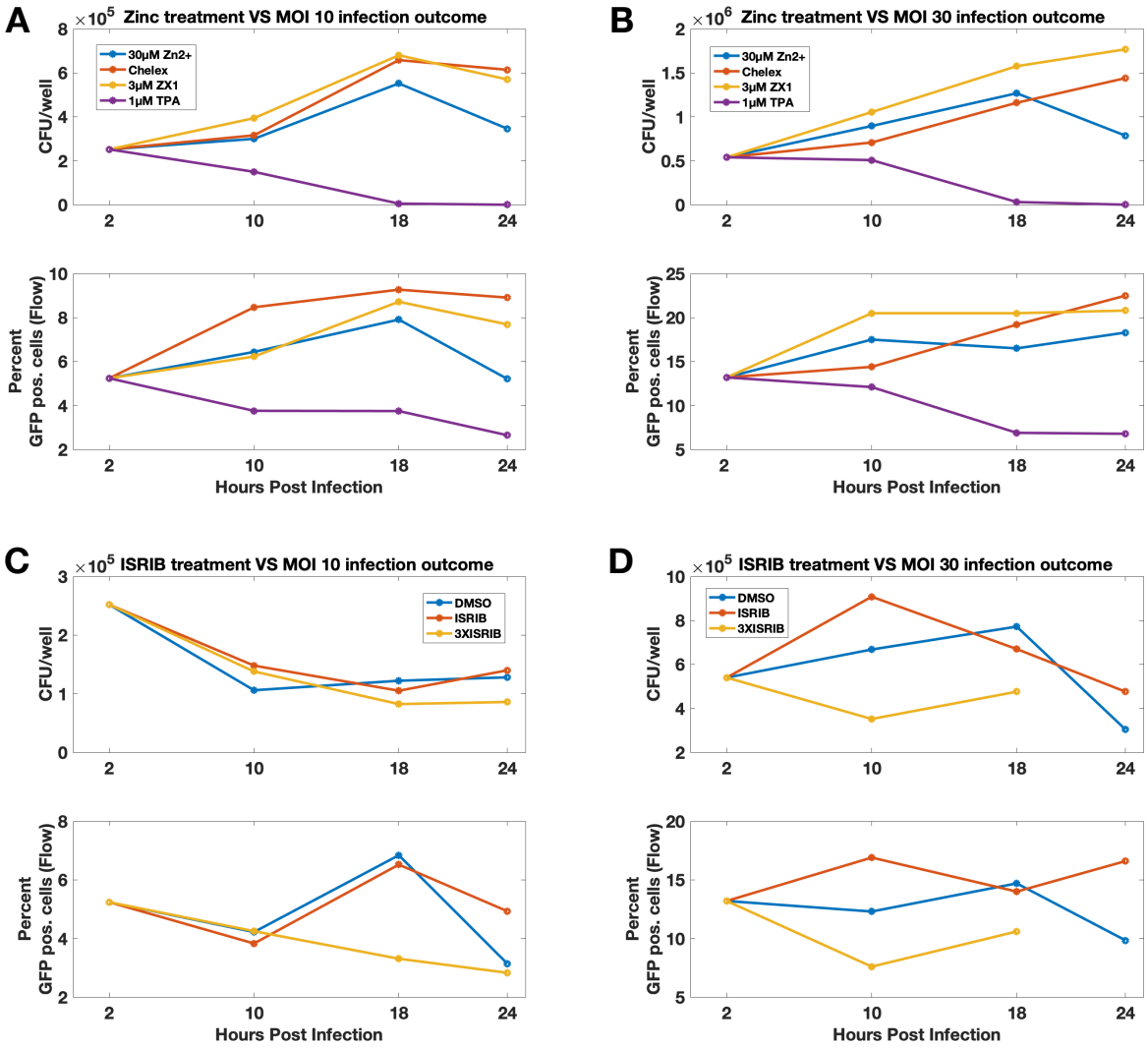

Figure 4.8 CFU infection load time course for zinc or drug manipulated cells
CFU and percent of GFP positive cells show similar trends for zinc or drug manipulated and infected cells at MOI 10 (**A & C**), or MOI 30 (**B &D**). While FACS showed that greater bacterial replication occurred under Zn^{2+} limiting conditions (Chelex, ZX1, TPA), both CFU and percent GFP positive cells indicate that there were fewer bacteria recovered from the 30 μM Zn^{2+} treated cells, suggesting that they are better at reducing bacterial load than either of the more zinc deplete conditions. The effect of ISRIB treatment on infection load is complicated and seems to depend on the time post infection. 3X ISRIB treatment (600 nM) seems to be better at reducing infection load than both 1X ISRIB and DMSO in both MOI 10 and MOI 30.

		MOI 10			MOI 30		
Sample	**Subset**	**Count**	**Percent**	**CFU*10^3**	**Count**	**Percent**	**CFU*10^3**
Initital Inoculum - 2 HPI	GFP Pos. cells	3022	5.24	252	6075	13.2	540
30μM Zn2+ - 10 HPI	GFP Pos. cells	10210	6.44	300	10228	17.5	896
30μM Zn2+ - 18 HPI	GFP Pos. cells	10383	7.91	552	10399	16.5	1268
30μM Zn2+ - 24 HPI	GFP Pos. cells	10408	5.21	346	10370	18.3	786
Chelex - 10 HPI	GFP Pos. cells	10200	8.47	316	10207	14.4	708
Chelex - 18 HPI	GFP Pos. cells	10360	9.27	658	10297	19.2	1160
Chelex - 24 HPI	GFP Pos. cells	10370	8.91	614	10372	22.5	1440
3μM ZX1 - 10 HPI	GFP Pos. cells	10209	6.23	394	10218	20.5	1054
3μM ZX1 - 18 HPI	GFP Pos. cells	10384	8.72	680	10510	20.5	1576
3μM ZX1 - 24 HPI	GFP Pos. cells	10375	7.69	570	10415	20.8	1768
1μM TPA - 10 HPI	GFP Pos. cells	10560	3.76	150	10341	12.1	508
1μM TPA - 18 HPI	GFP Pos. cells	10422	3.75	5.4	10391	6.9	31.6
1μM TPA - 24 HPI	GFP Pos. cells	10404	2.65	0.2	10328	6.79	1.1
DMSO - 10 HPI	GFP Pos. cells	8085	4.22	106	8938	12.3	668
DMSO - 18 HPI	GFP Pos. cells	8970	6.84	122.2	9042	14.7	772
DMSO - 24 HPI	GFP Pos. cells	8887	3.14	128	8928	9.84	304
200 nM ISRIB - 10 HPI	GFP Pos. cells	10299	3.83	148	10183	16.9	908
200 nM ISRIB - 18 HPI	GFP Pos. cells	10312	6.52	105.2	10260	14	670
200 nM ISRIB - 24 HPI	GFP Pos. cells	10397	4.93	140	10371	16.6	476
600 nM ISRIB - 10 HPI	GFP Pos. cells	9506	4.25	138	8757	7.6	352
600 nM ISRIB - 18 HPI	GFP Pos. cells	8459	3.31	82.4	8749	10.6	476
600 nM ISRIB - 24 HPI	GFP Pos. cells	8859	2.83	86			

Table 4.2 GFP positive population characteristics from flow cytometry.
GFP positive population characteristics from flow cytometry of each treatment condition at each MOI for each time point as well as each CFU/well. Percent of GFP positive cells seems to track with CFUs. Both the percent of GFP positive cells and CFU for MOI 30 are roughly 3 times as high as MOI 10. Values for CFU/well and for GFP positive frequency from this table are plotted in Figure 4.8.

The effect of 200 nM ISRIB treatment on bacterial burden falls very close to DMSO for MOI 10 at 10 and 18 hours post infection (Figure 4.8C). At 24 hours post infection, 200 nM ISRIB treatment has the highest bacterial burden of both MOI 10 and MOI 30 (Figure 4.8C & D). The effect of 200 nM ISRIB treatment contrasts with that of 30 μM Zn^{2+} treatment. Both treatments increase the rate of intracellular *Salmonella* replication, but ISRIB does not reduce the overall bacterial burden as does Zn^{2+} treatment, which suggests that there is a reduction to the rate at which macrophages can kill intracellular bacteria when cells are treated with ISRIB. This may be due to the impact of the integrated stress response on the upregulation of important stress related genes. If 200 nM ISRIB is delaying the induction of stress response genes which are required for bacterial clearance that could

explain the increase in bacterial load at later timepoints of infection. The 600 nM ISRIB treatment seems to have the opposite effect on bacterial load and replication of intracellular *Salmonella* compared to the 200 nM ISRIB treatment. 600 nM treatment shows a decreased Salmonella burden at 18 and 24 hours for MOI 10 (Figure 4.8C) and at 10 and 18 hours for MOI 30 (Figure 4.8D). If 600 nM ISRIB is capable of inhibiting the formation of the eIF2B holoenzyme complex, as mentioned earlier, then this would have the paradoxical effect of global translation arrest in the absence of phosphorylated eIF2α, leading to an increase in the rate and magnitude of the integrated stress response, which would lead to greater bacterial killing.

4.9 Changes to Select Zinc Regulatory and ER Stress Genes in Infected BMDMs Grown in Altered Zn^{2+} Conditions

We measured Zip14, MT2, Znt4, and spliced Xbp1 mRNA expression with RT-qPCR to quantify the relative changes in those genes over the course of *Salmonella* infection with the Zn^{2+} treatments used in the fluorescence dilution assay (Figure 4.9). mRNA levels at 0 hours post infection are from BMDMs that have been treated with their respective Zn^{2+} conditions for 21 hours. M0 cells are resting BMDMs grown in normal media and infected with *Salmonella* at the indicated times. All samples were normalized to the M0 uninfected control. Levels of several of the genes queried could not be measured in the M0 24 hour time point. An increase in Zip14 expression was observed across all conditions throughout the infection, consistent with RNAseq data (Figure 4.9A). Zip14 expression does not seem to be impacted by Zn^{2+} treatment during the infection. 1 μM TPA and chelex treatment in non-infected cells raise Zip14 on their own. MT2 levels are also increased during infection, but their levels are impacted by the Zn^{2+} manipulation (Figure 4.9B). 1μM TPA reduces the amount of MT2 expression compared to all the other conditions, while higher MT2 expression is seen in cells with increased Zn^{2+} levels. These levels of MT2 expression are also consistent with our RNAseq data. ZnT4 mRNA levels increase during infection in the Zn^{2+} treated cells by RT-qPCR but not by RNAseq (Figure 4.9C). ZnT4 expression is higher in the infected Chelex and ZX1 treated cells.

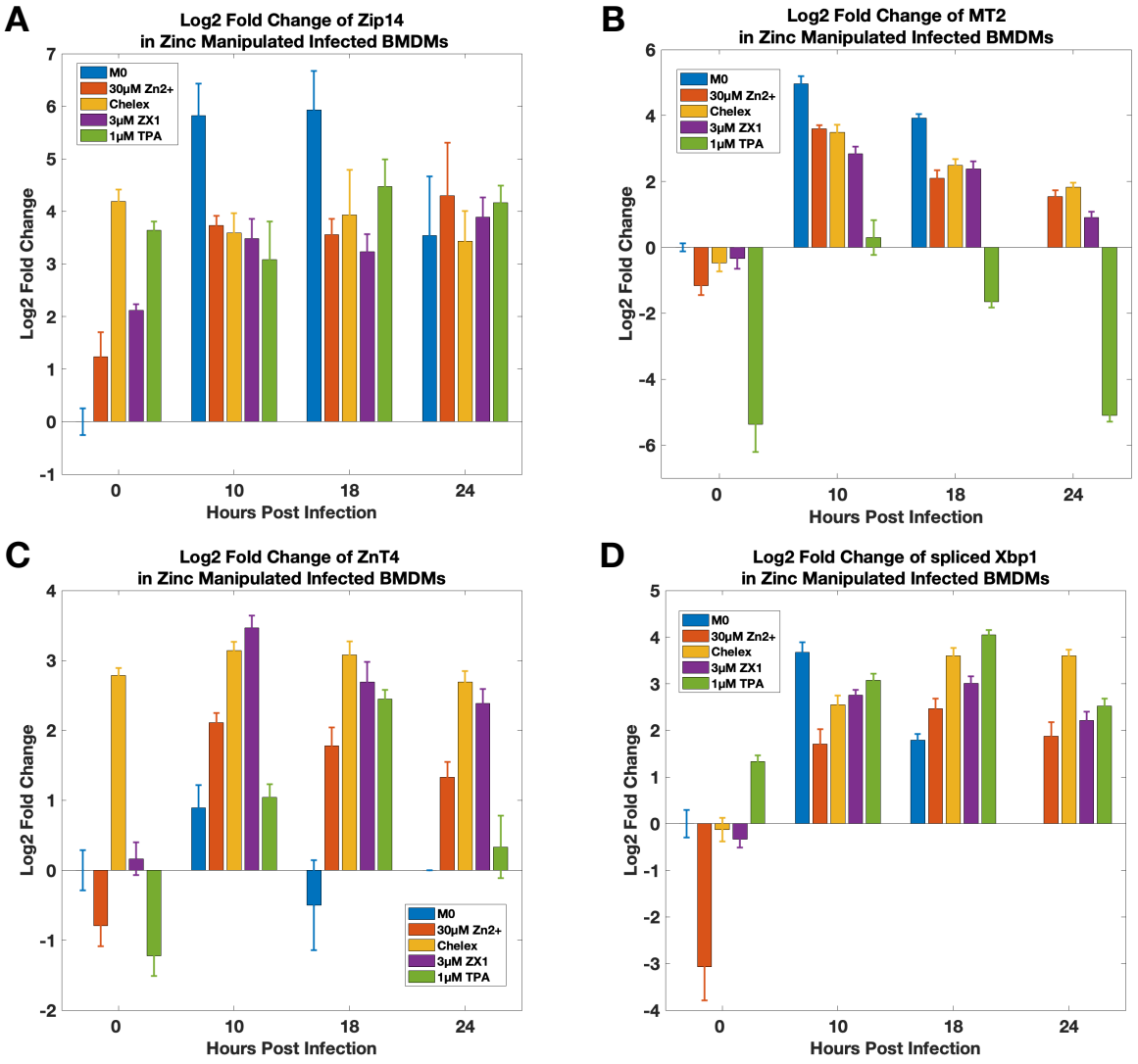

Figure 4.9 Quantification of mRNA changes in *Salmonella*-infected and zinc manipulated BMDMs. Log2 fold change in mRNA of zinc manipulated and infected BMDMs for Zip14 (**A**), MT2 (**B**), ZnT4 (**C**), and spliced Xbp1 (**D**) at each infection timepoint as measured by RT-qPCR. Samples collected at 0 hours post infection are uninfected and treated for 18 hours with their respective zinc condition. M0 cells are untreated and all samples are normalized to the M0 uninfected control. Error bars are +/- standard deviation, n = 3 replicates.

Xbp1 is a transcription factor that is upregulated by Ire1 and the spliced by ATF6α during the unfolded protein response. Splicing of Xbp1 by ATF6α creates an active transcript that is translated into an active transcription factor required to upregulate UPR responsive genes in mammalian cells[239]. Spliced Xbp1 mRNA levels correlate directly with ER stress marker proteins CHOP and BiP[240]. Since

Zip14 is required for hepatocytes to adapt to ER stress[137], we reasoned that Xbp1 splicing would be a good indicator for how Zn^{2+} treatment impacts ER stress in BMDMs in response to infection. Spliced Xbp1 levels increased in all Zn^{2+} manipulations during infection indicating that there is some level of ER stress, but strikingly there is more spliced Xbp1 in cells whose treatments are more zinc deplete (Figure 4.9D). Additionally, 30 μM Zn^{2+} treatment in uninfected BMDMs reduced the amount of Xbp1 splicing from baseline. This suggests that Zn^{2+} is helpful to the host cells undergoing ER stress and may help explain how cells treated with 30 μM Zn^{2+} were more effective at clearing intracellular *Salmonella*.

4.10 Changes to Select Zinc Regulatory or ER Stress Genes in Tunicamycin Treated BMDMs or Infected BMDMs Treated with ISRIB

ISRIB is capable of reversing the effect of translational arrest by modest levels of phospho-eIF2α[233] and as a result can block the transcription of integrated stress response genes including ATF4[237,241]. If ISRIB could block ATF4, we reasoned that it could reduce Zip14 levels, and potentially reduce the cytosolic labile zinc increase that occurs in infection. In order to determine the extent to which 200 nM ISRIB treatment impacted zinc homeostasis and ER stress in infected BMDMs we measured Zip14, MT2, ZnT4 and spliced Xbp1 mRNA levels over the course of an infection with *Salmonella* (Figure 4.10). Tunicamycin treatment of uninfected BMDMs was used as a positive control for ER stress. We found that Zip14 mRNA expression increased with tunicamycin treatment, demonstrating that Zip14 expression increases with ER stress as seen in hepatocytes[137]. Zip14 expression was also increased in infected BMDMs treated with ISRIB or DMSO (Figure 4.10A), One possible explanation for this observation is that the amount of phospho-eIF2α levels within infected cells is higher than the critical threshold that ISRIB can effectively antagonize. ISRIB was shown to restore translation and inhibit stress granule formation during arsenite administration but only up to 50 μM[233]. ISRIB also does not inhibit virus induced integrated stress response activity late in infection.[233] So ISRIB is incapable of preventing an increase in Zip14 expression at the timepoints we measured. The Xbp1 mRNA level increased upon tunicamycin treatment, as expected. It was also high during infection for

ISRIB and DMSO treatment (Figure 4.10D). This is not unexpected as Xbp1 Splicing is a result of the action of Ire1 and ATF6α and not phospho-eIF2α or ATF4. MT2 expression in tunicamycin treatment did not rise to the levels seen in infected cells. MT2 levels are much higher in the infected cells at all timepoints and treatments (Figure 4.10B). ZnT4 levels are also elevated in infection and in tunicamycin treatment (Figure 4.10C).

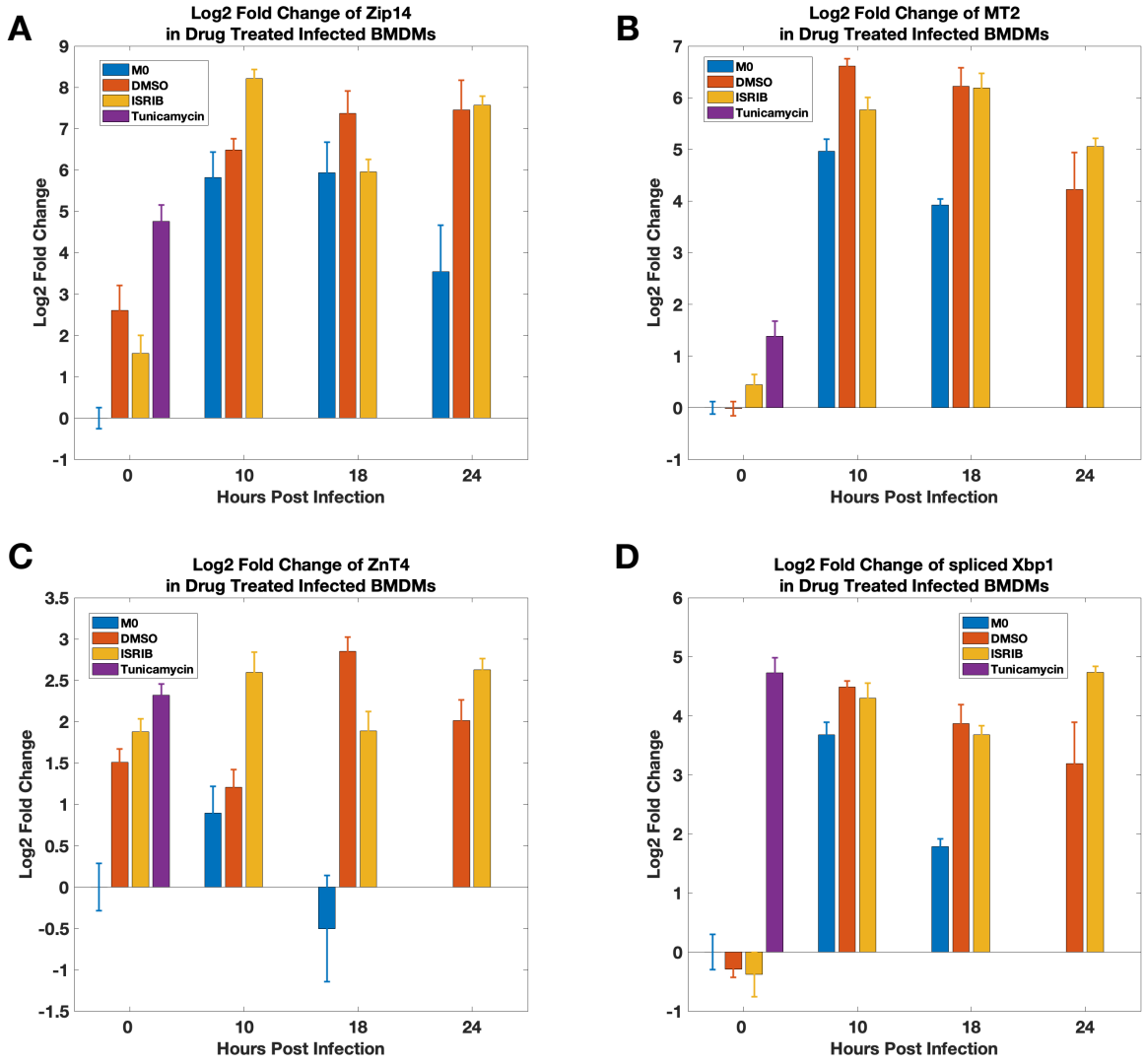

Figure 4.10 Quantification of mRNA changes in drug manipulated BMDMs.
Log2 fold change in mRNA of tunicamycin-treated or ISRIB-treated and infected BMDMs for Zip14 (**A**), MT2 (**B**), ZnT4 (**C**), and spliced Xbp1 (**D**) at each infection timepoint as measured by RT-qPCR. Samples collected at 0 hours post infection are uninfected and treated for 18 hours with their respective treatment. M0 cells are untreated and all samples are normalized to the M0 uninfected control. Error bars are +/- standard deviation, n = 3 replicates.

4.11 Changes to Cytosolic Labile Zn^{2+} in ISRIB Treated and Infected BMDMs

ER stress is implicated in the upregulation of Zip14 in hepatocytes and is regulated by the activation of ATF4 and ATF6α, products of the UPR[137]. To investigate potential labile Zn^{2+} changes upon ISRIB treatment or tunicamycin treatment in BMDMs, we measured the cytosolic labile Zn^{2+} pool in BMDMs expressing NES-ZapCV2 and treated with tunicamycin or infected with WT *Salmonella* expressing mRuby3 and treated with 200 nM ISRIB as was done for the fluorescence dilution and RT-qPCR experiments (Figure 4.11).

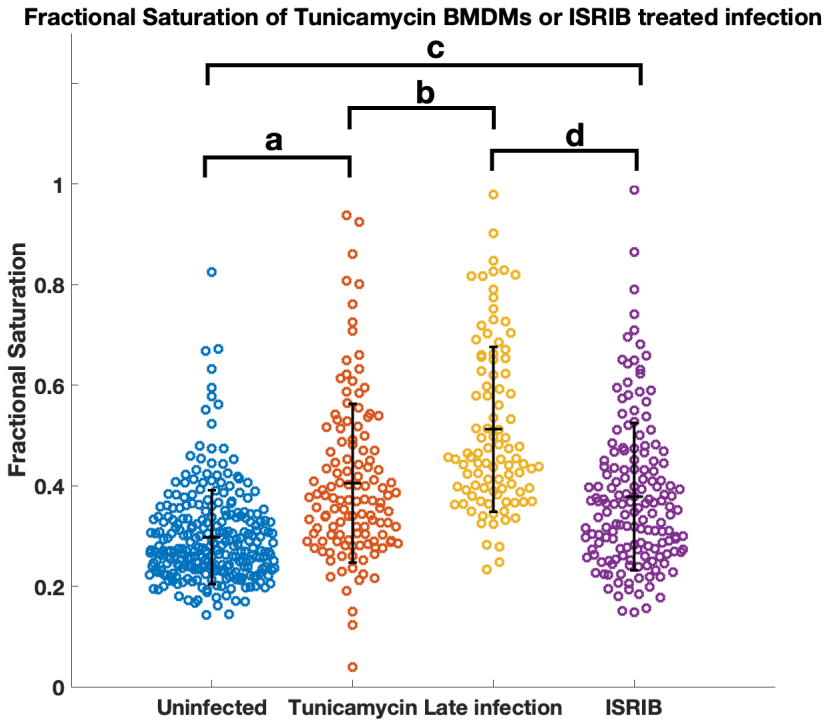

Figure 4.11 Quantification of labile cytosolic zinc in drug manipulated BMDMs
Fractional saturation of NES-ZapCV2 in uninfected tunicamycin-treated BMDMs (FS = 0.40, n = 126 cells) and infected ISRIB-treated BMDMs (FS = 0.38, n = 159 cells) compared to uninfected (FS of 0.30, n = 267 cells) and late-stage infected BMDMs (FS of 0.51, n = 99 cells). 5 µg/ml tunicamycin was added to uninfected BMDMs expressing NES-ZapCV2 for 15 - 18 hours. 200 nM ISRIB was added to infected BMDMS at 2 hours post infection, and dishes were measured between 18 and 21 hours post infection. Tunicamycin treatment raises the fractional saturation of the sensor compared to resting BMDMs (a, p = 8.10e-16), but not quite to the level of BMDMs that are infected for 12-24 hours (b, p = 1.56e-06). 200 nM ISRIB treatment was added to BMDMs expressing NES-ZapCV2 at 2 hours post infection and imaged between 18 and 21 hours post infection. ISRIB treatment reduces the fractional saturation from the late-stage infection group (d, p = 9.20e-11), but not quite to the level of uninfected cells (c, p = 1.59e-11).

18 hours of tunicamycin treatment raised cytosolic Zn^{2+} levels above the resting cell population, but not to the level of late-stage infected cells. Infected BMDMs treated with ISRIB were calibrated between 18 and 21 hours post infection to see whether ISRIB could lower cytosolic labile Zn^{2+} in infected cells. Indeed, ISRIB treated cells do not have as high of a cytosolic labile Zn^{2+} pool as late infected cells, but ISRIB treatment did not reduce labile zinc to the level of resting BMDMs. ISRIB treatment was unable to reduce Zip14 levels during infection as measured by RT-qPCR and was also

unable reduce Xbp1 splicing. Since the Zip14 promoter has binding sites for both ATF4 and ATF6α it may be possible that transcription of Zip14 can occur in the presence of either transcription factor.

4.12 Discussion

The importance of nutritional Zn^{2+} in the host pathogen interface is demonstrated by the mammalian host response to pathogenic insults. In the inflamed gut, neutrophils inhibit the growth of bacteria through the production of extracellular traps that bind zinc and manganese in addition to the robust production of reactive oxygen species and peroxide[58,71]. *Salmonella* thrives in the inflamed gut through the expression of a high affinity Zn^{2+} transporter, ZnuABC, and knockdown of this transporter severely attenuates systemic infection[58]. The role of zinc is also important in the innate immune system. Macrophages are the interface of a systemic infection for many intracellular pathogens including *Salmonella*[13–15,65]. Macrophages have been shown to poison some intracellular pathogens with zinc[63,64] while withholding zinc from other pathogens to cause starvation[61,62], with both mechanisms being important for clearance of the intracellular pathogen. Macrophage accumulate zinc from the extracellular milieu during activation and in infection through upregulation of Zip transporters[61,62,133] and intracellular zinc can act as a negative feedback regulator of NF-κB[123,133] and has the potential to impact infection outcome by reducing the expression of proinflammatory genes[123]. The role of Zn^{2+} in *Salmonella*-infected macrophages has been investigated previously[62,123] using RAW264.7 cells and primary macrophage cells from immune compromised mice[123] or human monocyte derived macrophage and the THP-1 human monocyte cell line[62]. As mentioned above, the immortalized macrophage-like cell line, RAW264.7, differs significantly from primary immune competent BMDMs in their infection phenotype due to differences in proteomics and phagosome maturation[182] and in their susceptibility to infection and intracellular *Salmonella* replication dynmics[75,183,184]. RAW264.7 cells lack a functional NRAMP-1 and are unable to counteract the *Salmonella*-dependent mechanism that remodels the SCV and blocks fusion with vesicle traffic that contain bactericidal agents[183], which may include zinc containing vesicles. Macrophage-like cell lines have also been found to be unable to recapitulate the speed and magnitude of an antimicrobial response during early phase activation[185] and the surface receptor phenotype degrades with

continuous culture[186]. Due to the differences in macrophage cell line infection model phenotypes we sought to utilize a macrophage model that is immune competent and better able to recapitulate a systemic model of infection[65].

We characterized the labile cytosolic Zn^{2+} pool, the changes in zinc regulatory genes, the intracellular *Salmonella* replication and total bacterial load in primary BMDMs from immune competent 129SV mice infected with WT *Salmonella* Typhimurium across a 24-hour infection and compared the effects of nutritional Zn^{2+} manipulations and drug treatments on those parameters. Prior studies that have examined the role of Zn^{2+} on *Salmonella* infection in a macrophage model[62,123] used supraphysiological concentrations of extracellular Zn^{2+} (100 μM – 200 μM) which are far outside of the range of what a macrophage would experience inside the body. Typical serum Zn^{2+} concentrations range from 10 – 30 μM[81,217,218] so we used a Zn^{2+} level that would mimic those concentrations. Serum Zn^{2+} is reduced in systemic infections due to an upregulation of Zip14 in the liver and other vital organs[135,140,213]. To mimic an acute Zn^{2+} deficiency model we chose to reduce Zn^{2+} in the cell culture serum with chelex treatment in place of the more commonly used cell permeable chemical chelation methods. 30 μM Zn^{2+} added back to media with chelex treated serum increases intracellular *Salmonella* replication in BMDMs while at the same time reduces the total bacterial burden compared to BMDMs cultured with chelex treated serum or with 3 μM ZX1 added. Spliced Xbp1 levels are lower throughout infection in 30 μM Zn^{2+} treatment than in serum Zn^{2+} restricted BMDMs suggesting nutritional Zn^{2+} may help the host cell resist ER stress in the context of infection. This may be due negative feedback that occurs from Zn^{2+} on NF-κB as seen previously[123,133].

We wanted to discern whether the increase in cytosolic Zn^{2+} was due to the action of Zip14. We attempted to knockdown Zip14 using shRNA and siRNA but both methods were unsuccessful. Both scramble siRNA and knockdown siRNA increased Zip14 levels as measured by RT-qPCR and also cytosolic labile Zn^{2+} in our BMDMs. This could be due to activation of the PKR in response to dsRNA. Regulation of Zip14 has been reported to be dependent on ATF4[137], so we used ISRIB, the small molecule therapeutic that rescues global translational arrest and reduces ATF4 production, to test whether Zip14 production could be reduced during infection. We did not see a reduction in Zip14

expression in ISRIB treated and infected BMDMs at the timepoints measured, possibly due to the limited magnitude of stress that it is capable of reversing. Xbp1 splicing is not appreciably reduced in ISRIB treatment either, suggesting that ATF6α activity is behaving as normal. ISRIB treatment of infected BMDMs did reduce the cytosolic labile Zn^{2+} increase at late stages of infection which may suggest that Zip14 expression alone is not the only driver of the labile Zn^{2+} increase. In our RNAseq analysis we also discovered that Zip4 is upregulated at 18 hours post infection in conjunction with Zip14, but we did not follow up with measuring Zip4 expression under nutritional Zn^{2+} manipulations and drug treatments.

Interestingly, we saw an increase in intracellular *Salmonella* replication and also an increased bacterial load in 200 nM ISRIB treated BMDMs and the trend was reversed with 600 nM ISRIB treatment. Based on the RT-qPCR analysis, we don't have substantial evidence for ISRIB efficacy after 10 hours of infection. This reason for this may be that, as mentioned earlier, ISRIB is only capable of rescuing only a moderate amount of stress and its effectiveness diminishes as phospho-eIF2α levels rise above a critical threshold regardless of the eIF2α kinase[233]. Rabouw et al. showed that ISRIB was not capable of suppressing translational arrest in cells infected with a recombinant picornovirus beyond 4 hours post infection[233]. Additionally, ISRIB has a very narrow therapeutic concentration. Within the appropriate therapeutic window ISRIB treatment serves to stabilize eIF2B holoenzyme stability and rescue translation initiation, essentially acting to delay the rate and magnitude of the integrated stress response. Above the therapeutic window, ISRIB treatment serves to block eIF2B holoenzyme stability even in the absence of phospho-eIF2α which would initiate the integrated stress response and possibly increase its magnitude. This may explain why, in our hands, 600 nM ISRIB and the DMSO condition have similar replication rates but 600 nm ISRIB showed a reduced bacterial burden for both MOI 10 and MOI 30 at the timepoints measured. If ISRIB treatment is only efficacious at the early stages of infection then the speed and magnitude of the integrated stress response may be impacted and could be important for the control intracellular bacterial replication and clearance. It will be a priority to confirm ISRIB effectiveness at early stages of the infection and

to investigate the role of the integrated stress response on the bacterial clearance mechanisms such as the early respiratory burst and the inducible reactive nitrogen species generation within our model.

Since ER stress induction of ATF4 and ATF6α has been implicated in the regulation of Zip14 in hepatocytes[137], we sought to verify that this regulation pattern occurs in BMDMs and test to what extent ER stress is responsible for the cytosolic labile Zn^{2+} increase. We treated BMDMs with 5 μg/ml tunicamycin for 18 hours to cause ER stress and then measured Zip14, MT2 and spliced Xbp1 mRNA levels along with cytosolic labile Zn^{2+}. Cytosolic labile Zn^{2+} levels, Zip14 expression and MT2 expression increased in tunicamycin treated BMDMs, indicating that indeed ER stress can alter zinc homeostasis in BMDMs, similar to what has been observed in hepatocytes[137]. However, the increases upon tunicamycin treatment were not as high as what was observed in infection. Together these data suggest that ER stress is likely not the only driver of cytosolic labile Zn^{2+} levels during infection. One component that tunicamycin treatment is lacking is the respiratory burst and inducible nitric oxide synthase generating ROS and RNS. It is possible that treatment with a mild oxidative agent, such as peroxide, in conjunction with tunicamycin treatment could raise the cytosolic Zn^{2+} pool to the levels seen during infection due to release from oxidized cysteines MTs.

We successfully demonstrate that nutritional Zn^{2+} adequacy improves the outcome of the infection for the host cell, but we have yet to address if this improvement is due to changes in the labile Zn^{2+} pool or by some other means. Wu et al. demonstrate that in *Salmonella*-infected RAW264.7 cells supplemented with 100 μM Zn^{2+} there was no change to internalized bacterial replication or clearance, but instead the vulnerability of the host cell to infection increased due to inhibition of NF-κB[123]. Kapetanovic et al., on the other hand show that primary human macrophages supplemented with 100 μM Zn^{2+} are better at clearing *Salmonella*[62] which is in agreement with what we see in our study. Perhaps the difference in these observations applies primarily to immune-compromised cells since macrophages lacking a functional Nramp1 are not able to prevent Salmonella from blocking vesicle fusion with the SCV[183]. Importantly, our report is the first to show that moderate nutritional Zn^{2+} perturbations impact the outcome of the infection. We have measured cytosolic labile Zn^{2+} in *Salmonella*-infected BMDMs but we have not demonstrated the extent to which nutritional Zn^{2+}

manipulations impact the labile Zn^{2+} pool. Additionally, we do not know to what extent changes in the labile Zn^{2+} pool are available to *Salmonella* contained in the SCV. In Zip14 knockout mice, injection of $^{65}Zn^{2+}$ in the small intestines labels early endosomes in the basolateral membrane of the duodenum and jejunum because a lack of Zip14 prevents Zn^{2+} from being mobilized, trapping it in the endosomes[89,242]. This demonstrates that in addition to transport at the plasma membrane, nutritional Zn^{2+} is absorbed into early endosomes. FluoZin3-AM staining of infected macrophages shows that high levels of Zn^{2+} are localized in vesicles and lysosomes[62,133]. It is known that *Salmonella* is able to modulate host cell vesicle trafficking[11], and at least one study reports that *Salmonella* uses this strategy to reduce exposure to Zn^{2+} and Cu^{+} containing vesicle to prevent toxicity[62]. It is conceivable therefore that nutritional Zn^{2+} accumulation throughout the infection may be available to intracellular *Salmonella* by coopted vesicle traffic fusing with the SCV, although acquisition from the cytosolic labile Zn^{2+} pool is not ruled out. It is clear that both nutritional Zn^{2+} adequacy and cytosolic labile Zn^{2+} are playing an important role in host cell defense.

4.13 Future Directions

One of the questions we set out to answer is whether the intracellular cytosolic zinc increase we see in our cells during infection was due to the expression of Zip14. Genetic manipulation of primary macrophages has been, in the past, extraordinarily difficult to carry out. When nucleofection technology enabled us to transiently transfect BMDMs, we attempted to use two classical methods of gene knockdown, siRNA and shRNA, to target Zip14 mRNA and reduce its expression. Both attempts were unsuccessful, we suppose, due to activation of the PKR dsRNA detection pathway which leads to cell activation of the pathway that contributes to Zip14 expression. Measurement of Zip14 levels in both the scramble and the targeted shRNA or siRNA showed that Zip14 expression increased. Importantly, transfection of a non shRNA plasmid did not increase Zip14 mRNA levels, indicating that this effect was not due to the act of transfection. We also tried using a pharmacological inhibitor of the integrated stress response, ISRIB, to try to reduce Zip14 expression, which did not seem to have therapeutic efficacy within the window of infection that we measured. At the time of this writing, the role of Zip14 in our system is still unknown.

Without the ability to knockdown Zip14 expression, we are limited in the certainty that Zip14 is the major contributor to the zinc uptake phenotype. We will address this problem by measuring the contribution of other Zip transporters that may contribute to our phenotype. Two studies have reported an increase in a Zip transporter, Zip2[61] and Zip8[133], where a similar phenotype to ours is measured. In our RNAseq data we see virtually no expression of Zip2 and a downregulation of Zip8. Both of those need to be verified by RT-qPCR. An ideal way to measure the effect of Zip14 in BMDMs would be to isolate primary macrophages from a Zip14 knockout mouse. The Zip14 knockout mouse is available, and it is available with the same immune competent genetic background as the mice used in our study, 129SV. To our knowledge, no one has carried out systemic infection studies in primary cells or in the whole animal of Zip14 (-/-) mice using a specific intracellular pathogen such as *Salmonella Typhimurium* or *Mycobacterium tuberculosis*.

Now that we are capable of transient transfection of primary BMDMs, a study of the intracellular cytosolic labile zinc pool within Zip14(-/-) BMDMs would give us a better understanding of the accessibility of the labile zinc pool to intracellular pathogens contained within a vacuole. Use of a genetically encoded zinc sensor gives us a more targeted and accurate readout f the labile zinc pool than cell permeable dyes both because the targeting of the sensor is more controlled and the sensitivity of the sensor is greater[227]. Zip14 (-/-) mice exhibit an increase in endosomal zinc within the duodenum and jejunum, suggesting that Zip14 contributes to the release of into the cytosol from endosomal compartments within those cells[89]. If zinc sequestration occurs in the same way inside of macrophages, then the cytosolic zinc pool should be similarly affected, with lower zinc than WT and a shift in intracellular zinc storage with more accumulation occurring in endosomal vesicles and less making it into the cytosol. This would provide a way to test the mechanism of zinc delivery to pathogens who are poisoned by zinc. If zinc poisoning inside of macrophages occurs by fusion of endosomal traffic, which is high in zinc, with the pathogen containing vacuole, then the Zip14 (-/-) macrophages should be better at killing these types of intracellular pathogens because their endosomes should have a higher amount of zinc than WT. If, on the other hand, zinc is pumped into pathogen containing vacuoles through the concerted action of ZnT transporters then this process should remain unaffected

in Zip14(-/-) macrophages, as long as ZnT expression and trafficking, which may be impacted by zinc status of the cell, is controlled for.

A logical extension of our work would be to test the extent of replication and killing within mice infected either orally or intraperitoneally with *Salmonella*. The effect of nutritional zinc status on infection outcome would be greatly enhanced by direct comparison of infection outcome measures in infected mice of both WT and Zip14 (-/-) genetic backgrounds, and would provide insight into the specific nature of the action this zinc transporter has on the ability of the host to control pathogen growth. Three studies have attempted to measure the effect of zinc chelation and supplementation on the production of ROS in infected macrophages and conclude that the intracellular zinc increase serves to inhibit ROS production[61,62,123]. Since those studies carried out those measurements using chemical chelation and supraphysiological concentrations of zinc to reach those conclusions, it would be beneficial to measure the extent of ROS production in macrophages isolated from infected mice of both WT and Zip14 (-/-) genetic backgrounds. This could be accomplished using flow cytometry to measure the ROS of isolated macrophages with a fluorogenic ROS indicator, and using a fluorescence dilution strain to measure the replication rate and rate of occurrence of intracellular pathogens, simultaneously. This would provide a better indication of the effects of zinc status and zinc handling capacity on ROS production. Paired with the infection outcome measures of killing and replication of the intracellular pathogen, this would provide the most in-depth insight into how intracellular zinc homeostasis and zinc status shape the host-pathogen interface.

One of the remaining questions from our study is the extent to which labile cytosolic zinc drives the control of bacterial replication and clearance in infection. The intracellular zinc rise during infection is followed with an increase in metallothionein expression which increases the buffering capacity of cells for zinc. Since we were unable reduce intracellular zinc by reducing Zip14 expression, another method we could try would be to overexpress metallothionein within macrophages to attempt to reduce the availability of zinc. First, it would have to be determined that metallothionein overexpression could reduce the labile zinc pool. Since the binding affinity, and thus the buffering capacity, of metallothionein is intrinsically tied to its redox state, this may not work during infection

where there is large shift in the redox state of the cell. If a reduction of labile zinc is achieved, however, the next step would be to measure the impact this has on the replication of the intracellular bacteria and also the production of ROS and RNS during infection. If ROS and RNS production remain the same this could help us to resolve the extent to which cytosolic zinc interacts with pathogens inside their vacuole. Since metallothionein is expressed in the cytosol, this would provide a targeted method for manipulating only the cytosolic zinc pool while leaving alone zinc pools within different organelles.

Chapter 5

Experimental Methods and Protocols

5.1 Publication Status and Author Contributions

Young, A.M., Minson, M., McQuate, S.E., Palmer, A.E., "Optimized Fluorescence Complementation Platform for Visualizing *Salmonella* Effector Proteins Reveals Distinctly Different Intracellular Niches in Different Cell Types" *ACS Infectious Diseases*, 2017

A.M.Y. designed the experiments, A.M.Y., M.M., S.E.M. carried out the research, A.M.Y., A.E.P., S.E.M., and M.M. wrote the manuscript.

Batan, D., Braselmann, E., Minson, M., Nguyen Thanh, D.M., Cossart, P., Palmer, A.E., "A Multicolor Split-Fluorescent Protein Approach to Visualize *Listeria* Protein Secretion in Infection" *Biophysical Journal,* 2018

D.B., E.B., A.E.P. designed research; D.B., E.B., M.M., D.M.T.N. performed research; D.B., E.B., M.M., D.M.T.N. analyzed data; P.C. contributed reagents and experimental advice; D.B., E.B., A.E.P. wrote the manuscript.

Minson, M., Janisziewski, L. Palmer, A.E., "Zinc Adequacy Improves Clearance of *Salmonella* in Infected Immune Competent Primary Macrophages" Unpublished, 2019

5.2 Bacterial Strains and Culture Conditions

5.2.1 Salmonella

All *Salmonella* strains were isogenic derivatives of *Salmonella enterica* serovar Typhimurium SL1344. *Salmonella* effector gene deletion strains (*ΔsteA, ΔsseF, ΔsseG, ΔslrP, ΔsopA, ΔsteB, ΔgtgE*) and chromosomal integration of the GFP11 or 3XGFP11 were generated as described previously[17,243] using λ red recombination. Fluorescent strains for live cell imaging studies constitutively expressed mRuby3 from a plasmid (parent pACYC177) under the *rpsM* ribosomal gene promoter (see Figure 2.1). The fluorescence dilution strain WT SL1344 expressing the plasmid pDiGc encodes for a fluorescent-optimized DsRed protein whose expression is under the control of the arabinose-inducible P_{BAD} promoter and EGFP under the control of a constitutive promoter (*rpsM*) was used as previously described[184,230,231] and was a generous gift from Corrie Detweiler. *Salmonella* strains and plasmids are listed in Table 5.1. To generate growth curves, *Salmonella* strains were grown with aeration at 37°C to saturation in LB (EMD) media supplemented with antibiotics as required. Cultures were then diluted 1:100 into fresh LB (EMD) media supplemented with appropriate antibiotics and the OD_{600} was measured every 30 minutes for a duration of 16 hours using a Tecan Safire II monochromator-based plate reader.

For infection of HeLa cells, *Salmonella* strains were grown in LB (EMD) supplemented with 300 mM NaCl (Fisher Scientific) and 25 mM MOPS (Sigma) at pH 7.6 and appropriate antibiotics at 37°C for 16 hours without aeration. Prior to infection, bacteria were diluted 1:33 in 3 ml of SPI-1 media, with appropriate antibiotics for 4 hours at 37 °C without aeration. For infection of primary BMDMs, *Salmonella* strains were grown to stationary phase in LB, with appropriate antibiotics at 37 °C with aeration. Prior to infection of BMDMs, bacteria were opsonized in a 1:1 solution of mouse serum (Sigma) and cell culture media (Gibco) for 30 min at 37 °C, pelleted at 13,000 X g for 1 min and resuspended in PBS prior to inoculation.

For SPI-2 induction, *Salmonella* strains were grown in defined media consisting of 5 mM KCl, 7.5 mM $(NH_4)_2SO_4$, 38 mM glycerol (0.3% v/v), 0.1% casamino acids, 0.5 mM K_2SO_4, 8 µM $MgCl_2$, 337 µM PO_4^{-3} (K_3PO_4), 80 mM MES, pH 6.5 with aeration. The pH conditions for SPI-2 induction are often 5.4,

however we modified these growth conditions to pH 6.5 for simultaneous expression of SPI-2 and split-GFP recombination during the bacterial expression assay. For the bacterial expression assay, cultures were grown to early stationary phase.

	Plasmid Name	Vector backbone	Resistance	FP(s)	Notes
	pTruncated SteA Promoter-SlrP-GFP11_mRuby3_ACYC	mRuby3-ACYC177	Amp	mRuby3	for split GFP tagging under steA promoter (Has EcoRI as the RBS spacer)
	pTruncated SteA Promoter-SseG-GFP11_mRuby3_ACYC	mRuby3-ACYC177	Amp	mRuby3	for split GFP tagging under steA promoter (Has EcoRI as the RBS spacer)
	pTruncated SteA Promoter-SseF-GFP11_mRuby3_ACYC	mRuby3-ACYC177	Amp	mRuby3	for split GFP tagging under steA promoter (Has EcoRI as the RBS spacer)
	pTruncated PipB2 Promoter-PipB2-GFP11_mRuby3_ACY	mRuby3-ACYC177	Amp	mRuby3	for split GFP tagging under steA promoter (Has EcoRI as the RBS spacer)
	pTruncated SteA Promoter-SteA-GFP11_mRuby3_ACYC	mRuby3-ACYC177	Amp	mRuby3	for split GFP tagging under steA promoter (Has EcoRI as the RBS spacer)
	pPipB2 Promoter-PipB2-SNAP_mCherry_ACYC	mCherry-ACYC177	Amp	mCherry	For SNAP-tag secretion assay
	pPipB2 Promoter-PipB2-3XFLAG_mCherry_ACYC	mCherry-ACYC178	Amp	mCherry	For SNAP-tag secretion assay = Positive control
	GFP1-10mamopt (mammalian optimized)	pCMV-Hyg-Amp	Amp	GFP1-10	For split GFP tagging
	GFP1-10_IRES_NLS-mtagBFP2	pMAX	Kan	NLS-BFP	For nucleofecting Macrophage
	Piggy Bac GFP1-10_IRES_NLS-BFP_pA	Piggy Bac	Amp	NLS-BFP	For making GFP1-10 Stable. Contains pA signal
	GFP11-ERK1 (mammalian optimized)	pCMV-Hyg-Amp	Amp	GFP11-Erk1	Co-transfect to test split GFP complementation = positive control
	GFP1-10bacopt (Bacteria optimized in pBAD18 CmR	pBAD18	Cmr	GFP1-10	Bacterial expression of GFP1-10
	pDiGc (DsRed-inducible_GFP_constitutive)	pBAD	Amp	DsRed + GFP	Fluorescence dilution plasmid. Arabinose inducible dsRed
Strain	**Construct Name**	**Vector backbone**	**Resistance**	**FP(s)**	**Genotype**
SI1344	GFP1-10 in pBAD18 CmR + pAYCY-mRuby3	pBAD18 + pACYC177	StreP/Amp/Cmr	GFP1-10 + mRuby3	WT
	pDiGC (DsRed-inducible_GFP_constitutive)	pBAD	StreP/Amp	DsRed + GFP	WT
	pTruncated SteA Promoter-PipB2-GFP11_mRuby3_ACYC	pmRuby3_ACYC	Strep/Amp/Kan	mRuby3	ΔPipB2 SL1344
	pTruncated SteA Promoter-SlrP-GFP11_mRuby3_ACYC	pmRuby3_ACYC	Strep/Amp/Kan	mRuby3	ΔSlrP SL1344
	pTruncated SteA Promoter-SseG-GFP11_mRuby3_ACYC	pmRuby3_ACYC	Strep/Amp/Kan	mRuby3	ΔSseG SL1344
	pTruncated SteA Promoter-SteA-GFP11_mRuby3_ACYC	pmRuby3_ACYC	Strep/Amp/Kan	mRuby3	ΔSteA SL1344
	SteA-1x-GFP11 knock in + pmRuby3-ACYC	pmRuby3_ACYC	Strep/Amp/Kan	mRuby3	ΔSteA SL1344
	SteA-3x-GFP11 knock in + pmRuby3-ACYC	pmRuby3_ACYC	Strep/Amp/Kan	mRuby3	ΔSteA SL1344
	SseF-1x-GFP11 knock in + pmRuby3-ACYC	pmRuby3_ACYC	Strep/Amp/Kan	mRuby3	ΔSseF SL1344
	SseF-3x-GFP11 knock in + pmRuby3-ACYC	pmRuby3_ACYC	Strep/Amp/Kan	mRuby3	ΔSseF SL1344
	SseG-1x-GFP11 knock in + pmRuby3-ACYC	pmRuby3_ACYC	Strep/Amp/Kan	mRuby3	ΔSseG SL1344
	SseG-3x-GFP11 knock in + pmRuby3-ACYC	pmRuby3_ACYC	Strep/Amp/Kan	mRuby3	ΔSseG SL1344
	SlrP-1x-GFP11 knock in + pmRuby3-ACYC	pmRuby3_ACYC	Strep/Amp/Kan	mRuby3	ΔSlrP SL1344
	SlrP-3x-GFP11 knock in + pmRuby3-ACYC	pmRuby3_ACYC	Strep/Amp/Kan	mRuby3	ΔSlrP SL1344

Table 5.1 Strains and plasmids used for *Salmonella* infections

5.2.2 Listeria

An overview of *Listeria* strains is presented in Table 5.2 (see also Fig. 3.1 b for a schematic). *Listeria* experiments were carried out in *Listeria monocytogenes* EGDe (BUG 1600)[244] or an *inlC* deletion strain (EGDe Δ*inlC*, BUG 2118). *Listeria* strains were grown in Brain Heart Infusion (BHI) media (Fisher Scientific, Waltham, MA) at 37ºC. When required, erythromycin was added at a final concentration of 5 µg/ml for *Listeria* and at a final concentration of 150 µg/ml for *E. coli* (see Table 5.2[S1]). Growth curves of *Listeria* strains were collected as follows. A saturated overnight culture of each strain was diluted to an O.D. at 600 nm of 0.001. Wells of a 96 well plate with clear bottom were filled with 300 µL of each culture in triplicate. Growth of bacterial cultures was monitored via O.D. at 600 nm every 30 min at 30°C for 18 h in a Tecan Safire-II plate reader while leaving the plate shaking.

Strain Name	Resistance	Detailed genotype and source
wt	none	EGD-e wt (BUG 1600) (51)
Δ*inlC*	none	EGD-e Δ*inlC* (Cossart lab collection, BUG 2118)
Δ*inlC* $_{Phyper\text{-}inlC\text{-}GFP11}$	erythromycin	EGD-e Δ*inlC* pAT18_P*hyper_inlC_GFP11* (Batan et al.)
Δ*inlC* $_{pInlC\text{-}inlC\text{-}GFP11}$	erythromycin	EGD-e Δ*inlC* pAT18_*pInlC_inlC_GFP11* (Batan et al.)
Δ*inlC* $_{pInlC\text{-}inlC\text{-}mNG11}$	erythromycin	EGD-e Δ*inlC* pAT18_*pInlC_inlC_mNG11* (Batan et al.)
Δ*inlC* $_{pInlC\text{-}inlC\text{-}sfCh11}$	erythromycin	EGD-e Δ*inlC* pAT18_*pInlC_inlC_sfCh11* (Batan et al.)

Table 5.2 Strains, sources, and resistance markers of *Listeria* used to image *Listeria* effector proteins.

5.2.3 Escherichia coli

Plasmid generation was carried out in *Escherichia coli* (*E. coli*) Stellar cells (Takara Bio USA, Mountain View, CA). *E. coli* strains were grown in Luria-Bertani (LB) broth (Fisher Scientific, Waltham, MA) at 37°C shaking at 180 rpm.

5.3 Cloning

5.3.1 Generalized Labeling Platform of *Salmonella* Effectors

A generalized effector labeling platform was created in pACYC177 using standard cloning methods. A cloning layout is presented in Figure 5.1.

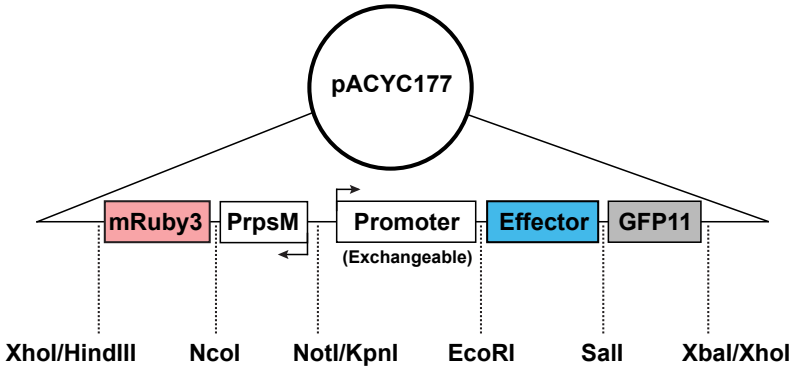

Figure 5.1 Cloning layout of the pACYC plasmid based GFP11 effector protein labeling platform. The plasmid based effector protein-labeling platform with exchangeable promoters, effectors, and tags including a constitutive mRuby bacterial marker was made modular with restriction cloning sites.

5.3.2 GFP1-10 IRES NLS mtagBFP

To create a co-expressing transfection tag for easier identification of transfected cells expressing non-fluorescent GFP1-10, a bicistronic vector encoding for GFP1-10 and a nuclear localized blue fluorescent protein was made. The GFP1-10 sequence was obtained from pGFP1-10$_{mamopt}$. The IRES, from encephalomyocarditis virus (EMCV), was obtained from the pIRES2-EGFP (Clontech, Palo Alto, California). PCR fragments of GFP1-10, the IRES, and the NLS-tagBFP were created with short overlapping regions of homology and joined using overlapping PCR. The long PCR fragment of GFP1-10_IRES_NLS-mTagBFP2 was ligated into PiggyBac Dual Promoter plasmid PB513B-1. The polyA signal was PCR amplified with homology adapters from the downstream SV40 polyA in the PB513B-1 and added to the long PCR fragment of GFP1-10_IRES_NLS-mTagBFP2 and re-ligated into PB513B-1 at the MCS. For easier expression of this construct in primary cells the long PCR fragment of GFP1-10_IRES_NLS-mTagBFP2 was ligated into pMax vector using BamHI and EcoRI restriction sites in the MCS. In this context GFP1-10_IRES_NLS-mTagBFP2 has a polyA signal from the vector backbone, and is driven by the CMV promoter.

5.3.3 FP11 tagging of inlC for expression in *Listeria*

A unique *Xba*I site was introduced upstream of the P*hyper* promoter in pAT18_cGFP[195] by standard site directed mutagenesis techniques. A unique *Sal*I site is located immediately after the GFP stop codon. The region encompassing the P*hyper* promoter and the cGFP coding sequence was removed via *Xba*I and *Sal*I restriction digestion and replaced by inserts encoding for various *inlC* fusions (see Fig. 3.1 b). Variants of the inserts include two different promoters (P*hyper* vs. the *inlC* promoter) and the 11th strand of different fluorescent proteins, namely the 11st strand of GFP (GFP11)[50,245], the 11th strand of mNeonGreen (mNG11)[246] and the 11th strand of super-folder Cherry (sfCh11)[246]. These inserts were purchased as g-block (IDT, San Jose, CA) DNA fragments, including *Xba*I and *Sal*I restriction sites for ligation. Annotated sequences for promoters and the tag sequences are provided in Table 5.3 and 5.4. The DNA and resulting protein coding sequences for the GFP11, mNG11 and sfCh11 tags are shown in Table 5.4. The promoter and coding sequence for *inlC* were retrieved from the National Library of Medicine (US), National Center for Biotechnology Information (NCBI); 2004 – [cited 2019-07-19], available from https://www.ncbi.nlm.nih.gov/gene/. Gene ID: 985945, inlC internalin C [*Listeria monocytogenes* EGD-e]. To ensure optimal expression in *Listeria*, the codon usage for the tags was optimized manually according to codon usage in *Listeria*[247] and verified using the %MinMax codon usage quantification algorithm[248].

P*hyper*   5'**TCTAGA**AGACGAAAGGGCCTAATTTTGCAAAAAGTTGTTGACTTTATCTACAAGGTGTGGC   ATAATGTGTGTCGGCCATAAAGCAAGCATATAATATTGCGTTTCATCTTTAGAAGCGAATTTC   GCCAATATTATAATTATCAAAAGAGAGGGGTGGCAAACGGTATTTGGCATTATTAGGTTAAAA   AATGTAGAAGGAGAGTGAAACCC **ATG TTG**…
p*inlC*   5'**TCTAGA**AGACGAAAGGGCCATTATTAACGCTTGTTAATTTAAACATCTCTTATTTTTGCTAA   CATATAAGTATACAAAGGGACATAAAAAGGTTAACAGCGTTTGTTAAATAGGAAGTATATGAA   AATCCTCTTTTGTGTTTCTAAATTTATTTTTAAGGAGTGGAGACGGTCCGCTAGC **ATG TTG**…

Table 5.3 Sequences of Phyper and pinlC.
The 5' *Xba*I restriction site flanking the *inlC* fusion genes is indicated in bold and underlined and the beginning of the *inlC* coding sequence (ATG TTG…) at the 3' end of the promoters is shown in bold. **Top**: the blue underlined region is the P*hyper* region and the *hly* 5'UTR is shown in yellow and underlined. **Bottom**: the green underlined region corresponds to the *inlC* promoter.

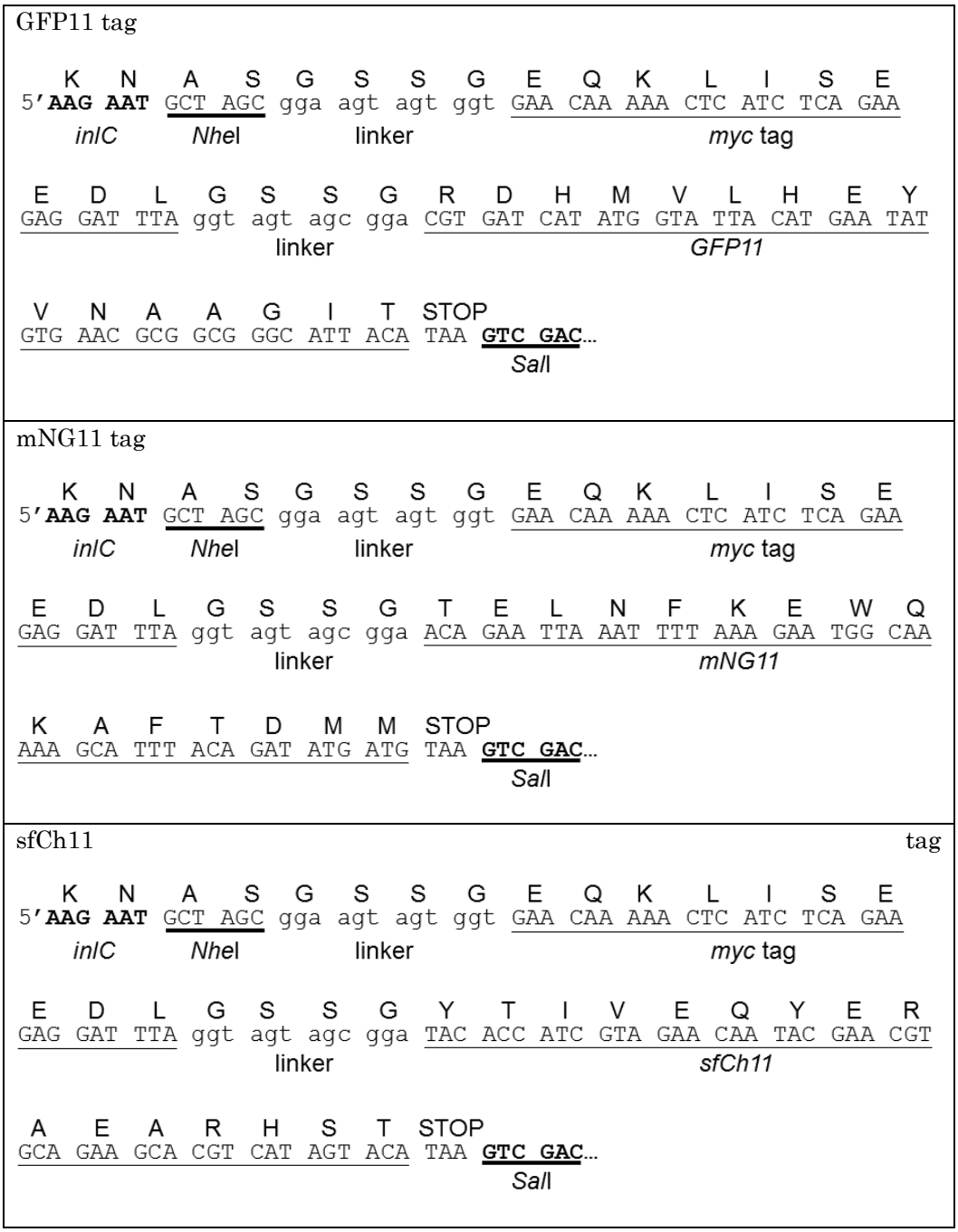

Table 5.4 DNA and protein sequences of split-FP tags at the 3' end of InlC

5.3.4 *Listeria* electroporation

To introduce plasmids into *Listeria* strains, cells were grown for two hours at 37°C and shaking at 180 rpm until an O.D. of 0.2 at 600 nm was reached. Penicillin-G was added to a final concentration of 0.12 μg/mL. The *Listeria* cells were grown for an additional three hours until the final O.D. was

between 0.6 and 0.8 at 600 nm. Cells were harvested by centrifugation for 30 mins at 4,000 rpm and resuspended in cold (4°C) electroporation buffer consisting of 816 mM Sucrose, 1 mM $MgCl_2$ at pH 7. Cells were washed three times using 100 mL, 66 mL and 33 mL electroporation buffer in subsequent steps. All resuspension steps were performed at 4°C. The washed cells were resuspended at a concentration of approximately $1x10^{11}$ cells/mL in electroporation buffer. Aliquots of 100 µL cells were placed in electroporation cuvettes with a 0.2 cm gap (Bio-Rad, Hercules, CA) along with 5 µL plasmid DNA at a concentration of 1 µg/µL. Cells were electroporated at 2.4 kV, 200 Ohms and 25 µF. The cells were immediately transferred in 900 µL pre-warmed BHI media and incubated at 37°C for three hours, followed by plating on selective plates and incubation at 37°C overnight.

For fluorescent protein complementation, a plasmid encoding GFP1-10 and a nuclear BFP marker was used (described above). Plasmids to produce strands 1-10 of mNeonGreen (mNG1-10) and super-folder Cherry (sfCh1-10) were a gift from Bo Huang[246]. The coding sequences of each gene were ligated into pcDNA3.1(+) using standard cloning methods. Protein sequences of GFP1-10, mNG1-10 and sfCh1-10 are listed in Table 5.5.

GFP1-10 MVSKGEELFT GVVPILVELD GDVNGHKFSV RGEGEGDATI GKLTLKFICT TGKLPVPWPT LVTTLTYGVQ CFSRYPDHMK RHDFFKSAMP EGYVQERTIS FKDDGKYKTR AVVKFEGDTL VNRIELKGTD FKEDGNILGH KLEYNFNSHN VYITADKQKN GIKANFTVRH NVEDGSVQLA DHYQQNTPIG DGPVLLPDNH YLSTQTVLSK DPNEK
mNG1-10 MVSKGEEDNM ASLPATHELH IFGSINGVDF DMVGQGTGNP NDGYEELNLK STKGDLQFSP WILVPHIGYG FHQYLPYPDG MSPFQAAMVD GSGYQVHRTM QFEDGASLTV NYRYTYEGSH IKGEAQVMGT GFPADGPVMT NTLTAADWCM SKKTYPNDKT IISTFKWSYT TVNGKRYRST ARTTYTFAKP MAANYLKNQP MYVFRKTELK HSM
sfCh1-10 MEEDNMAIIK EFMRFKVHME GSVNGHEFEI EGEGEGHPYE GTQTAKLKVT KGGPLPFAWD ILSPQFMYGS KAYVKHPADI PDYLKLSFPE GFTWERVMNF EDGGVVTVTQ DSSLQDGQFI YKVKLLGINF PSDGPVMQKK TMGWEASTER MYPEDGALKG EINQRLKLKD GGHYDAEVKT TYKAKKPVQL PGAYNVDIKL DITSHNED

Table 5.5 Protein sequences for fluorescent protein 1-10 (FP1-10) constructs.
Each FP1-10 corresponds to the first 10 ß-strands of the FP; the last and 11th strand represents the other fragment of the split-FP system (Table 5.4).

5.4 Cell Culture and Reagents

5.4.1 HeLa Cell Culture and Transfection

HeLa cells (ATCC CCL-2) were used as model epithelial cells in these studies. Cells were maintained in Dulbecco's modified Eagle's medium (DMEM) (Thermo Fisher Scientific) supplemented with 10% fetal bovine serum (FBS) (Thermo Fisher Scientific). Cells were grown at 37 ^{o}C with 5% CO_2. HeLa cells were passaged every 2–4 days and not used past passage 12. To passage cells, they

were first rinsed with phosphate-buffered saline (PBS) then incubated with trypsin EDTA (Thermo Fisher Scientific) until cells had detached. Trypsin was quenched with DMEM/FBS media and cells were homogenized for counting, and then seeded in new dishes.

For transfections, HeLa cells between a passage number of 2-10 were seeded into 35 mm glass-bottom dishes and allowed to proliferate for 24 hours. Transection of pGFP1-10mamopt was achieved using *Trans*IT-LT1 (Mirus) transfection reagent and conditions recommended by the manufacturer for 3 µg of DNA. Transfected cells were incubated at 37°C with 5% CO_2 for 48 hours prior to imaging. For the creation of a stable cell line expressing GFP1-10_IRES_NLS-mTagBFP2, 1000 ng of PiggyBac-GFP1-10_IRES_NLS-mTagBFP2 was cotransfected with 200 ng of Super PiggyBac Transposase into HeLa cells using *Trans*IT-LT1 (Mirus) and stably expressing cells were selected using puromycin (10 µg/ml) 72 hours post transfection.

5.4.2 Bone Marrow Isolation and Macrophage Differentiation

Primary BMDMs were isolated, as previously described[249]. Bone marrow was flushed with PBS from the femur, tibia, and humerus bones of 8- to 16- week-old SV129S6 mice (Taconic Laboratories, Hudson, NY, USA). Marrow was strained through a 70 µm nylon mesh Falcon™ Cell Strainer (Corning™ 352350) then overlaid onto an equal volume of Histopaque-1083 (Sigma-Aldrich, St. Louis, MO, USA) and centrifuged at 500g for 25 min and allowed to spin down with no brake. Monocytes at the interface were washed 2X with PBS then suspended in DMEM (Sigma-Aldrich, St. Louis, MO, USA) supplemented with FBS (20%), L-glutamine (2 mM), sodium pyruvate (1 mM), beta-mercaptoethanol (50 µM), HEPES (10 mM) and penicillin-streptomycin (50 IU/ml of penicillin and 50 µg/ml of streptomycin) containing recombinant murine macrophage colony stimulating factor (10 pg/µl) (PeproTech, Inc.). Isolated monocytes were incubated for 6 to 7 days at 37 °C and 5% CO_2 to promote monocyte differentiation into macrophages. Cells can be assessed for differentiation by morphology (Figure 5.2). Monocytes are typically round and can be adherent to the plate or floating in suspension. Macrophages are adherent and spread out in an elongated shape.

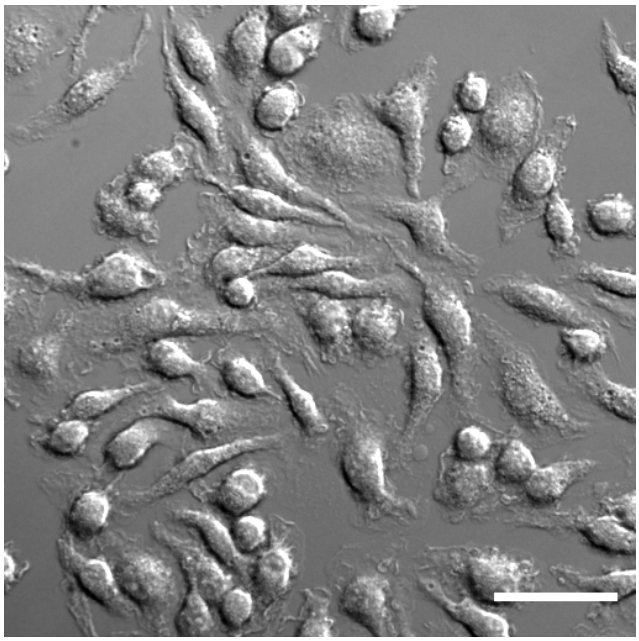

Figure 5.2 Typical macrophage morphology after differentiation.
DIC image of BMDMs after transfection and recovery. Differentiated macrophages are running and elongated, monocytes are tight and round similar to what is seen in the upper right-hand corner. Scale bar = 40 μm.

5.4.3 Bone Marrow Derived Macrophage Transfection

Differentiated primary macrophage at 6 days post isolation were harvested for transfection. First, the preconditioned media was removed and sterile filtered using a 0.22 μm PES syringe filter to be used as recovery media later. Then, cells were washed with cold PBS with 5 mM EGTA and incubated at 4˚C for 3-5 min then lifted by scraping with a nylon cell lifter (Corning™ C3008). Cells were centrifuged for 5 min at 50 X g and gently resuspended in 82 μl mouse macrophage transfection reagent and 18 μl supplement 1 (100 μl total) (Lonza, VVPA-1009) with 2.5 μg of DNA per 10^6 cells using a P1000 pipette tip, placed in an electroporation cuvette and subjected to nucleofection from Nucleofector® Program Y-001. Nucleofected cells were added back to 500 μl of their own preconditioned media and seeded into 35 mm glass-bottom dishes and incubated at 37°C with 5% CO_2 for 6 - 24 hours prior to imaging. For efficient seeding, recovered cells are plated into the bottom of the imaging dish and allowed to settle for up to 20 min without adding additional media to the dish.

Typically 125,000 cells were plated per imaging dish and were concentrated only onto the coverslip, not spread around to cover the entire bottom of the dish.

5.4.4 Zinc Manipulations to Cell Culture Media

For making Zn^{2+} manipulated media, fetal bovine serum was treated with Chelex 100 resin (Sigma-Aldrich, St. Louis, MO, USA) for 5 hours, stirring at 4˚C, then sterile filtered using a 0.22 µm PES membrane filter. "Chelex media" was made using DMEM (Sigma-Aldrich, St. Louis, MO, USA) supplemented with Chelex treated FBS (20%), L-glutamine (2 mM), sodium pyruvate (1 mM). Metal concentration values were measured by ICP-MS (Table 5.6). No calcium or iron was added back to the media. Zn^{2+} replete media was made by adding 30 µM $ZnCl_2$ (Sigma-Aldrich, St. Louis, MO, USA) to Chelex media. Zn^{2+} restricted conditions were made with Chelex media and used as is or by adding either 3 µM 2-{[Bis(2-pyridinylmethyl)amino]ethylamino}benzenesulfonic (ZX1) (Strem Chemicals, Inc.) or 1 µM Tris 2-pyridylmethyl amine (TPA) (Sigma-Aldrich, St. Louis, MO, USA).

Media	[Zn] (µM)	[Y] µM	[Ga] (µM)	[Ca] (mM)	[Cu] (µM)	[Fe] (µM)	[Mn] (µM)
DMEM + 20% Chelex FBS	3.48	4.88	6.17	1.13	26.98	26.12	0.21
DMEM 20% FBS	25.18	4.81	5.99	18.24	26.94	138.79	0.31

Table 5.6 Concentration values for Normal media and Chelex treated media measured by ICP-MS.

5.5 Salmonella Infections

5.5.1 HeLa cell infection

HeLa cells expressing GFP1-10 were challenged with *Salmonella* grown under SPI-1 inducing conditions at a multiplicity of infection (MOI) of 50. Infections were allowed to proceed for 45 minutes at 37°C and 5% CO_2 before gentamicin protection was carried out. For gentamycin protection, the *Salmonella*-containing media was exchanged with phenol red free DMEM containing 10% FBS (HeLa cells) and 100 µg/mL gentamicin to eliminate any non-internalized bacteria. After incubating for 45 minutes in a high concentration of gentamicin at 37°C and 5% CO_2, the media was replaced with

phenol red free DMEM containing 10% FBS and a low concentration (10 µg/mL) gentamicin to limit extracellular bacteria for the remainder of the experiment.

5.5.2 Bone marrow derived macrophage infection

Salmonella strains were grown overnight in LB with aeration. Bacteria were opsonized in a 1:1 solution of mouse serum (Sigma) and cell culture media (Gibco) for 30 min at 37 °C, pelleted at 13,000 X g for 1 min and resuspended in PBS prior to inoculation. Resting bone marrow derived macrophages on day 6 or 7 post differentiation expressing either GFP1-10 or NES-ZapCV2 were inoculated with opsonized *Salmonella* at MOI 10 – 30 and incubated at 37˚C and 5% CO_2 for 1 hour. Cells were then rinsed with PBS and switched to a low gentamicin containing media (10 µg/ml) for the remainder of the infection.

5.6 *Listeria* Infection

5.6.1 HeLa Cell Infection

To visualize fluorescent protein complementation in live infections, 0.15 x 10^6 HeLa cells were seeded two days before the infection in home-made imaging dishes (35 mm) with a 10 mm center hole covered by cover glass (No. 1.5, VWR, Aurora, CA). DNA encoding for GFP1-10 (or mNG1-10 or sfCh1-10) was transfected on day two using the *Trans*IT transfection system at a concentration of 2.5 µg per imaging dish according to the manufacturer's recommendations (Mirus Bio LLC, Madison, WI). One dish was treated equally and used on the day of the infection for counting to determine the multiplicity of infection (MOI). On the day of the infection, a saturated overnight culture of the *Listeria* strain of interest was diluted 10-fold in BHI media (supplemented with antibiotic as necessary) and grown for about three hours while periodically measuring the O.D. at 600 nm. When the O.D. at 600 nm reached 0.6-0.8, bacteria were pelleted and rinsed in DMEM media three times. To calculate the MOI, we assumed each O.D. unit at 600 nm corresponded to 10^9 bacteria/mL. Infections were performed at an MOI of 100. HeLa cells to be infected were rinsed with DMEM media three times. The media was then replaced with DMEM supplemented with *Listeria* cells. The infected cells were incubated in 37°C and 5% CO_2 for one hour. The media was then exchanged with DMEM media with 10% FBS,

supplemented with 20 ng/µL of Gentamicin (Fisher Scientific, Waltham, MA). The cells were then incubated for the remainder of the infection course in 37°C / 5% CO_2.

For infections without live cell complementation, 0.25 x 10^6 HeLa cells were seeded and the infection was performed as described above on the following day.

5.6.2 Bone Marrow Derived Macrophage Infection

Macrophage cells expressing GFP1-10 were infected with the pInlC-InlC-GFP11 containing strain of *Listeria* at an MOI of 5. Infections were allowed to proceed for 45 minutes at 37°C and 5% CO_2 before the media was changed to phenol red free DMEM and 20 µg/mL gentamicin. The cells were incubated in 37°C / 5% CO_2 during the course of the infection and while imaging on the microscope.

5.6.3 Immunofluorescence

For preserving GFP complementation fluorescence upon fixation, cells were fixed using 1% paraformaldehyde and 1% sucrose in PBS for 20 min and permeabilized using 0.1% Tween for 15 min. Cells were rinsed 3 times for 5 min each in PBS, slides were blocked with 200 µL of 5% FBS in PBS for 20 minutes. After rinsing in PBS, slides were incubated with the primary antibody in 5% FBS in PBS. Dilutions and sources of all antibodies and stains are listed in Table 5.6. After rinsing in PBS three times, the slides were incubated with the secondary antibody in 5% FBS in PBS. Alexa 594-phalloidin or Coumarin-phalloidin for actin staining was added together with the secondary antibody. After incubation with the secondary antibody, slides were washed in PBS, rinsed in water and mounted.

5.7 Colony Forming Unit (CFU) Determination

5.7.1 Salmonella

For quantification of intracellular bacterial burden by CFU at various times post infection, infected BMDMs in 6-well plates were rinsed 3x with PBS to remove extracellular bacteria. Cells were lifted and homogenized in 500 µl PBS and 50 µl was removed and mixed 1:1 in 50 µl 0.1% Triton X 100 in PBS and pipetted vigorously to release intracellular bacteria. Serial dilutions were made in PBS and

bacteria were plated on antibiotic containing LB agar plates and incubated overnight at 37˚C before counting colonies.

5.7.2 Listeria

For colony forming unit (CFU) assays, HeLa cells were infected with *Listeria* strains as described above in 6 well dishes in triplicates, at MOI 100. After infection for specified times, the media was removed and HeLa cells were washed 3x in PBS then lysed by incubation in 0.1% Triton X100 in PBS at room temperature. To quantify bacteria in each infection, serial dilutions were plated on BHI plates and CFUs were determined in technical triplicates.

5.8 Western Blotting

5.8.1 Salmonella

Measuring the secretion of tagged effector protein fusions was carried out by TCA precipitation of secreted *Salmonella* proteins in the culture supernatants. *Salmonella* strains harboring tagged effector protein plasmids were grown overnight under SPI-2 associated conditions (listed above) to induce effector secretion into the culture supernatants. Culture supernatants were collected by centrifugation at 14,000 x g for 30 minutes followed by 0.22 µm filtration. The supernatants were then precipitated with 10% TCA and collected by centrifugation for 10 min at max speed. Precipitated proteins were washed in pure acetone and dissolved in SDS-loading buffer and resolved using 14% SDS- PAGE and transferred to PVDF membrane for western blotting. Blots were blocked with 3% milk in TBS-T and probed with primary anti-SNAP-tag antibody (mouse) 1:1000 (New England Biolabs) or with anti-FLAG antibody (rabbit) 1:2000 (Sigma Aldrich, St. Louis, MO) overnight at 4˚C shaking. An HRP conjugated secondary antibody, goat anti-rabbit [HRP] or rabbit anti-mouse[HRP] (Novus Biologicals Inc), was used 1:2000 to stain the blot for 1 hour at room temperature before development and imaging. Immunoblots were developed with Amersham ECL Prime Western Blotting Detection Reagent (GE Healthcare Life Sciences, Pittsburgh, PA) and imaged on an ImageQuant LAS4000 imaging system (GE Healthcare Life Sciences, Pittsburgh, PA).

5.8.2 Listeria

To generate *Listeria* lysates, the equivalent of 1 mL bacterial culture for O.D. at 600 nm of 0.5 was pelleted and resuspended in 40 µL lysozyme buffer (20% sucrose, 10 mg/mL lysozyme, 10 mM Tris pH 8.0, 50 mM NaCl, 10 mM EDTA). The resuspended pellets were incubated at 55°C for 20 min. After addition of 10 µL of B-PER Bacterial Protein Extraction Reagent (Thermo Fisher Scientific, Lafayette, CO), the samples were incubated at room temperature for 15 min. Each cell lysate was diluted 1:1 with 2x SDS-PAGE loading buffer, spun for 5 min to remove debris and the supernatant was used for SDS-PAGE.

To generate cell lysates from HeLa cells infected with *Listeria*, the infections were carried out as described above in 6 well dishes. At the indicated time after infection, cells were washed with PBS twice and then scraped into 1 mL PBS. Cells were pelleted by centrifugation (2,500x*g* for 5 min) and resuspended in 100 µL RIPA buffer (150 mM NaCl, 1% Nonidet P-40, 0.5% deoxycholate, 0.1% SDS, 50 mM Tris pH 8.0, 5 mM EDTA) supplemented with 100x protease inhibitor (cOmplete™, Mini, EDTA-free Protease Inhibitor Cocktail, Sigma Aldrich, St. Louis, MO). After a 10-20 min incubation on ice, the lysates were spun at 20,000x*g* at 4°C for 10 min, and the clarified lysate was transferred to a new tube. The protein concentration in the lysate was determined by a BCA assay (Thermo Fisher Scientific, Lafayette, CO) according to the manufacturer's protocol.

For SDS-PAGE, O.D. normalized *Listeria* lysates (10 µL of the lysates prepared as described above) were loaded per well. Samples from infected HeLa cells were normalized by protein content and a volume containing 10 µg protein was loaded per lane. Protein samples were separated by SDS-PAGE on a 14% gel and stained by Coomassie according to standard protocols.

For Western blotting, the SDS-PAGE gel was transferred on to a PVDF membrane and probed with primary and secondary antibody as outlined in Table 5.6. Immunoblots were developed with Amersham ECL Prime Western Blotting Detection Reagent (GE Healthcare Life Sciences, Pittsburgh, PA) and imaged on an ImageQuant LAS4000 imaging system (GE Healthcare Life Sciences, Pittsburgh, PA).

Antibody / stain (source)	Dilution / incubation time	Purpose
Alexa 594-Phalloidin (Thermo Fisher Scientific, Waltham, MA)	1:1,000 / 45 min	Actin staining in fixed cells
Phalloidin-coumarin (Sigma-Aldrich, St. Louis, MO)	1:1,000 / 45 min	Actin staining in fixed cells
Anti-InlC (rabbit) (Cossart lab)	Immunofluorescence: 1:500 / 45 min at room temperature Western blotting: 1:500 / overnight at 4°C	Immunofluorescence and Western blotting
Anti-GFP (mouse) (Thermo Fisher Scientific, Waltham, MA)	1:1,000 / 45 min	Immunofluorescence
Goat anti-rabbit HRP conjugated (Novus Biologicals, Littleton, CO)	1:2,000 / 1 h at room temperature	Western blotting
Rabbit anti-mouse IgG (Alexa Fluor 488) (Thermo Fisher Scientific, Waltham, MA)	1:1,000 / 45 min at room temperature	Immunofluorescence
Donkey anti-rabbit IgG H&L (Alexa Fluor 488) (Abcam, Cambridge, MA)	1:1,000 / 45 min at room temperature	Immunofluorescence
Donkey anti-rabbit IgG H&L (Alexa Fluor 568) (Abcam, Cambridge, MA)	1:1,000 / 45 min at room temperature	Immunofluorescence

Table 5.7 Antibody concentrations and stains used for immunofluorescence and western blotting in *Listeria* infections.

5.9 Live Cell Fluorescence Imaging

5.9.1 Infections with *Salmonella*

Salmonella infections of HeLa cells with the split-GFP effector labeling system were imaged on a Nikon A1R laser scanning confocal microscope equipped with the Nikon Elements software platform, Ti-E Perfect Focus system, a motorized XY stage with a Ti Z drive and an environmental chamber (Pathology Devices) to maintain cells at 37°C, 5% CO_2 and 70% humidity. Images were acquired using a 40x oil objective (NA 1.30) and the following channels: red (561 nm laser line, PMT gain: 100, emission filter: 600/50 nm), green (488 nm laser line, PMT gain: 120, emission filter: 525/50 nm), and bright field DIC. All imaging was performed with the channel series function engaged to prevent bleed-through between fluorescence channels and all fields of view were imaged with a pixel dwell time of 2 µs. Long-term imaging of infected cells was done between 5-25 hours post infection, acquiring images every 15 minutes. The motorized XY stage was used to select and store the locations of multiple fields

of view in order to follow the fates of many infected cells over the course of the experiment. The Z drive was used to generate z slices that stack to encompass the entirety of the cells within each field of view, thus ensuring the complete detection of any bacteria and effector-GFP_{comp} signal present. Select images were acquired with a digital zoom, sampling at Nyquist resolution to capture effector-GFP_{comp} signal in detail. All images were processed using Fiji to merge individual fluorescence channels and to flatten Z stacks using the Maximum z Projection algorithm into a single image per time point and per field of view. Background fluorescence signal was subtracted using the rolling ball background correction algorithm with a radius set to 100 pixels. Fluorescence signal intensities were false colored and brightness and contrast were held to equivalent values per channel between images.

Imaging of split-GFP complementation within *Salmonella* was imaged on a Nikon Ti-E microscope fitted with a Yokogawa CSU-X1 spinning disc head and equipped with the Nikon Elements High Content Analysis (HCA) software platform, Ti-E Perfect Focus system, a motorized XY stage with a Ti Z drive and a fully enclosed environmental chamber (Oko Labs) to maintain cells at 37°C, 5% CO_2 and 70% humidity. Images were acquired using a 40x air objective (NA 0.95) and the following channels: red (mRuby3: 561 nm laser line, emission filter: 620/60 nm; mCherry: 594 nm laser line, emission filter: 645/75 nm), green (488 nm laser line, emission filter: 525/50 nm), and bright field DIC (HBO arc lamp) detected with an iXon Ultra 888 EMCCD camera (Andor). Fluorescence channels were acquired with a readout mode of 10mHz at 16 bit and an EM gain of 300.

5.9.2 Infections with *Listeria*

Fluorescence images were acquired on a Nikon Ti-E widefield fluorescence microscope equipped with Nikon elements software, Ti-E perfect focus system, an iXon3 EMCCD camera (Andor), mercury arc lamp, GFP (480/10 excitation, 490 dichroic, 510/10 emission) and mCherry (560/10 excitation, 585 dichroic, 610/25 emission) filter sets. External excitation and emission filter wheels were controlled by a Lambda 10-3 filter changer (Sutter Instruments), while dichroic mirrors were placed on cubes in the dichroic turret. Images were collected using a 60X oil objective (NA 1.40) and exposures, EM gain settings and neutral density filter settings are listed in Table 5.8 for each data set in this study. Live cells were maintained at 37°C and 5% CO_2 in a LiveCell™ environment chamber (Pathology Devices)

during the experiments. For time course infection experiments (Fig. 3.4b), images were collected every 15 min.

For high throughput comparison of GFP complementation (Fig. 3.6), a Nikon Ti-E HCA widefield fluorescence microscope was used. This system was equipped with Nikon elements software, Ti-E perfect focus system, a digital CMOS camera (Hamamatsu), a Lumencor Spectra X light engine® 500 mW solid state light source, and DAPI (395 excitation, 475/20 emission), GFP (470 excitation, 540/21 emission) and brightfield transmitted illumination using a PEKA light engine (Lumencor). Images were collected using a Plan Apo λ 40x Ph2 DM air objective (NA 0.95). Images were acquired at 50% light intensity for 200ms for each fluorescent or brightfield channel, every 15 min over the time course of the experiment. Live cells were maintained at 37°C and 5% CO_2 in an Okolab™ cage incubator during the experiment.

Immunofluorescence of infections (Fig. 3.4, 3.5)	GFP: 287 ms exposure, EM gain 1 MHz at 16-bit readout mode, EM gain multiplier = 200, neutral density filter (25% emission)	mCherry: 90 ms exposure, EM gain 1 MHz at 16-bit readout mode, EM gain multiplier = 200, neutral density filter (25% emission)	DIC: 50 ms exposure, EM gain 1 MHz at 16-bit readout mode, EM gain multiplier = 0, neutral density filter (25% emission)
Proof of principle live imaging of split-GFP complementation (Fig. 3.3a)	GFP: 50 ms exposure, EM gain 1 MHz at 16-bit readout mode, EM gain multiplier = 200, neutral density filter (25% emission)	Dapi: 287 ms exposure, EM gain 1 MHz at 16-bit readout mode, EM gain multiplier = 200, neutral density filter (25% emission)	DIC: 50 ms exposure, EM gain 1 MHz at 16-bit readout mode, EM gain multiplier = 0, neutral density filter (25% emission)
GFP complementation time course (Fig. 3.3b)	GFP: 50 ms exposure, EM gain 1 MHz at 16-bit readout mode, EM gain multiplier = 200, neutral density filter (25% emission)	Dapi: 287 ms exposure, EM gain 1 MHz at 16-bit readout mode, EM gain multiplier = 200, neutral density filter (25% emission)	DIC: 50 ms exposure, EM gain 1 MHz at 16-bit readout mode, EM gain multiplier = 0, neutral density filter (25% emission)
GFP complementation promoter comparison end point (Fig. 3.7)	GFP: 287 ms exposure, EM gain 1 MHz at 16-bit readout mode, EM gain multiplier = 200	Dapi: 287 ms exposure, EM gain 1 MHz at 16-bit readout mode, EM gain multiplier = 200	DIC: 70 ms exposure, EM gain 1 MHz at 16-bit readout mode, EM gain multiplier = 0
Super-folder Cherry complementation (Fig. 3.10a)	mCherry: 287 ms exposure, EM gain 1 MHz at 16-bit readout mode, EM gain multiplier = 200	DIC: 50 ms exposure, EM gain 1 MHz at 16-bit readout mode, EM gain multiplier = 200	
mNeonGreen complementation (Fig. 3.10b)	GFP: 287 ms exposure, EM gain 1 MHz at 16-bit readout mode, EM gain multiplier = 200	DIC: 50 ms exposure, EM gain 1 MHz at 16-bit readout mode, EM gain multiplier = 0	
GFP complementation in macrophages (Fig. 3.9)	GFP: 287 ms exposure, EM gain 1 MHz at 16-bit readout mode, EM gain multiplier = 200	Dapi: 287 ms exposure, EM gain 1 MHz at 16-bit readout mode, EM gain multiplier = 200	DIC: 90 ms exposure, EM gain 1 MHz at 16-bit readout mode, EM gain multiplier = 0

Table 5.8 Settings for fluorescence microscopy on Nikon Ti-E widefield fluorescence microscope.

5.9.3 ZapCV2 Imaging, Calibrations and Data Analysis

For quantification of cytosolic labile Zn^{2+} in primary macrophages, calibration experiments were performed at the indicated times post infection on a Nikon Ti-E widefield fluorescence microscope equipped with Nikon elements software, Ti-E perfect focus system, an iXon3 EMCCD camera (Andor),

mercury arc lamp, and YFP FRET (434/16 excitation, 458 dichroic, 535/20 emission), CFP (434/16 excitation, 458 dichroic, 470/24 emission), and YFP (495/10 excitation, 515 dichroic, 535/20 emission) filter sets. External excitation and emission filter wheels were controlled by a Lambda 10-3 filter changer (Sutter Instruments), while dichroic mirrors were placed on cubes in the dichroic turret. It is important to ensure that the channel setting for both YFP FRET and CFP are set to be the same. Images were collected using a 60X oil objective (NA 1.40), 200 ms exposure time, EM gain 1 MHz at 16-bit readout mode with an EM gain multiplier of 200, and a neutral density filter with 25% light transmission. Sensor expression level was controlled by selecting cells with YFP intensities between 4,000-15,000 fluorescence units under these conditions. 8 fields of view were collected using multipoint acquisition mode and the Perfect Focus System (PFS) set to 'ON' in between points. Cells were maintained at 37°C and 5% CO_2 in a LiveCell™ environment chamber (Pathology Devices) during the experiments. Images were collected every minute.

Fresh calibration solutions were prepared the day of the experiment and include a 2x solution of R_{min} buffer (TPA in PO_4^{3-}-free HHBSS) for minimum FRET ratio collection and a 2x solution of R_{max} buffer (0.001% saponin + 0.75 µM pyrithione + buffered Zn^{2+} in PO_4^{3-}-, Ca^{2+}-, Mg^{2+}-free HEPES-buffered HBSS) for collecting the maximum FRET ratio. The resting FRET ratio of the sensor was collected for 10 mins prior to calibration to ensure a stable signal. After 10 min of imaging, 50 µM TPA was added to the dish to collect the minimum FRET ratio of the sensor. Once a stable signal had been achieved, cells were then washed with PO_4^{3-}-, Ca^{2+}-, Mg^{2+}-free HEPES-buffered HBSS, pH = 7.4 to remove the chelate, followed by treatment with pyrithione and Zn^{2+} with 0.001% (w/v) saponin. For a detailed protocol, please see Appendix B (page 170) of Carter, Kyle Pierce, "Engineering and Evaluating Fluorescent Tools for Endoplasmic Reticulum Zinc" (2017). Chemistry & Biochemistry Graduate Theses & Dissertations. 223 https://scholar.colorado.edu/chem_gradetds/223

All imaging data were analyzed in MATLAB (Mathworks) (Appendix A). Images were background corrected by subtracting a local background intensity from each pixel grouped in a certain region of the image. ROIs were generated by using a segmentation algorithm that segments the image based

on the fluorescence intensity of the FRET ratio channel. FRET ratios for each cell were calculated by dividing the background-corrected YFP FRET intensity by the background-corrected CFP intensity.

5.10 Flow Cytometry Acquisition and Analysis

For analysis of intracellular bacterial replication, BMDMs were grown and infected in 6-well plates and the Zn^{2+} or drug treatment was applied at 2 hours post infection. At the indicated time point post infection, cells were rinsed 3 times in PBS and lifted by scraping with a nylon cell lifter (Corning™ C3008) and homogenized by pipetting gently with a P1000. Homogenized cells were fixed in a gentle fixative for preserving fluorescent protein fluorescence, 1% PFA and 1% sucrose, for 15 min and then washed and resuspended in PBS and chilled at 4˚C. Samples were analyzed on a BD FACSCelesta™ (BD Bioscences) collecting forward scatter area and width, side scatter area and width, 488 nm excitation 530/30 nm emission, and 561 nm excitation and 585/15 nm emission. Data was analyzed using FlowJo 10.5.3 software (FlowJo LLC). The cell gating hierarchy was set as Single cells > GFP positive cells > Cells containing replicated bacteria. 10,000 GFP positive cells were collected per sample. Single cells were determined first by forward scatter area versus side scatter area then by side scatter width versus side scatter area. Non-fluorescent uninfected cells were used to set the gate for GFP positive cells. A ratio of the 488 nm channel with the 561 nm channel was taken by dividing 488 nm intensity by 561 nm intensity. Samples collected at 2 hours post infection were used as the "initial inoculum" to determine the fluorescence intensities for cells that have bacteria that have not undergone replication. Cells containing replicated bacteria were gated as having a 488 nm:561 nm ratio above the initial inoculum (Figure 4.4).

5.11 RNA Extraction, Purification, RT-qPCR, and RNAseq

For extraction of RNA from BMDMs, cells were plated in 6-well plates and infected day 7 post isolation with the indicated treatments as described above. At the indicated timepoints, BMDMs were washed 3x in PBS prior to RNA extraction then lysed using RLT buffer (Qiagen), homogenized using a sterile syringe and 25-gauge needle (BD Biosciences), and purified using the RNeasy Mini Kit (Qiagen).

For RT-qPCR, total isolated RNA was reverse transcribed into cDNA using ProtoScript II reverse transcriptase (New England Biolabs) and $d(T)_{23}VN$ (50 μM) to copy only polyadenylated mRNA. cDNA samples were diluted 1:20 in ultrapure milliQ to be used as templates for qPCR. Diluted cDNA templates were analyzed on a CFX384 Touch Real-Time PCR Detection System (BioRad) using Sybr Select master mix (Applied Biosystems™). Relative copy numbers of selected genes were normalized to the house keeping gene Syntaxin (Stx5a)[250] using the Pfaffl method[251].

$$Ratio = \frac{(E_{target})^{\Delta Ct_{target}(control-sample)}}{(E_{ref})^{\Delta Ct_{ref}(control-sample)}}$$

The efficiency of each primer is calculated by the slope of the line of a calibration curve of the log dilution vs Ct, given by $Efficiency = 10^{(\frac{1}{slope})}$ qPCR Primers are listed in Table 5.8.

Primer Name	Sequence	Tm	Amplicon size	Concentration	Efficiency
Stx5a	CGGAAACGCTACGGATCTAAG	55.2	77	200 nM	1.95
	CAGGGGACAGAACCTGTGT	56.9			
Zip14	CGGTCCCAGACAACAAGATT	55	116	200 nM	1.98
	TGGCTTGTGGTGTGAAATGT	55.2			
MT2	CAAACCGATCTCTCGTCGAT	54.4	121	200 nM	1.81
	CATTTGCATTGTTTGCATTTG	50			
ZnT4	CTGCCGTCCTCTACTTCGTT	57	130	200 nM	1.94
	GCATATGGAGTGCATCTGTCA	54.9			
Spliced Xbp1	CTGAGTCCGAATCAGGTGCAG	57.7	75	200 nM	1.85
	GTCCATGGGAAGATGTTCTGG	55.4			

Table 5.9 Primer sequences and attributes for qPCR of zinc regulatory and ER stress related genes in *Salmonella*-infected BMDMs treated with zinc manipulations or drugs.

For RNAseq, total RNA was harvested from *Salmonella*-infected BMDMs as described above. Total RNA from each sample was processed into sequencing libraries with TruSeq Stranded mRNA library prep kit (Illumina). Sequencing libraries were run on an Illumina NextSeq 500 using NextSeq 500/550 High Output Kit v2.5 (Illumina) in The BioFrontiers Next-Gen Sequencing Facility at University of Colorado Boulder. Raw sequence data was analyzed for QC using RSubread, mapped with HiSat2 to the mm10 gene list and counted with Feature Counts. Differential expression analysis was done with DESeq2 and EdgeR. Transcripts per million reads mapped (TPM) was calculated from DESeq2 output.

Bibliography

1. Majowicz, S. E. *et al.* The global burden of nontyphoidal Salmonella gastroenteritis. *Clin Infect Dis* **50**, 882–889 (2010).

2. Crump, J. A., Luby, S. P. & Mintz, E. D. The global burden of typhoid fever. *Bull World Heal. Organ* **82**, 346–353 (2004).

3. Collins, F. M. & Carter, P. B. Growth of salmonellae in orally infected germ free mice. *Infect Immun* **21**, 41–47 (1978).

4. Gopinath, S., Carden, S. & Monack, D. Shedding light on Salmonella carriers. *Trends Microbiol* **20**, 320–327 (2012).

5. Gopinath, S., Lichtman, J. S., Bouley, D. M., Elias, J. E. & Monack, D. M. Role of disease-associated tolerance in infectious superspreaders. *Proc Natl Acad Sci U S A* **111**, 15780–15785 (2014).

6. Galan, J. E. Salmonella interactions with host cells: type III secretion at work. *Annu Rev Cell Dev Biol* **17**, 53–86 (2001).

7. Radics, J., Konigsmaier, L. & Marlovits, T. C. Structure of a pathogenic type 3 secretion system in action. *Nat Struct Mol Biol* **21**, 82–87 (2014).

8. Galan, J. E. & Wolf-Watz, H. Protein delivery into eukaryotic cells by type III secretion machines. *Nature* **444**, 567–573 (2006).

9. Ellermeier, J. R. & Slauch, J. M. Adaptation to the host environment: regulation of the SPI1 type III secretion system in Salmonella enterica serovar Typhimurium. *Curr Opin Microbiol* **10**, 24–29 (2007).

10. Sun, H., Kamanova, J., Lara-Tejero, M. & Galán, J. E. A Family of Salmonella Type III Secretion Effector Proteins Selectively Targets the NF-κB Signaling Pathway to Preserve Host Homeostasis. *PLoS Pathog.* **12**, 1–19 (2016).

11. Vazquez-Torres, A. *et al.* Salmonella pathogenicity island 2-dependent evasion of the phagocyte NADPH oxidase. *Sci. (New York, NY)* **287**, 1655–1658 (2000).

12. Cirillo, D. M., Valdivia, R. H., Monack, D. M. & Falkow, S. Macrophage-dependent induction of

theSalmonellapathogenicity island 2 type III secretion system and its role in intracellular survival. *Mol Microbiol* **30**, 175–188 (1998).

13. Salcedo, S. P., Noursadeghi, M., Cohen, J. & Holden, D. W. Intracellular replication of Salmonella typhimurium strains in specific subsets of splenic macrophages in vivo. *Cell Microbiol* **3**, 587–597 (2001).

14. Sheppard, M. *et al.* Dynamics of bacterial growth and distribution within the liver during Salmonella infection. *Cell Microbiol* **5**, 593–600 (2003).

15. Richter-Dahlfors, A., Buchan, A. M. & Finlay, B. B. Murine salmonellosis studied by confocal microscopy: Salmonella typhimurium resides intracellularly inside macrophages and exerts a cytotoxic effect on phagocytes in vivo. *J Exp Med* **186**, 569–580 (1997).

16. Ramos-Morales, F. Impact of Salmonella enterica Type III Secretion System Effectors on the Eukaryotic Host Cell. *ISRN Cell Biol.* **2012**, 1–36 (2012).

17. Van Engelenburg, S. B. & Palmer, A. E. Imaging type-III secretion reveals dynamics and spatial segregation of Salmonella effectors. *Nat Methods* **7**, 325–330 (2010).

18. Van Engelenburg, S. B. & Palmer, A. E. Quantification of real-time Salmonella effector type III secretion kinetics reveals differential secretion rates for SopE2 and SptP. *Chem Biol* **15**, 619–628 (2008).

19. Figueira, R. & Holden, D. W. Functions of the Salmonella pathogenicity island 2 (SPI-2) type III secretion system effectors. *Microbiology* **158**, 1147–1161 (2012).

20. Boucrot, E., Henry, T., Borg, J. P., Gorvel, J. P. & Meresse, S. The intracellular fate of Salmonella depends on the recruitment of kinesin. *Science (80-.).* **308**, 1174–1178 (2005).

21. Rosa-Ferreira, C. & Munro, S. Arl8 and SKIP act together to link lysosomes to kinesin-1. *Dev Cell* **21**, 1171–1178 (2011).

22. Salomon, D. & Orth, K. What pathogens have taught us about posttranslational modifications. *Cell Host Microbe* **14**, 269–279 (2013).

23. Patel, S., Wall, D. M., Castillo, A. & McCormick, B. A. Caspase-3 cleavage of Salmonella type III secreted effector protein SifA is required for localization of functional domains and bacterial dissemination. *Gut Microbes* **10**, 172–187 (2019).

24. Cossart, P. Illuminating the landscape of host-pathogen interactions with the bacterium Listeria monocytogenes. *Proc. Natl. Acad. Sci.* **108**, 19484–19491 (2011).

25. Hamon, M., Bierne, H. & Cossart, P. Listeria monocytogenes: A multifaceted model. *Nat. Rev. Microbiol.* **4**, 423–434 (2006).

26. Camejo, A. *et al.* The arsenal of virulence factors deployed by Listeria monocytogenes to promote its cell infection cycle. *Virulence* **2**, 379–394 (2011).

27. Desvaux, M. & Hébraud, M. The protein secretion systems in Listeria: Inside out bacterial virulence. *FEMS Microbiol. Rev.* **30**, 774–805 (2006).

28. Renier, S., Micheau, P., Talon, R., Hébraud, M. & Desvaux, M. Subcellular localization of

extracytoplasmic proteins in monoderm bacteria: Rational secretomics-based strategy for genomic and proteomic analyses. *PLoS One* **7**, (2012).

29. Bierne, H. & Cossart, P. Listeria monocytogenes Surface Proteins: from Genome Predictions to Function. *Microbiol. Mol. Biol. Rev.* **71**, 377–397 (2007).

30. Lenz, L. L. & Portnoy, D. A. Identification of a second Listeria secA gene associated with protein secretion and the rough phenotype. *Mol. Microbiol.* **45**, 1043–1056 (2002).

31. Renier, S. *et al.* Exoproteomic analysis of the SecA2-dependent secretion in Listeria monocytogenes EGD-e. *J. Proteomics* **80**, 183–195 (2013).

32. Dumas, E., Desvaux, M., Chambon, C. & Hébraud, M. Insight into the core and variant exoproteomes of Listeria monocytogenes species by comparative subproteomic analysis. *Proteomics* **9**, 3136–3155 (2009).

33. Tilney, L. G. Actin filaments and the growth, movement, and spread of the intracellular bacterial parasite, Listeria monocytogenes. *J. Cell Biol.* **109**, 1597–1608 (2004).

34. Dabiri, G. A., Sanger, J. M., Portnoy, D. A. & Southwick, F. S. Listeria monocytogenes moves rapidly through the host-cell cytoplasm by inducing directional actin assembly. *Proc. Natl. Acad. Sci.* **87**, 6068–6072 (1990).

35. Welch, M. D., Iwamatsu, A. & Mitchison, T. J. Actin polymerization is induced by Arp2/3 protein complex at the surface of. *List. monocytogenes. Nat.* **385**, 265–269 (1997).

36. Gouin, E., Welch, M. D. & Cossart, P. Actin-based motility of intracellular pathogens. *Curr. Opin. Microbiol.* **8**, 35–45 (2005).

37. Travier, L. & Lecuit, M. Listeria monocytogenes ActA: A new function for a 'classic' virulence factor. *Curr. Opin. Microbiol.* **17**, 53–60 (2014).

38. Travier, L. *et al.* ActA Promotes Listeria monocytogenes Aggregation, Intestinal Colonization and Carriage. *PLoS Pathog.* **9**, (2013).

39. Kayal, S. & Charbit, A. Listeriolysin O: A key protein of Listeria monocytogenes with multiple functions. *FEMS Microbiol. Rev.* **30**, 514–529 (2006).

40. Cossart, P. *et al.* Listeriolysin-O Is Essential for Virulence of Listeria-Monocytogenes - Direct Evidence Obtained By Gene Complementation. *Infect. Immun.* **57**, 3629–3636 (1989).

41. Schnupf, P. & Portnoy, D. A. Listeriolysin O: a phagosome-specific lysin. *Microbes Infect.* **9**, 1176–1187 (2007).

42. Hamon, M. A., Ribet, D., Stavru, F. & Cossart, P. Listeriolysin O: the Swiss army knife of Listeria. *Trends Microbiol.* **20**, 360–8 (2012).

43. Hamon, M. A. *et al.* Histone modifications induced by a family of bacterial toxins. *Proc Natl Acad Sci U S A* **104**, 13467–13472 (2007).

44. Stavru, F., Palmer, A. E., Wang, C., Youle, R. J. & Cossart, P. Atypical mitochondrial fission upon bacterial infection. *Proc Natl Acad Sci U S A* **110**, 16003–16008 (2013).

45. Rajashekar, R., Liebl, D., Chikkaballi, D., Liss, V. & Hensel, M. Live cell imaging reveals novel functions of Salmonella enterica SPI2-T3SS effector proteins in remodeling of the host cell endosomal system. *PLoS One* **9**, e115423 (2014).

46. Enninga, J., Mounier, J., Sansonetti, P. & Nhieu, G. T. Van. Secretion of type III effectors into host cells in real time. *Nat. Methods* **2**, 959–965 (2005).

47. Gawthorne, J. A. *et al.* Visualizing the Translocation and Localization of Bacterial Type III Effector Proteins by Using a Genetically Encoded Reporter System. *Appl. Environ. Microbiol.* **82**, 2700–2708 (2016).

48. Buckley, A. M., Petersen, J., Roe, A. J., Douce, G. R. & Christie, J. M. LOV-based reporters for fluorescence imaging. *Curr. Opin. Chem. Biol.* **27**, 39–45 (2015).

49. Cabantous, S., Terwilliger, T. C. & Waldo, G. S. Protein tagging and detection with engineered self-assembling fragments of green fluorescent protein. *Nat. Biotechnol.* **23**, 102–107 (2005).

50. Young, A. M., Minson, M., McQuate, S. E. & Palmer, A. E. Optimized Fluorescence Complementation Platform for Visualizing Salmonella Effector Proteins Reveals Distinctly Different Intracellular Niches in Different Cell Types. *ACS Infect. Dis.* **3**, 575–584 (2017).

51. Batan, D. *et al.* A Multicolor Split-Fluorescent Protein Approach to Visualize Listeria Protein Secretion in Infection. *Biophys. J.* 1–12 (2018). doi:10.1016/j.bpj.2018.03.016

52. Feng, S. *et al.* Bright split red fluorescent proteins with enhanced complementation efficiency for the tagging of endogenous proteins and visualization of synapses. (2018). doi:https://doi.org/10.1101/454041

53. Feng, S. *et al.* Improved split fluorescent proteins for endogenous protein labeling. *Nat. Commun.* **8**, 370 (2017).

54. Batan, D. *et al.* A Multicolor Split-Fluorescent Protein Approach to Visualize Listeria Protein Secretion in Infection. *Biophys. J.* **115**, 251–262 (2018).

55. Weiss, G. & Schaible, U. E. Macrophage defense mechanisms against intracellular bacteria. *Immunol. Rev.* **264**, 182–203 (2015).

56. Skaar, E. P. The Battle for Iron between Bacterial Pathogens and Their Vertebrate Hosts. *PLoS Pathog.* **6**, e1000949 (2010).

57. Hennigar, S. R. & McClung, J. P. Nutritional Immunity: Starving Pathogens of Trace Minerals. *Am. J. Lifestyle Med.* **10**, 170–173 (2014).

58. Cerasi, M., Ammendola, S. & Battistoni, A. Competition for zinc binding in the host-pathogen interaction. *Front. Cell. Infect. Microbiol.* **3**, 108 (2013).

59. Fang, F. C. Antimicrobial reactive oxygen and nitrogen species: concepts and controversies. *Nat Rev Microbiol* **2**, 820–832 (2004).

60. Slauch, J. M. How does the oxidative burst of macrophages kill bacteria? Still an open question. *Mol Microbiol* **80**, 580–583 (2011).

61. Subramanian Vignesh, K., Landero Figueroa, J. A., Porollo, A., Caruso, J. A. & Deepe, G. S.

Granulocyte macrophage-colony stimulating factor induced Zn sequestration enhances macrophage superoxide and limits intracellular pathogen survival. *Immunity* **39**, 697–710 (2013).

62. Kapetanovic, R. *et al.* Salmonella employs multiple mechanisms to subvert the TLR-inducible zinc-mediated antimicrobial response of human macrophages. *FASEB J* **30**, 1901–1912 (2016).

63. Botella, H. *et al.* Mycobacterial P1-Type ATPases Mediate Resistance to Zinc Poisoning in Human Macrophages. *Cell Host Microbe* **10**, 248–259 (2011).

64. Botella, H., Stadthagen, G., Lugo-Villarino, G., de Chastellier, C. & Neyrolles, O. Metallobiology of host-pathogen interactions: An intoxicating new insight. *Trends in Microbiology* (2012). doi:10.1016/j.tim.2012.01.005

65. Monack, D. M., Bouley, D. M. & Falkow, S. Salmonella typhimurium persists within macrophages in the mesenteric lymph nodes of chronically infected Nramp1+/+ mice and can be reactivated by IFNgamma neutralization. *J Exp Med* **199**, 231–241 (2004).

66. Malik-Kale, P. *et al.* Salmonella- at home in the host cell. *Front. Microbiol.* **2**, 1–9 (2011).

67. Rosenberger, C. M. & Finlay, B. B. Phagocyte sabotage: Disruption of macrophage signalling by bacterial pathogens. *Nat. Rev. Mol. Cell Biol.* **4**, 385–396 (2003).

68. Liu, J. Z. *et al.* Zinc sequestration by the neutrophil protein calprotectin enhances salmonella growth in the inflamed gut. *Cell Host Microbe* **11**, 227–239 (2012).

69. Bullen, J. J., Griffiths, E. & Edmiston, C. E. IRON AND INFECTION: MOLECULAR, PHYSIOLOGICAL AND CLINICAL ASPECTS, 2ND EDITION. *Shock* **12**, (1999).

70. Nakashige, T. G., Zhang, B., Krebs, C. & Nolan, E. M. Human calprotectin is an iron-sequestering host-defense protein. *Nat. Chem. Biol.* **11**, 765–771 (2015).

71. Diaz-Ochoa, V. E. *et al.* Salmonella Mitigates Oxidative Stress and Thrives in the Inflamed Gut by Evading Calprotectin-Mediated Manganese Sequestration. *Cell Host Microbe* **19**, 814–825 (2016).

72. Neyrolles, O. Mycobacteria , metals , and the macrophage. *Immunol. Rev.* 249–263 (2015).

73. McCracken, J. M. & Allen, L. H. Regulation of Human Neutrophil Apoptosis and Lifespan in Health and Disease. *J. Cell Death* **7**, JCD.S11038 (2014).

74. Lathrop, S. K. *et al.* Replication of Salmonella enterica Serovar Typhimurium in Human Monocyte-Derived Macrophages. *Infect Immun* **83**, 2661–2671 (2015).

75. Loomis, W. P. *et al.* Temporal and anatomical host resistance to chronic Salmonella infection is quantitatively dictated by nramp1 and influenced by host genetic background. *PLoS One* **9**, (2014).

76. Wessling-Resnick, M. Nramp1 and other transporters involved in metal withholding during infection. *J. Biol. Chem.* **290**, 18984–18990 (2015).

77. Krężel, A. & Maret, W. The biological inorganic chemistry of zinc ions. *Arch. Biochem. Biophys.* **611**, 3–19 (2016).

78. Maret, W. & Li, Y. Coordination Dynamics of Zinc in Proteins. *Chem. Rev.* **109**, 4682–4707 (2009).

79. Changela, A. *et al.* Molecular Basis of Selectivity and Sensitivity in Metal-Ion Recognition by CueR. *Science (80-.).* **301**, 1383–1387 (2003).

80. Outten, C. E. & O'Halloran, T. V. Femtomolar sensitivity of metalloregulatory proteins controlling zinc homeostasis. *Science* **292**, 2488–2492 (2001).

81. Krężel, A. & Maret, W. Zinc-buffering capacity of a eukaryotic cell at physiological pZn. *J. Biol. Inorg. Chem.* **11**, 1049–1062 (2006).

82. Qin, Y., Dittmer, P. J., Park, J. G., Jansen, K. B. & Palmer, A. E. Measuring steady-state and dynamic endoplasmic reticulum and Golgi Zn2+ with genetically encoded sensors. *Proc Natl Acad Sci U S A* **108**, 7351–7356 (2011).

83. Andreini, C., Banci, L., Bertini, I. & Rosato, A. Counting the zinc-proteins encoded in the human genome. *J. Proteome Res.* **5**, 196–201 (2006).

84. Maret, W. Zinc in cellular regulation: The nature and significance of "zinc signals". *Int. J. Mol. Sci.* **18**, (2017).

85. Kambe, T., Hashimoto, A. & Fujimoto, S. Current understanding of ZIP and ZnT zinc transporters in human health and diseases. *Cell. Mol. Life Sci.* **71**, 3281–3295 (2014).

86. Kambe, T., Tsuji, T., Hashimoto, A. & Itsumura, N. The Physiological, Biochemical, and Molecular Roles of Zinc Transporters in Zinc Homeostasis and Metabolism. *Physiol Rev* **95**, 749–784 (2015).

87. Guerinot, M. Lou. The ZIP family of metal transporters. *Biochim. Biophys. Acta - Biomembr.* **1465**, 190–198 (2000).

88. Krebs, N. F. Overview of Zinc Absorption and Excretion in the Human Gastrointestinal Tract. *J. Nutr.* **130**, 1374S-1377S (2000).

89. Guthrie, G. J. *et al.* Influence of ZIP14 (slc39A14) on intestinal zinc processing and barrier function. *Am. J. Physiol. - Gastrointest. Liver Physiol.* **308**, G171–G178 (2015).

90. Mwangi, M. N. *et al.* Insects as sources of iron and zinc in human nutrition. *Nutr. Res. Rev.* **31**, 248–255 (2018).

91. Lönnerdal, B. Zinc and Health : Current Status and Future Directions. Dietary Factors Influencing Zinc Absorption. *J. Nutr.* **130**, S1378-1383 (2000).

92. Foster, M., Chu, A., Petocz, P. & Samman, S. Effect of vegetarian diets on zinc status: A systematic review and meta-analysis of studies in humans. *J. Sci. Food Agric.* **93**, 2362–2371 (2013).

93. Hess, S. Y., Peerson, J. M., King, J. C. & Brown, K. H. Use of serum zinc concentration as an indicator of population zinc status. *Food Nutr Bull* **28**, S403-29 (2007).

94. Kim, J. & Ahn, J. Effect of zinc supplementation on inflammatory markers and adipokines in young obese women. *Biol. Trace Elem. Res.* **157**, 101–106 (2014).

95. Iovino, L. *et al.* High-dose zinc oral supplementation after stem cell transplantation causes an increase of TRECs and CD4+ naïve lymphocytes and prevents TTV reactivation. *Leuk. Res.* **70**, 20–24 (2018).

96. Plum, L. M., Rink, L. & Hajo, H. The essential toxin: Impact of zinc on human health. *Int. J. Environ. Res. Public Health* **7**, 1342–1365 (2010).

97. Wessells, K. R. & Brown, K. H. Estimating the Global Prevalence of Zinc Deficiency: Results Based on Zinc Availability in National Food Supplies and the Prevalence of Stunting. *PLoS One* **7**, (2012).

98. WHO. WORLD HEATH REPORT: Reducing Risks, Promoting Healthy Life. 1–230 (2002).

99. Livingstone, C. Zinc: Physiology, deficiency, and parenteral nutrition. *Nutr. Clin. Pract.* **30**, 371–382 (2015).

100. Croxford, T. P., McCormick, N. H. & Kelleher, S. L. Moderate Zinc Deficiency Reduces Testicular Zip6 and Zip10 Abundance and Impairs Spermatogenesis in Mice. *J. Nutr.* **141**, 359–365 (2011).

101. Shankar, A. H. & Prasad, A. S. Zinc and immune function: the biological basis of altered resistance to infection. *Am J Clin Nutr* **68**, 447S-463S (1998).

102. Wang, J., Um, P., Dickerman, B. A. & Liu, J. Zinc, magnesium, selenium and depression: A review of the evidence, potential mechanisms and implications. *Nutrients* **10**, 1–19 (2018).

103. Wong, H. R. *et al.* Genome-level expression profiles in pediatric septic shock indicate a role for altered zinc homeostasis in poor outcome. *Physiol. Genomics* **30**, 146–155 (2007).

104. Bao, S. *et al.* Zinc modulates the innate immune response in vivo to polymicrobial sepsis through regulation of NF-κB. *Am. J. Physiol. Cell. Mol. Physiol.* **298**, L744–L754 (2010).

105. Knoell, D. L. *et al.* Zinc deficiency increases organ damage and mortality in a murine model of polymicrobial sepsis. *Crit. Care Med.* **37**, 1380–1388 (2009).

106. Wessels, I. & Cousins, R. J. Zinc dyshomeostasis during polymicrobial sepsis in mice involves zinc transporter Zip14 and can be overcome by zinc supplementation. *Am. J. Physiol. - Gastrointest. Liver Physiol.* **309**, G768–G778 (2015).

107. Maywald, M. & Rink, L. Zinc supplementation induces CD4+CD25+Foxp3+antigen-specific regulatory T cells and suppresses IFN-γ production by upregulation of Foxp3 and KLF-10 and downregulation of IRF-1. *Eur. J. Nutr.* **56**, 1859–1869 (2017).

108. Mousavi, S. M., Djafarian, K., Mojtahed, A., Varkaneh, H. K. & Shab-Bidar, S. The effect of zinc supplementation on plasma C-reactive protein concentrations: A systematic review and meta-analysis of randomized controlled trials. *Eur. J. Pharmacol.* **834**, 10–16 (2018).

109. Florea, D. *et al.* Changes in zinc status and zinc transporters expression in whole blood of patients with Systemic Inflammatory Response Syndrome (SIRS). *J. Trace Elem. Med. Biol.* **49**, 202–209 (2018).

110. Vatsalya, V. *et al.* Association of serum zinc with markers of liver injury in very heavy drinking alcohol-dependent patients. *J. Nutr. Biochem.* **59**, 49–55 (2018).

111. Tinkov, J. O. A., Skalny, A. & Suliburska, J. Zinc status is associated with inflammation , oxidative stress , lipid , and glucose metabolism. *J. Physiol. Sci.* **68**, 19–31 (2018).

112. Jarosz, M., Olbert, M., Wyszogrodzka, G., Młyniec, K. & Librowski, T. Antioxidant and anti-inflammatory effects of zinc. Zinc-dependent NF-κB signaling. *Inflammopharmacology* **25**, 11–24 (2017).

113. Maywald, M., Wessels, I. & Rink, L. Zinc signals and immunity. *Int. J. Mol. Sci.* **18**, (2017).

114. Bonaventura, P., Benedetti, G., Albarede, F. & Miossec, P. Zinc and its role in immunity and inflammation. *Autoimmun Rev* **14**, 277–285 (2015).

115. Prasad, A. S. Effects of zinc deficiency on Th1 and Th2 cytokine shifts. *J Infect Dis* **182 Suppl**, S62-8 (2000).

116. Dubben, S., Hönscheid, A., Winkler, K., Rink, L. & Haase, H. Cellular zinc homeostasis is a regulator in monocyte differentiation of HL-60 cells by 1α,25-dihydroxyvitamin D 3 . *J. Leukoc. Biol.* **87**, 833–844 (2010).

117. Sheikh, A. *et al.* Zinc Influences Innate Immune Responses in Children with Enterotoxigenic Escherichia coli-Induced Diarrhea. *J. Nutr.* **140**, 1049–1056 (2010).

118. Hasan, R., Rink, L. & Haase, H. Chelation of Free Zn2+ Impairs Chemotaxis, Phagocytosis, Oxidative Burst, Degranulation, and Cytokine Production by Neutrophil Granulocytes. *Biol. Trace Elem. Res.* **171**, 79–88 (2016).

119. Wirth, J. J., Fraker, P. J. & Kierszenbaum, F. Zinc requirement for macrophage function: effect of zinc deficiency on uptake and killing of a protozoan parasite. *Immunology* **68**, 114–9 (1989).

120. DeCoursey, T. E., Morgan, D. & Cherny, V. V. The voltage dependence of NADPH oxidase reveals why phagocytes need proton channels. *Nature* **422**, 531–534 (2003).

121. Chasapis, C. T., Spiliopoulou, C. A., Loutsidou, A. C. & Stefanidou, M. E. Zinc and human health: An update. *Arch. Toxicol.* **86**, 521–534 (2012).

122. Hasegawa, H., Suzuki, K., Suzuki, K., Nakaji, S. & Sugawara, K. Effects of zinc on the reactive oxygen species generating capacity of human neutrophils and on the serum opsonic activity in vitro. *Luminescence* **15**, 321–327 (2000).

123. Wu, A. *et al.* Salmonella utilizes zinc to subvert antimicrobial host defense of macrophages via modulation of NF-κB signaling. *Infect. Immun.* **85**, (2017).

124. Haase, H. *et al.* Zinc Signals Are Essential for Lipopolysaccharide-Induced Signal Transduction in Monocytes. *J. Immunol.* **181**, 6491–6502 (2008).

125. Thoen, R. U. *et al.* ZINC SUPPLEMENTATION REDUCES DIET-INDUCED OBESITY AND IMPROVES INSULIN SENSITIVITY IN RATS. *Appl. Physiol. Nutr. Metab.* apnm-2018-0519 (2018). doi:10.1139/apnm-2018-0519

126. García, O. P. *et al.* Zinc, iron and vitamins A, C and E are associated with obesity, inflammation, lipid profile and insulin resistance in Mexican school-aged children. *Nutrients* **5**, 5012–5030 (2013).

127. Troche, C., Beker Aydemir, T. & Cousins, R. J. Zinc transporter Slc39a14 regulates inflammatory signaling associated with hypertrophic adiposity. *Am. J. Physiol. - Endocrinol. Metab.* **310**, E258–E268 (2016).

128. Noh, H., Paik, H. Y., Kim, J. & Chung, J. The alteration of zinc transporter gene expression is associated with inflammatory markers in obese women. *Biol. Trace Elem. Res.* **158**, 1–8 (2014).

129. Foster, M. & Samman, S. Zinc and regulation of inflammatory cytokines: implications for cardiometabolic disease. *Nutrients* **4**, 676–694 (2012).

130. Lawson, R., Maret, W. & Hogstrand, C. Expression of the ZIP/SLC39A transporters in ß-cells: A systematic review and integration of multiple datasets. *BMC Genomics* **18**, 1–13 (2017).

131. Aydemir, T. B. *et al.* Aging amplifies multiple phenotypic defects in mice with zinc transporter Zip14 (Slc39a14) deletion. *Exp. Gerontol.* **85**, 88–94 (2016).

132. Wong, C. P., Magnusson, K. R. & Ho, E. Increased inflammatory response in aged mice is associated with age-related zinc deficiency and zinc transporter dysregulation. *J. Nutr. Biochem.* **24**, 353–359 (2013).

133. Liu, M. J. *et al.* ZIP8 Regulates Host Defense through Zinc-Mediated Inhibition of NF-κB. *Cell Rep.* **3**, 386–400 (2013).

134. Pereira, S. G. & Oakley, F. Nuclear factor-κB1: Regulation and function. *International Journal of Biochemistry and Cell Biology* **40**, 1425–1430 (2008).

135. Liuzzi, J. P. *et al.* Interleukin-6 regulates the zinc transporter Zip14 in liver and contributes to the hypozincemia of the acute-phase response. *Proc. Natl. Acad. Sci.* **102**, 6843–6848 (2005).

136. Lichten, L. A., Liuzzi, J. P. & Cousins, R. J. Interleukin-1 contributes via nitric oxide to the upregulation and functional activity of the zinc transporter Zip14 (Slc39a14) in murine hepatocytes. *AJP Gastrointest. Liver Physiol.* **296**, G860–G867 (2009).

137. Kim, M.-H., Aydemir, T. B., Kim, J. & Cousins, R. J. Hepatic ZIP14-mediated zinc transport is required for adaptation to endoplasmic reticulum stress. *Proc. Natl. Acad. Sci.* **114**, E5805–E5814 (2017).

138. Cousins, R. J. & Leinart, A. S. Tissue-specific regulation of zinc metabolism and metallothionein genes by interleukin 1. *FASEB J.* **2**, 2884–2890 (1988).

139. Mertens, K. *et al.* Low zinc and selenium concentrations in sepsis are associated with oxidative damage and inflammation. *Br. J. Anaesth.* **114**, 990–999 (2015).

140. Sobocinski, P. Z., Canterbury, W. J., Mapes, C. A. & Dinterman, R. E. Involvement of hepatic metallothioneins in hypozincemia associated with bacterial infection. *Am. J. Physiol. Metab.* **234**, E399 (1978).

141. Aktan, F. iNOS-mediated nitric oxide production and its regulation. *Life Sci.* **75**, 639–653 (2004).

142. Gálvez-Peralta, M., Wang, Z., Bao, S., Knoell, D. L. & Nebert, D. W. Tissue-specific induction of mouse ZIP8 and ZIP14 divalent cation/bicarbonate symporters by, and cytokine response to, inflammatory signals. *Int. J. Toxicol.* **33**, 246–258 (2014).

143. Beker Aydemir, T. *et al.* Zinc Transporter ZIP14 Functions in Hepatic Zinc, Iron and Glucose Homeostasis during the Innate Immune Response (Endotoxemia). *PLoS One* **7**, (2012).

144. Sayadi, A., Nguyen, A. T., Bard, F. A. & Bard-Chapeau, E. A. Zip14 expression induced by lipopolysaccharides in macrophages attenuates inflammatory response. *Inflamm. Res.* **62**, 133–143 (2013).

145. Larock, D. L., Chaudhary, A. & Miller, S. I. Salmonellae interactions with host processes. *Nat. Rev. Microbiol.* **13**, 191–205 (2015).

146. Knodler, L. A. *et al.* Cloning Vectors and Fluorescent Proteins Can Significantly Inhibit. *Society* **73**, 7027–7031 (2005).

147. Clark, L., Martinez-Argudo, I., Humphrey, T. J. & Jepson, M. A. GFP plasmid-induced defects in Salmonella invasion depend on plasmid architecture, not protein expression. *Microbiology* **155**, 461–467 (2009).

148. Kalderon, D., Roberts, B. L., Richardson, W. D. & Smith, A. E. A short amino acid sequence able to specify nuclear location. *Cell* **39**, 499–509 (1984).

149. Dang, C. V & Lee, W. M. Identification of the human c-myc protein nuclear translocation signal. *Mol. Cell. Biol.* **8**, 4048–4054 (2015).

150. Komar, A. A. & Hatzoglou, M. Cellular IRES-mediated translation: The war of ITAFs in pathophysiological states. *Cell Cycle* **10**, 229–240 (2011).

151. Kuhle, V., Abrahams, G. L. & Hensel, M. Intracellular Salmonella enterica Redirect Exocytic Transport Processes in a Salmonella Pathogenicity Island 2-Dependent Manner. *Traffic* **7**, 716–730 (2006).

152. Müller, P., Chikkaballi, D. & Hensel, M. Functional dissection of SseF, a membrane-integral effector protein of intracellular Salmonella enterica. *PLoS One* **7**, (2012).

153. Bernal-Bayard, J. & Ramos-Morales, F. Salmonella type III secretion effector SlrP is an E3 ubiquitin ligase for mammalian thioredoxin. *J. Biol. Chem.* **284**, 27587–27595 (2009).

154. Kuhle, V. & Hensel, M. SseF and SseG are translocated effectors of the type III secretion system of. *Cell. Microbiol.* **4**, 813–824 (2002).

155. Deiwick, J. *et al.* The translocated Salmonella effector proteins SseF and SseG interact and are required to establish an intracellular replication niche. *Infect. Immun.* **74**, 6965–6972 (2006).

156. Yu, X. J., Liu, M. & Holden, D. W. Salmonella effectors SseF and SseG interact with mammalian protein ACBD3 (GCP60) to anchor salmonella-containing vacuoles at the Golgi network. *MBio* **7**, 1–11 (2016).

157. Kuhle, V., Jäckel, D. & Hensel, M. Effector proteins encoded by Salmonella Pathogenicity Island 2 interfere with the microtubule cytoskeleton after translocation into host cells. *Traffic* **5**, 356–370 (2004).

158. Abrahams, G. L., Müller, P. & Hensel, M. Functional dissection of SseF, a type III effector protein involved in positioning the salmonella-containing vacuole. *Traffic* **7**, 950–965 (2006).

159. Krieger, V. *et al.* Reorganization of the Endosomal System in Salmonella-Infected Cells: The Ultrastructure of Salmonella-Induced Tubular Compartments. *PLoS Pathog.* **10**, (2014).

160. Hyun, S. I., Maruri-Avidal, L. & Moss, B. Topology of Endoplasmic Reticulum-Associated Cellular and Viral Proteins Determined with Split-GFP. *Traffic* **16**, 787–795 (2015).

161. Patel, J. C., Hueffer, K., Lam, T. T. & Galán, J. E. Diversification of a Salmonella Virulence Protein Function by Ubiquitin-Dependent Differential Localization. *Cell* **137**, 283–294 (2009).

162. Garai, P., Gnanadhas, D. P. & Chakravortty, D. Salmonella enterica serovars typhimurium and typhi as model organisms: Revealing paradigm of host-pathogen interactions. *Virulence* **3**, 377–388 (2012).

163. Chakravortty, D., Hansen-Wester, I. & Hensel, M. Salmonella Pathogenicity Island 2 Mediates Protection of Intracellular Salmonella from Reactive Nitrogen Intermediates . *J. Exp. Med.* **195**, 1155–1166 (2002).

164. Janssen, R., van der Straaten, T., van Diepen, A. & van Dissel, J. T. Responses to reactive oxygen intermediates and virulence of Salmonella typhimurium. *Microbes Infect.* **5**, 527–34 (2003).

165. Bruno, V. M. *et al.* Salmonella typhimurium type III secretion effectors stimulate innate immune responses in cultured epithelial cells. *PLoS Pathog.* **5**, (2009).

166. Zhang, S. *et al.* Transcriptional Response of Chicken Macrophages to Salmonella enterica Serovar Enteritidis Infection. in *Animal Genomics for Animal Health* 141–151 (KARGER, 2008). doi:10.1159/000317154

167. Wu, H., Jones, R. M. & Neish, A. S. The Salmonella effector AvrA mediates bacterial intracellular survival during infection in vivo. *Cell. Microbiol.* **14**, 28–39 (2012).

168. Knodler, L. A., Finlay, B. & Steele-Mortimer, O. The Salmonella effector protein SopB protects epithelial cells from apoptosis by sustained activation of Akt. *J. Biol. Chem.* **280**, 9058–9064 (2005).

169. Brennan, M. A. & Cookson, B. T. Salmonella induces macrophage death by caspase-1-dependent necrosis. *Mol. Microbiol.* **38**, 31–40 (2000).

170. Monack, D. M., Navarre, W. W. & Falkow, S. Salmonella-induced macrophage death: The role of caspase-1 in death and inflammation. *Microbes Infect.* **3**, 1201–1212 (2001).

171. McQuate, S. E. *et al.* Long-term live-cell imaging reveals new roles for Salmonella effector proteins SseG and SteA. *Cell. Microbiol.* **19**, (2017).

172. Keppler, A. *et al.* Labeling of fusion proteins of O6-alkylguanine-DNA alkyltransferase with small molecules in vivo and in vitro. *Methods* **32**, 437–444 (2004).

173. Bosch, P. J. *et al.* Evaluation of Fluorophores to Label SNAP-Tag Fused Proteins for Multicolor Single-Molecule Tracking Microscopy in Live Cells. *Biophys J* **107**, 803–814 (2014).

174. Liu, T. K. *et al.* A Rapid SNAP-Tag Fluorogenic Probe Based on an Environment-Sensitive Fluorophore for No-Wash Live Cell Imaging. *ACS Chem Biol* (2014). doi:10.1021/cb500502n

175. Heinis, C., Schmitt, S., Kindermann, M., Godin, G. & Johnsson, K. Evolving the substrate specificity of O6-alkylguanine-DNA alkyltransferase through loop insertion for applications in molecular imaging. *ACS Chem Biol* **1**, 575–584 (2006).

176. Geddes, K., Worley, M., Niemann, G. & Heffron, F. Identification of new secreted effectors in Salmonella enterica serovar Typhimurium. *Infect Immun* **73**, 6260–6271 (2005).

177. Chen, L. M., Briones, G., Donis, R. O. & Galan, J. E. Optimization of the delivery of heterologous proteins by the Salmonella enterica serovar Typhimurium type III secretion system for vaccine development. *Infect Immun* **74**, 5826–5833 (2006).

178. Mollwitz, B. *et al.* Directed evolution of the suicide protein O(6)-alkylguanine-DNA alkyltransferase for increased reactivity results in an alkylated protein with exceptional stability. *Biochemistry* **51**, 986–994 (2012).

179. Kufer, S. K. *et al.* Covalent immobilization of recombinant fusion proteins with hAGT for single molecule force spectroscopy. *Eur Biophys J* **35**, 72–78 (2005).

180. VanEngelenburg, S. B. & Palmer, A. E. Fluorescent biosensors of protein function. *Curr Opin Chem Biol* **12**, 60–65 (2008).

181. Plant, J. & Glynn, A. A. Natural resistance to Salmonella infection, delayed hypersensitivity and Ir genes in different strains of mice. *Nature* **248**, 345–347 (1974).

182. Guo, M. *et al.* High-resolution quantitative proteome analysis reveals substantial differences between phagosomes of RAW 264.7 and bone marrow derived macrophages. *Proteomics* (2014). doi:10.1002/pmic.201400431

183. Cuellar-Mata, P. *et al.* Nramp1 modifies the fusion of Salmonella typhimurium-containing vacuoles with cellular endomembranes in macrophages. *J. Biol. Chem.* **277**, 2258–2265 (2002).

184. Helaine, S. *et al.* Dynamics of intracellular bacterial replication at the single cell level. *Proc. Natl. Acad. Sci.* **107**, 3746–3751 (2010).

185. Andreu, N. *et al.* Primary macrophages and J774 cells respond differently to infection with Mycobacterium tuberculosis. *Sci. Rep.* **7**, 1–12 (2017).

186. Berghaus, L. J. *et al.* Innate immune responses of primary murine macrophage-lineage cells and RAW 264.7 cells to ligands of Toll-like receptors 2, 3, and 4. *Comp. Immunol. Microbiol. Infect. Dis.* **33**, 443–54 (2010).

187. Portnoy, D. A., Auerbuch, V. & Glomski, I. J. The cell biology of Listeria monocytogenes infection: The intersection of bacterial pathogenesis and cell-mediated immunity. *J. Cell Biol.* **158**, 409–414 (2002).

188. Lebreton, A., Stavru, F. & Cossart, P. Organelle targeting during bacterial infection: Insights from Listeria. *Trends Cell Biol.* **25**, 330–338 (2015).

189. Rolhion, N. & Cossart, P. How the study of Listeria monocytogenes has led to new concepts in biology. *Future Microbiol.* **12**, 621–638 (2017).

190. Cossart, P. & Lebreton, A. A trip in the 'new Microbiology' with the bacterial pathogen Listeria monocytogenes. *FEBS Lett.* **588**, 2437–2445 (2014).

191. Disson, O. & Lecuit, M. Invitro and invivo models to study human listeriosis: Mind the gap. *Microbes Infect.* **15**, 971–980 (2013).

192. D'Orazio, S. E. F. Animal models for oral transmission of Listeria monocytogenes. *Front. Cell. Infect. Microbiol.* **4**, 1–6 (2014).

193. Birmingham, C. L. *et al.* Listeriolysin O allows Listeria monocytogenes replication in macrophage vacuoles. *Nature* **451**, 350–354 (2008).

194. Helaine, S. & Holden, D. W. Heterogeneity of intracellular replication of bacterial pathogens. *Curr. Opin. Microbiol.* **16**, 184–191 (2013).

195. Balestrino, D. *et al.* Single-cell techniques using chromosomally tagged fluorescent bacteria to study Listeria monocytogenes infection processes. *Appl. Environ. Microbiol.* **76**, 3625–3636 (2010).

196. Engelbrecht, F. *et al.* A new PrfA-regulated gene of Listeria monocytogenes encoding at small, secreted protein which belongs to the family of internalins. *Mol. Microbiol.* **21**, 823–837 (1996).

197. de las Heras, A., Cain, R. J., Bielecka, M. K. & Vázquez-Boland, J. A. Regulation of Listeria virulence: PrfA master and commander. *Curr. Opin. Microbiol.* **14**, 118–127 (2011).

198. Rajabian, T. *et al.* The bacterial virulence factor InlC perturbs apical cell junctions and promotes cell-to-cell spread of Listeria. *Nat. Cell Biol.* **11**, 1212–1218 (2009).

199. Toledo-Arana, A. *et al.* The Listeria transcriptional landscape from saprophytism to virulence. *Nature* **459**, 950–956 (2009).

200. Gouin, E. *et al.* The Listeria monocytogenes InlC protein interferes with innate immune responses by targeting the I{kappa}B kinase subunit IKK{alpha}. *Proc. Natl. Acad. Sci. U. S. A.* **107**, 17333–8 (2010).

201. Polle, L., Rigano, L. A., Julian, R., Ireton, K. & Schubert, W. D. Structural details of human tuba recruitment by InlC of listeria monocytogenes elucidate bacterial cell-cell spreading. *Structure* **22**, 304–314 (2014).

202. Kühbacher, A., Gouin, E., Cossart, P. & Pizarro-Cerdá, J. Imaging InlC Secretion to Investigate Cellular Infection by the Bacterial Pathogen Listeria monocytogenes. *J. Vis. Exp.* 1–8 (2013). doi:10.3791/51043

203. Samba-Louaka, A. *et al.* Listeria monocytogenes Dampens the DNA Damage Response. *PLoS Pathog.* **10**, (2014).

204. Kühbacher, A. *et al.* Genome-Wide siRNA Screen Identifies Complementary Signaling Pathways Involved in Listeria Infection and Reveals Different Actin Nucleation Mechanisms during Listeria Cell Invasion and Actin Comet Tail Formation. *MBio* **6**, (2015).

205. Yang, F., Moss, L. G. & Phillips, G. N. The Molecular Structure of Green Fluorescent Protein The Molecular Structure of Green Fluorescent Protein. *Structure* **14**, 1–14 (2011).

206. Kamiyama, D. *et al.* Versatile protein tagging in cells with split fluorescent protein. *Nat. Commun.* **7**, 11046 (2016).

207. Moest, T. P. & Meresse, S. Salmonella T3SSs: successful mission of the secret(ion) agents. *Curr Opin Microbiol* **16**, 38–44 (2013).

208. Tsirigotaki, A., De Geyter, J., Šoštarić, N., Economou, A. & Karamanou, S. Protein export through the bacterial Sec pathway. *Nat. Rev. Microbiol.* **15**, 21–36 (2017).

209. Kunze, M. & Berger, J. The similarity between N-terminal targeting signals for protein import into different organelles and its evolutionary relevance. *Front. Physiol.* **6**, 1–27 (2015).

210. Baison-Olmo, F., Cardenal-Munoz, E. & Ramos-Morales, F. PipB2 is a substrate of the Salmonella pathogenicity island 1-encoded type III secretion system. *Biochem Biophys Res Commun* **423**, 240–246 (2012).

211. Specht, E. A., Braselmann, E. & Palmer, A. E. A Critical and Comparative Review of Fluorescent Tools for Live-Cell Imaging. *Annu. Rev. Physiol.* **79**, 93–117 (2016).

212. Stafford, S. L. *et al.* Metal ions in macrophage antimicrobial pathways: emerging roles for zinc and copper. *Biosci Rep* **33**, (2013).

213. Gaetke, L. M., McClain, C. J., Talwalkar, R. T. & Shedlofsky, S. I. Effects of endotoxin on zinc metabolism in human volunteers. *Am. J. Physiol. Metab.* **272**, E952–E956 (1997).

214. Leibbrandt, M. E. I. & Koropatnick, J. Activation of Human Monocytes with Lipopolysaccharide Induces Metallothionein Expression and Is Diminished by Zinc. *Toxicol. Appl. Pharmacol.* **124**, 72–81 (1994).

215. Subramanian Vignesh, K. *et al.* IL-4 Induces Metallothionein 3- and SLC30A4-Dependent Increase in Intracellular Zn2+that Promotes Pathogen Persistence in Macrophages. *Cell Rep.* **16**, 3232–3246 (2016).

216. Schroder, K. *et al.* Conservation and divergence in Toll-like receptor 4-regulated gene expression in primary human versus mouse macrophages. *Proc. Natl. Acad. Sci.* **109**, E944-53 (2012).

217. Ghasemi, A., Zahediasl, S., Hosseini-Esfahani, F. & Azizi, F. Reference Values for Serum Zinc Concentration and Prevalence of Zinc Deficiency in Adult Iranian Subjects. *Biol. Trace Elem. Res.* **149**, 307–314 (2012).

218. Hennigar, S. R., Lieberman, H. R., Fulgoni, V. L. & McClung, J. P. Serum zinc concentrations in the US population are related to sex, age, and time of blood draw but not dietary or supplemental zinc. *J. Nutr.* **148**, 1341–1351 (2018).

219. Huang, Z., Zhang, X. A., Bosch, M., Smith, S. J. & Lippard, S. J. Tris(2-pyridylmethyl)amine (TPA) as a membrane-permeable chelator for interception of biological mobile zinc. *Metallomics* **5**, 648–655 (2013).

220. Kiedrowski, L. Cytosolic zinc release and clearance in hippocampal neurons exposed to glutamate - the role of pH and sodium. *J. Neurochem.* **117**, 231–243 (2011).

221. Mato, S., Sánchez-Gḃmez, M. V., Bernal-Chico, A. & Matute, C. Cytosolic zinc accumulation contributes to excitotoxic oligodendroglial death. *Glia* **61**, 750–764 (2013).

222. Nicolson, T. J. *et al.* Insulin storage and glucose homeostasis in mice null for the granule zinc

transporter ZnT8 and studies of the type 2 diabetes-associated variants. *Diabetes* **58**, 2070–2083 (2009).

223. Qin, Y. *et al.* Direct comparison of a genetically encoded sensor and small molecule indicator: implications for quantification of cytosolic Zn(2+). *ACS Chem Biol* **8**, 2366–2371 (2013).

224. Hwang, J. J., Lee, S.-J., Kim, T.-Y., Cho, J.-H. & Koh, J.-Y. Zinc and 4-Hydroxy-2-Nonenal Mediate Lysosomal Membrane Permeabilization Induced by H2O2 in Cultured Hippocampal Neurons. *J. Neurosci.* **28**, 3114–3122 (2008).

225. Jeong, J. *et al.* Promotion of vesicular zinc efflux by ZIP13 and its implications for spondylocheiro dysplastic Ehlers-Danlos syndrome. *Proc Natl Acad Sci U S A* **109**, E3530-8 (2012).

226. Qian, J. & Noebels, J. L. Visualization of transmitter release with zinc fluorescence detection at the mouse hippocampal mossy fibre synapse. *J. Physiol.* **566**, 747–758 (2005).

227. Carter, K. P., Young, A. M. & Palmer, A. E. Fluorescent sensors for measuring metal ions in living systems. *Chem Rev* **114**, 4564–4601 (2014).

228. Park, J. G., Qin, Y., Galati, D. F. & Palmer, A. E. New Sensors for Quantitative Measurement of Mitochondrial Zn 2+. *ACS Chem. Biol.* **7**, 1636–1640 (2012).

229. Maret, W. Cellular Zinc and Redox States Converge in the Metallothionein/Thionein Pair. *J. Nutr.* **133**, 1460S-1462S (2003).

230. Helaine, S. *et al.* Internalization of Salmonella by Macrophages Induces Formation of Nonreplicating Persisters. *Science (80-.).* **343**, 204–208 (2014).

231. Saliba, A. E. *et al.* Single-cell RNA-seq ties macrophage polarization to growth rate of intracellular Salmonella. *Nat. Microbiol.* **2**, 1–8 (2016).

232. Pan, E. *et al.* Vesicular Zinc Promotes Presynaptic and Inhibits Postsynaptic Long-Term Potentiation of Mossy Fiber-CA3 Synapse. *Neuron* **71**, 1116–1126 (2011).

233. Rabouw, H. H. *et al.* Small molecule ISRIB suppresses the integrated stress response within a defined window of activation. *Proc. Natl. Acad. Sci.* **116**, 2097–2102 (2019).

234. Pavitt, G. D., Ramaiah, K. V. A., Kimball, S. R. & Hinnebusch, A. G. eIF2 independently binds two distinct eIF2b subcomplexes that catalyze and regulate guanine-nucleotide exchange. *Genes Dev.* **12**, 514–526 (1998).

235. Yang, W. & Hinnebusch, A. G. Identification of a regulatory subcomplex in the guanine nucleotide exchange factor eIF2B that mediates inhibition by phosphorylated eIF2. *Mol. Cell. Biol.* **16**, 6603–16 (1996).

236. Krishnamoorthy, T., Pavitt, G. D., Zhang, F., Dever, T. E. & Hinnebusch, A. G. Tight Binding of the Phosphorylated Subunit of Initiation Factor 2 (eIF2) to the Regulatory Subunits of Guanine Nucleotide Exchange Factor eIF2B Is Required for Inhibition of Translation Initiation. *Mol. Cell. Biol.* **21**, 5018–5030 (2002).

237. Jaishankar, P. *et al.* Pharmacological dimerization and activation of the exchange factor eIF2B antagonizes the integrated stress response. *Elife* **2**, 1–27 (2015).

238. Tsai, J. C. *et al.* Structure of the nucleotide exchange factor eIF2B reveals mechanism of memory-enhancing molecule. *Science (80-.).* **359**, eaaq0939 (2018).

239. Yoshida, H., Matsui, T., Yamamoto, A., Okada, T. & Mori, K. XBP1 mRNA Is Induced by ATF6 and Spliced by IRE1 in Response to ER Stress to Produce a Highly Active Transcription Factor. *Cell* **107**, 881–891 (2001).

240. Van Schadewijk, A., Van'T Wout, E. F. A., Stolk, J. & Hiemstra, P. S. A quantitative method for detection of spliced X-box binding protein-1 (XBP1) mRNA as a measure of endoplasmic reticulum (ER) stress. *Cell Stress Chaperones* **17**, 275–279 (2012).

241. Sidrauski, C. *et al.* Pharmacological brake-release of mRNA translation enhances cognitive memory. *Elife* **2013**, 1–22 (2013).

242. Liuzzi, J. P., Aydemir, F., Nam, H., Knutson, M. D. & Cousins, R. J. Zip14 (Slc39a14) mediates non-transferrin-bound iron uptake into cells. *Proc. Natl. Acad. Sci.* **103**, 13612–13617 (2006).

243. Datsenko, K. A. & Wanner, B. L. One-step inactivation of chromosomal genes in Escherichia coli K-12 using PCR products. *Proc Natl Acad Sci U S A* **97**, 6640–6645 (2000).

244. Glaser, P. *et al.* Comparative Genomics of Listeria Species. *Science* **294**, 849–853 (2001).

245. Van Engelenburg, S. B. & Palmer, A. E. Imaging type-III secretion reveals dynamics and spatial segregation of Salmonella effectors. *Nat. Methods* **7**, 325–30 (2010).

246. Feng, S. *et al.* Improved split fluorescent proteins for endogenous protein labeling. *Nat. Commun.* **8**, 370 (2017).

247. Nakamura, Y., Gojobori, T. & Ikemura, T. Codon usage tabulated from international DNA sequence databases: status for the year 2000. *Nucleic Acids Res.* **28**, 292 (2000).

248. Clarke IV, T. F. & Clark, P. L. Rare codons cluster. *PLoS One* **3**, (2008).

249. Silva-Herzog, E. & Detweiler, C. S. Salmonella enterica replication in hemophagocytic macrophages requires two type three secretion systems. *Infect Immun* **78**, 3369–3377 (2010).

250. Tanaka, A., To, J., O'Brien, B., Donnelly, S. & Lund, M. Selection of reliable reference genes for the normalisation of gene expression levels following time course LPS stimulation of murine bone marrow derived macrophages. *BMC Immunol.* **18**, 43 (2017).

251. Pfaffl, M. W. A new mathematical model for relative quantification in real-time RT-PCR. *Nucleic Acids Res.* **29**, 45e – 45 (2001).

Appendix A

Matlab Script for Segmentation and Tracking of Fluorescently Labeled Macrophage and Salmonella

A.1 Introduction

Provided here is the Matlab script that I used for image analysis of FRET sensor calibrations performed on BMDMs expressing the NES-ZapCV2 sensor. The forums on the Mathworks website were useful when troubleshooting or improving these scripts. Additionally, the Mathworks tutorial on Image Analysis is a great introduction to using MATLAB that is particularly focused on imaging data. I owe a big debt of thanks to Jian Wei Tay, Van Tra, Kyle Carter, and Joel Kralj and the Quantitative Optical Imaging Course for helping me make this script what it is.

A.2 Mac_track_FRET_analysis.m

This script will be functional if copied directly into MATLAB as long as the dependencies are present in the path folder. Dependencies can be obtained from the GitLab repository of Michael Minson located at https://biof-git.colorado.edu/mimi9073/Mac_tracking_zinc_analysis Please note that this script will work for FRET calibration experiments collected on a Nikon microscope with the file type '-.nd2' and experimental pauses for calibration events that correspond to the addition of the R_{min} buffer, Washout, and the addition of the R_{max} buffer. Additionally, this code handles multipoint image acquisition for better throughput per imaging dish. This script was generated in MATLAB version R2017b.

```
%% Mac_track_FRET_analysis
% Version 3, March 2019 by Mike Minson, Jian Tay
%
% Segmentation and Tracking pipeline for fluorescently labeled
% Macrophage and Salmonella
%
% Segments and tracks macrophage cells and salmonella, analyzes FRET
% calibration experiments giving important parameters such as Fractional
% saturation and zinc concentration. Outputs segmented cell track data with
% sensor paramters appended.
%
%% Dependencies:
% Can be obtained from the GitLab repository of Michael Minson at
% https://biof-git.colorado.edu/mimi9073/Mac_tracking_zinc_analysis
%
% 'Bioformats Image Toolbox (v1.0.4).mltbx'
% 'Cell tracking toolbox (Zinc Signalling)v1.1.6.mltbx'
% 'Cellular FRET Analysis v1.0.0.mltbx'
%
% 'correctLocalBackground.m', 'disptrack.m', 'dotplot.m', 'getfeatures.m',
% 'getPositionArea.m', 'isodd.m', 'makegif.m', 'outlineOverlay.m',
% 'outputdir.m', 'savefigs.m'
% 'plotSpread' toolbox from Mathworks
%% Specify paths for raw data and toolbox and specify background parameters
clear, clc, close all
% Specify the absolute path of your data directory
data_dir    =    uigetdir('/Users/mikeminson/Google    Drive/Palmer    Lab/Image
processing/',...
    'Select the directory for the Analysis');
addpath(genpath('/Users/mikeminson/Google    Drive/Palmer    Lab/GitLab'));    %
toolbox path
Analysis_dir = outputdir(data_dir); % Make output directory
addpath(Analysis_dir)

bgPrctile = 5; % define background pixel value percentile


m = 7; % define number of blocks to segment image for background subtraction
n = round(m);
if mod(n,2) == 0
    n = n+1;
end % checks if n is even else changes to odd
numBlocks = [n n];
clear vars m n

% Define channel indexes, these should be defined manually before analysis
FRET_channel = 0;
CFP_channel = 1;
%YFP_channel = 2;
MCH_channel = 2; %3;

%% Segmentation and tracking of cells acquired from .nd2 files

files = dir(fullfile(data_dir,'*.nd2')); %define .nd2 files in data_dir

for file = files(1:end)' %cycles through all files in data_dir
    r = bfGetReader(fullfile(data_dir, file.name));
```

```
    numSeries  =  r.getSeriesCount;  % Obtains series name for multipoint
acquisition
    OMEmeta = r.getMetadataStore();
    channelIn = r.getSizeC;

    for s = 1:numSeries
        try
            fprintf('Reading series #%d', s);
            r.setSeries(s-1);
            frames = r.getSizeT();
            for t = 0:frames-1
                % read images
                disp(t);

                iPlane = r.getIndex(0,CFP_channel,t)+1;
                CFP = bfGetPlane(r, iPlane);
                iPlane = r.getIndex(0,FRET_channel,t)+1;
                FRET = bfGetPlane(r, iPlane);
                iPlane = r.getIndex(0,MCH_channel,t)+1;
                MCH = bfGetPlane(r, iPlane);
                if exist('YFP_channel', 'var') == 1
                    iPlane = r.getIndex(0,YFP_channel,t)+1;
                    YFP =  bfGetPlane(r, iPlane);
                end

                timeSeries     =     double(OMEmeta.getPlaneDeltaT(s-1,iPlane-
1).value);
                % Subtract local background
                FRET_cor = correctLocalBackground(FRET,numBlocks,bgPrctile);
                CFP_cor = correctLocalBackground(CFP,numBlocks,bgPrctile);
                % Segment bacteria in red channel
                if exist('MCH_channel','var') == 1
                    MCH_cor = correctLocalBackground(MCH,numBlocks,bgPrctile);
                    bw = MCH_cor > 1300;
                    bw_mch = bwpropfilt2(bw, 'Area', [20, 500]);
                    %imshow(bw_mch)
                    %bw_mch = bwpropfilt2(bw, 'Circularity', [0.3 2]);
                end
                %ToDo: Validate upper limit for salmonella pixel area
                % Segment macs
                cell = imbinarize(FRET, 'adaptive', 'Sensitivity', 0.5,...
                    'ForegroundPolarity', 'bright');
                %imshow(FRET,[800 10000])
                cell0 = bwpropfilt2(cell, 'Area', [1000 20000]);
                cell1 = imfill(cell0, 'holes');
                bw_cell = imopen(cell1, strel('Disk', 15));
                bw2_cell = imerode(bw_cell, strel('Disk', 5));
                bw3_cell = imdilate(bw2_cell, strel('Disk', 2));

                % Calculate FRET ratio
                FRETratio = im2double(FRET_cor)./im2double(CFP_cor);
                FRETratio(isinf(FRETratio)) = 0;
                FRETratio(isnan(FRETratio)) = 0;
                %imshow(FRETratio, [1 9])

                % Get number of Salmonella inside each macs
                [maclabel,k] = bwlabel(bw3_cell);
                n = max(max(maclabel));
```

```
                detSalCount = [];
                detSalS = [];
                for i = 1:n
                    mac = maclabel == i;
                    mac_sal = logical(mac .* bw_mch);
                    [celllabel, L] = bwlabel(mac_sal);
                    Sals =  bwarea(mac_sal);
                    detSalS = [detSalS; Sals];
                    detSalCount = [detSalCount; L];
                end

                %Get the position and area of each of the labels
                [detAreas, detPos] = getPositionArea(maclabel);
                %Get features of each label
                detRatio2 = getfeatures(maclabel, FRETratio, 'PixelValues');
                detCFP = getfeatures(maclabel, CFP_cor, 'PixelValues');
                detFRET = getfeatures(maclabel, FRET_cor, 'PixelValues');

                if t == 0
                    %Initialize the cell tracker
                    cellTracker = tracker(t,'Series', ...
                        repmat(s, [size(detPos,1),1]), 'Times',...
                        repmat(timeSeries, [size(detPos,1),1]), 'Position',...
                        detPos, 'Area',detAreas, 'CFP', detCFP,...
                        'FRET', detFRET, 'Sal_count', detSalCount,...
                        'FRETratio', detRatio2, 'a', detSalS);
                    cellTracker.options = struct('MaxLinkDistance',150,...
                        'MaxTrackAge',2,'TrackMitosis',false,...
                        'MinAgeSinceMitosis',2,'MaxMitosisDistance',200,...
                        'MaxMitosisAreaChange',0.0,'LAPSolver','lapjv');

                else
                    %Track cells and store data parmeters in celltracker
                    cellTracker = cellTracker.assignToTrack(t,'Series', ...
                        repmat(s, [size(detPos,1),1]), 'Times',...
                        repmat(timeSeries, [size(detPos,1),1]), 'Position',...
                        detPos, 'Area',detAreas, 'CFP', detCFP,...
                        'FRET', detFRET, 'Sal_count', detSalCount,...
                        'FRETratio', detRatio2, 'a', detSalS);
                end
                % Create quality control movies and output to Gif
                cellPerim = imdilate(bwperim(maclabel > 0), strel('disk',1));
                imgOut = imoverlay(imadjust(FRET_cor,[0.3 0.7],[]),cellPerim);
                imgOut = disptrack(cellTracker, t, imgOut);
                makegif(imgOut,t+1,        Analysis_dir,        ['celltrack_',
file.name(1:end-4),...
                    '_',int2str(s)], 0.2);
                overlay2 = outlineOverlay(bw_mch,imadjust(MCH));
                overlay3 = imoverlay(overlay2, cellPerim);
                overlay4 = imoverlay(imgOut,bw_mch,'red');
                makegif(overlay3,t+1,    Analysis_dir,    ['Cell_Salmonella_',
file.name(1:end-4),...
                    '_',int2str(s)], 0.2);
                makegif(overlay4,t+1,     Analysis_dir,     ['Celltrack_Sal_',
file.name(1:end-4),...
                    '_',int2str(s)], 0.2);
            end
```

```
            save(fullfile(Analysis_dir,    ['cellTracker_',    file.name(1:end-
4),'_',...
                int2str(s), '.mat']), 'cellTracker', 'timeSeries');
        catch Error
            continue
        end
    end
end


%% FRET Analysis from celltracker data

% Read in cellTrackers from Analysis_dir
% Analysis can begin here if segmentation file 'Analysis_dir' exists
cellTracksFiles = dir(fullfile(Analysis_dir,'cellTracker_*_*.mat'));
cellTracks = [];
for indx = 1:numel(cellTracksFiles)
    cellTrackNames = cellTracksFiles(indx).name;
    load(cellTrackNames,'cellTracker');

    for iTrack = 1:numel(cellTracker.tracks.Data)

        if isempty(cellTracks)
            cellTracks = cellTracker.getTrack(iTrack);
            cellTracks.cellID = iTrack;

        else
            newIdx = numel(cellTracks) + 1;
            newCellTrack = cellTracker.getTrack(iTrack);
            newCellTrack.cellID = iTrack;

            cellTracks(newIdx) = newCellTrack;

        end
    end
end
for iTrack1 = 1:numel(cellTracks)
    cellTracks(iTrack1).Series = mean(cellTracks(iTrack1).Series,'omitnan');
end
% Trim data structure 'cellTracks' by deleting cells not present for the
% whole experiment. This affects cells innapropriately called in the
% segmentation algorithm
lastframe = [cellTracks.LastFrame];
startframe = [cellTracks.StartFrame];
logic1 = lastframe ~= max(lastframe);
logic2 = startframe ~= min(startframe);
cellTracks(logic1 | logic2) = [];

% Remove spurious FRET Ratio Values by replacing with NaN for cells that
% have a FRET ratio > 10
% for iFRET = 1:numel(cellTracks)
%     FRETRATIO = [cellTracks(iFRET).FRETratio];
%     logic3 = FRETRATIO >= 14;
%     cellTracks(iFRET).FRETratio(logic3) = mean(cellTracks(iFRET)....
%         FRETratio(logic3-1),cellTracks(iFRET).FRETratio(logic3+1));
% end
%
% Filter cells whos diff(FRETratio) > 2
```

```
% This removes the really noisy cell traces
% RATIOdiff calculates the difference in FRETratio from one frame to the next
% In the case of noise in the track logic4 thresholds the tracks to a
% specific limit
cellTracks2 = cellTracks;
% iDiff = [];
% for iDiff = 1:numel(cellTracks)
%     RATIOdiff = diff([cellTracks(iDiff).FRETratio]);
%     absRATIOdiff(iDiff) = max(abs(RATIOdiff));
% end

% logic4 = absRATIOdiff > 2.5;
% cellTracks2(logic4) = [];

% Plot FRET Ratio of Filtered cells
fig1 = figure;
for icell2 = 1:numel(cellTracks2)
    hold on
    plot(cellTracks2(icell2).Times,cellTracks2(icell2).FRETratio)
end
xlabel('Time (s)'), ylabel('FRET Ratio')
title('Raw FRET Ratio Cell Tracks');
hold off
print(fig1,[Analysis_dir,'/',file.name,'Raw FRET Ratio Cell Tracks','.tif'],'-
dtiff')
savefig(fig1,[Analysis_dir,'/',file.name,'Raw FRET Ratio Cell Tracks','.fig'])
% Find experiment events for calibrations
for itimes = 1:numel(cellTracks2)
    times(itimes) = any(isnan(cellTracks2(itimes).Times));
end
timeidx = find(times == 0);

event = find(diff(cellTracks2(timeidx(1)).Times)>63); % Finds time gaps greater
than 70 sec
resting_start = 1;
resting_end = event(1);
% Define the range of frames to calculate Rmin data.
min_start = event(1)+1;
min_end = event(2);
% Define the range of frames to calculate Rmax data.
max_start = event(2)+1;
max_end = frames;
% Event values depend on the shape of the 'event' variable and may change
% based on the length of pauses in a given experiment.
RatioFRET = [];
for iRatio = 1:numel(cellTracks2)
    RatioFRET(iRatio,:) = [cellTracks2(iRatio).FRETratio]';
end

Resting_mean = RatioFRET(:,resting_start:resting_end);
Resting_mean = movmean(Resting_mean',4,'omitnan');
Resting_mean_err = movstd(Resting_mean,4,'omitnan');

Ratio_min = RatioFRET(:,min_start:min_end);
Ratio_min = movmean(Ratio_min',4,'omitnan');
Ratio_min_err = movstd(Ratio_min,4,'omitnan');

Ratio_max = RatioFRET(:,max_start:max_end);
```

```
Ratio_max_mean = movmean(Ratio_max',4,'omitnan');
Ratio_max_mean_err = movstd(Ratio_max',4,'omitnan');

Ratio_mean = [Resting_mean',Ratio_min',Ratio_max_mean'];
Ratio_mean_err = [Resting_mean_err',Ratio_min_err',Ratio_max_mean_err'];

RMin = min(Ratio_min);
RMax = max(Ratio_max_mean);


%ToDo: Plot pixel intensity VS DR scatter plot look for trend and exclude
%cells based on overexpression of sensor

DR = RMax./RMin;
logic5 = DR > 2.3 | DR < 1.6;
AnalyzedTracks = cellTracks2;
AnalyzedTracks(logic5) = [];
Ratio_mean(logic5',:) = [];
Ratio_mean_err(logic5',:) = [];
Resting_mean(:,logic5) = [];
Resting_mean_err(:,logic5) = [];
RMin(logic5') = [];
RMax(logic5') = [];
DR(logic5) = [];

% Zinc sensor binding data as of 10 October 2016:
% ZapCY1: Kd=17 pM, hill=0.47
% ZapCY2: Kd=811 pM, hill=0.44
% ZapCV2: Kd=230 pM, hill=0.53
% ZapCV5: Kd=0.3 μM (300,000 pM), hill=0.553

Kd = 230;
hill = 0.53;
Resting_zn = [];
for izn = 1:numel(Ratio_mean(:,1))
    Resting_zn(:,izn) = Kd*((Resting_mean(:,izn) - RMin(izn))./...
        (RMax(izn) - Resting_mean(:,izn))).^(1/hill);
end

Frac_sat = [];
for izn1 = 1:numel(Ratio_mean(:,1))
    Frac_sat(:,izn1) = ((Ratio_mean(izn1,:) - RMin(izn1))./...
        (RMax(izn1) - RMin(izn1)));
end

Frac_sat_mean = mean(Frac_sat(resting_start:resting_end,:));

for idata = 1:numel(AnalyzedTracks)
    AnalyzedTracks(idata).Ratio_mean = Ratio_mean(idata,:);
    AnalyzedTracks(idata).Ratio_mean_err = Ratio_mean_err(idata,:);
    AnalyzedTracks(idata).DR = DR(idata);
    AnalyzedTracks(idata).Frac_sat = Frac_sat(:,idata);
    AnalyzedTracks(idata).Frac_sat_mean = Frac_sat_mean(idata);
    AnalyzedTracks(idata).Resting_zn = Resting_zn(:,idata);
end

save(fullfile(Analysis_dir,['Analyzed_tracks_',file.name(1:end-4),'.mat']),
'AnalyzedTracks')
```

```
fig2 = figure;
for icell3 = 1:numel(AnalyzedTracks)
    hold on
    plot(AnalyzedTracks(icell3).Times,AnalyzedTracks(icell3).Ratio_mean,...
        'LineWidth',2)
end
title('Smoothed FRET Ratio Cell Tracks','FontWeight','bold','FontSize',24)
xlabel('Time (s)','FontWeight','bold','FontSize',20)
ylabel('FRET Ratio','FontWeight','bold','FontSize',20)
ax = gca;
ax.LineWidth = 2;
ax.FontWeight = 'bold';
ax.FontSize = 16;
ax.XLim = [0 round(AnalyzedTracks(icell3).Times(end))];
hold off
print(fig2,[Analysis_dir,'/',file.name,'Smoothed FRET Ratio Cell
Tracks','.tif'],'-dtiff')
savefig(fig2,[Analysis_dir,'/',file.name,'Smoothed FRET Ratio Cell
Tracks','.fig'])

fig3 = figure;
hold on
subplot(2,1,1);
for icell3 = 1:numel(AnalyzedTracks)
     plot(AnalyzedTracks(icell3).Times(resting_start:resting_end),Resting_zn)
end
title('Resting [Zinc]')
xlabel('Time (s)','FontWeight','bold','FontSize',20)
ylabel('[Zn] (pM)','FontWeight','bold','FontSize',20)
xlim([0 AnalyzedTracks(icell3).Times(resting_end)])
subplot(2,1,2);
for icell3 = 1:numel(AnalyzedTracks)
    plot(AnalyzedTracks(icell3).Times(1:end),Frac_sat)
end
title('Fractional Saturation')
xlabel('Time (s)','FontWeight','bold','FontSize',20)
ylabel('Fractional Saturation','FontWeight','bold','FontSize',20)
xlim([0 AnalyzedTracks(icell3).Times(end)])
hold off
print(fig3,[Analysis_dir,'/',file.name,'Resting Zinc and Fractional Saturation
Cell Tracks','.tif'],'-dtiff')
savefig(fig3,[Analysis_dir,'/',file.name,'Resting Zinc and Fractional
Saturation Cell Tracks','.fig'])

fig4 = figure;
scatter(DR,Frac_sat_mean), title('Fractional Saturation VS Dynamic Range')
xlabel('Dynamic Range')
ylabel('Fractional Saturation')
print(fig4,[Analysis_dir,'/',file.name,'Fractional Saturation VS Dynamic
Range','.tif'],'-dtiff')
savefig(fig4,[Analysis_dir,'/',file.name,'Fractional Saturation VS Dynamic
Range','.fig'])

FRETmean = [];
FRETmin = [];
FRETmax = [];
for imean = 1:numel(AnalyzedTracks)
```

```
    FRETmean(imean)                                                    =
[mean(AnalyzedTracks(imean).FRET(resting_start:resting_end))];
    FRETmin(imean)                                                     =
[min(AnalyzedTracks(imean).FRET(resting_start:resting_end))];
    FRETmax(imean)                                                     =
[max(AnalyzedTracks(imean).FRET(resting_start:resting_end))];
end

fig5 = figure;
scatter3(DR,Frac_sat_mean,FRETmean), title('FracSat VS DR VS FRETmean')
xlabel('Dynamic Range')
ylabel('Fractional Saturation')
zlabel('FRET Intensity')
print(fig4,[Analysis_dir,'/',file.name,'FracSat VS DR VS FRETmean','.tif'],'-
dtiff')
savefig(fig4,[Analysis_dir,'/',file.name,'FracSat VS DR VS FRETmean','.fig'])

fig6 = figure;
scatter3(DR,Frac_sat_mean,FRETmin), title('FracSat VS DR VS FRETmin')
xlabel('Dynamic Range')
ylabel('Fractional Saturation')
zlabel('FRET Intensity')
print(fig4,[Analysis_dir,'/',file.name,'FracSat VS DR VS FRETmin','.tif'],'-
dtiff')
savefig(fig4,[Analysis_dir,'/',file.name,'FracSat VS DR VS FRETmin','.fig'])

fig7 = figure;
scatter3(DR,Frac_sat_mean,FRETmax), title('FracSat VS DR VS FRETmax')
xlabel('Dynamic Range')
ylabel('Fractional Saturation')
zlabel('FRET Intensity')
print(fig4,[Analysis_dir,'/',file.name,'FracSat VS DR VS FRETmax','.tif'],'-
dtiff')
savefig(fig4,[Analysis_dir,'/',file.name,'FracSat VS DR VS FRETmax','.fig'])
```